CHALMERS

Characterisation of the self-arrangement of gold nanoparticles on surfaces based on simulations and model experiments.

A thesis for the degree Master of Science

Joakim Brorsson

Supervisor: Anders Lundgren
Examiner: Krister Holmberg
The Department of Cell and Molecular Biology, Interface Biophysics
Göteborg University
Göteborg, Sweden 2012

Characterisation of the self-arrangement of gold nanoparticles on surfaces based on simulations and model experiments
Joakim Brorsson

Supervisor: Anders Lundgren
Examiner: Krister Holmberg
The Department of Cell and Molecular Biology, Interface Biophysics
Göteborg University

Cover:
This image is a combination of a, partially transparent, plot of a radially symmetric coverage gradient, calculated with help of the COMSOL Multiphysics® software, and an SEM image of a cysteamine functionalised gold surface, which has been covered by charge stabilised 10 nm gold nanoparticles.

Characterisation of the self-arrangement of gold nanoparticles on surfaces based on simulations and model experiments

Joakim Brorsson

November 8, 2012

Supervisor: Anders Lundgren
Examiner: Krister Holmberg

KBTX05 - Master thesis at Chemical and Biological Engineering
The Department of Cell and Molecular Biology, Interface Biophysics
Göteborg University
Göteborg, Sweden 2012

Characterisation of the self-arrangement of gold nanoparticles on surfaces based on simulations and model experiments.

Joakim Brorsson
Supervisor: Anders Lundgren
Examiner: Krister Holmberg
The Department of Cell and Molecular Biology, Interface Biophysics
Göteborg University

Abstract: Gold nanoparticles possess many unique properties and can, for example, form strong covalent bonds with certain chemical functionalities, in particular thiol and amino groups. This mechanism is, in particular, exploited in the concept for the self-organisation of Au NPs on gold covered silicon substrates, coated with either dithiol or cysteamine SAMs, which is the principle subject of this thesis. Specifically, the project, described in this report, focused on a method for controlling the interparticle repulsion, and thus the separation between the adsorbed particles, by tuning the ionic strength. Following functionalisation, the patterned surfaces thus obtained can, among other things, be used to study the cellular adhesion or, more generally, the response of cells presented to such nanostructures.

The study began with development of a mathematical model for the method of depositing one-dimensional gradients of 10 nm gold nanoparticles on planar surfaces, originally proposed by A. Lundgren [1]. It was, in particular, shown that this physical situation could be, relatively, accurately described as an, analytically solvable, diffusion problem combined with a deposition process, which can be represented with help of the theory of random sequential adsorption. The same physical model was later implemented in order to develop experimental setups, with which radially symmetric Au NP gradients can be achieved. Specifically, the molecular diffusion process inside geometries representing the suggested designs were simulated using the COMSOL Multiphysics® software, to determine suitable values on the design parameters. From the surface electron microscope, SEM, analysis of the patterned surfaces, obtained with the final product of this development process, it was concluded that should be possible to achieve radially symmetric coverage profiles with experimental setups based on the proposed concept.

Sammanfattning: Guld nanopartiklar äger en kombination av unika egenskaper och kan, exempelvis, ingå i starka kovalenta bindingar med vissa typer av molekyler, i synnerhet sådana som innehåller thiol- eller aminogrupper. Det är denna interaktionsmekanism som utgör grunden för den metod för att få guld nanopartiklar att spontant arrangera sig i bestämda mönster på guldbeklädda kiselsubstrat, vilka täcks av enskilda lager av antingen dithioleller cysteaminmolekyler. Det projekt som beskrivs häri, har, i synnerhet, fokuserat på ett koncept för att kontrollera repulsionen, och därmed även, avståndet mellan de ytadsorberade partiklarna genom att ändra jonstyrkan. Efter att ha funktionaliserats, kan sådana ytor användas för att studera, blandat annat, inbindning av celler eller, mer generellt, hur celler reagerar på förekomsten av sådana nanostrukturerer.

Studien ifråga inleddes med utvecklandet av en matematisk modell för den teknik som tidigare använts, av A. Lundgren, för att adsorbera endimensionella gradienter av guld nanopartiklar på släta ytor [1]. Det kunde, i synnerhet, påvisas att detta skeende kan representeras som ett, analytiskt lösbart, diffusions problem följd av en deponering process, vilken i sin tur kan beskrivas inom ramen för den så kallade RSA, "Random Sequential Adsorption", modellen. Samma metodik användes senare för att ta fram en experimentel uppställning, ämnad för att deponera en gradient av nanopartiklar, med radiell symmetri, på ett plant substrat. Mer specifikt utnyttjades COMSOL Multiphysics® programvara för att bestämma hur värdena på diverse nyckelparametrar lämpligen skulle väljas. De mönstrade ytor, som skapats med hjälp av den design som utgjorde slutprodukten från denna desginprocess, analyserades sedan med ett svepelektronmikroskop. Med utgångspunkt från detta resultat drogs slutsatsen att det, mycket riktigt, är möjlig att åstadkomma radiellt symmetriska täckningsprofiler genom att tillämpa uppställningar konstruerade i enlighet med det föreslagna konceptet.

Keywords: Gold nanoparticles; Nanoparticle adsorption; Coverage gradients; Patterned surfaces; Self-organisation; self-assembled monolayer; Concentration gradients; Molecular diffusion; Fick's laws; DLVO theory; random sequential adsorption; Numerical simulations; Scanning electron microscope.

Acknowledgements First and foremost, I wish to thank my supervisor Dr Anders Lundgren, who, in spite of his busy schedule, took the time to guide me through my diploma work. His advise and support has been much appreciated. Moreover, I would like to extend my gratitude to Anders supervisor, Dr Mattias Berglin, whose constant support and willingness to share his knowledge and expertise has benefited me greatly. I am, also, very grateful for the practical aid provided by Dr Jenny Lindström. Without her help and guidance it would have been impossible to perform the experiments, which were central to this study. In this context, I can not forget to mention my appreciation of the encouraging words offered by Professor Hans Elwing, who has, additionally, been the source of many interesting discussions. Furthermore, I send a special word of thanks to COMSOL AB, specifically for helping me to resolve the issues I encountered when implementing the COMSOL Multiphysics® software. Lastly, I very much appreciate that Professor Krister Holmberg agreed to be the examiner for this diploma work.

On a final note, I would like to thank my family for their unconditional love, patience and support.

Contents

List of Figures

List of Tables

Chapter 1

Introduction

The aim of this introductory chapter is to provide a context for the project. Specifically, both the background as well as formulations of specific goals and limitations will be presented, in that order.

Due to the similarity in size between on one hand nanomaterials, such as nanoparticles, or NPs, and on the other biological molecules, such as proteins and DNA, it is possible to create hybrid systems with unique and novel features as is detailed in a recent review by Willner and Willner [2]. A key functionality of many such systems is the ability to self-assemble into different types of ordered structures. For example, Lundgren, Björefors, Olofsson and Elwing have presented a method for obtaining uniform distributions of charged-stabilized gold nanoparticle on octanedithol monolayers using a procedure based on self-assembly [1]. In particular, this technique is referred to as the Nano Particle Binary Chemistry, NPBC, method. Utilizing such a procedure another research group, Lundgren et al, created arrays of similar macromolecule and nanoparticle hybrids on a PEG background [3]. Here, the aim was to use the obtained architectures to study the interaction between the macromolecules and a cell surface and how this binding is affected by, for instance, the molecular spacing.

Studies, such as those described above, are made possible by the fact that the previously mentioned assembly method allows the interparticle distance to be controlled. As a result of continuing research, this technique has been further refined by Lundgren and his colleges [4]. Specifically, these researchers have reported that they have been able to create gradients of nanoparticles on suitable substrates. The surfaces thus obtained have, furthermore, supposedly been successfully used to study cell adhesion [5]. According to Lundgren,

such nonuniform nanopatterned surfaces are very attractive for exploring the cellular response to different types of nanoscopic systems [5].

It is important to note that the average distance between the Au NPs is controlled by Debye-screening and hence by, among others, the concentration of electrolyte [1]. It is thus possible to make the nanoparticles self-assemble into a particular pattern, for example a one-dimensional gradient, by setting up a salt gradient in a uniform nanoparticle suspension. This should lead to the formation of a NP mono layer on the substrate, with the highest coverage being achieved on the areas of the surface that are in contact with the regions of the solution containing the greatest number of ions. Still, the fact that this ionic gradient must evolve in time, and eventually disappear, makes studying the underlying diffusion process, for different geometrical setups, a highly relevant issue for continuing research.

One possible route to obtain data pertaining to the time evolution of chemical gradients is the implementation of numerical calculations. In particular, quantitatively important results could be ascertained by creating suitable models of physical systems of interest and then simulating the diffusion of ions. For this research to be relevant, the model systems that are initially considered should be simple enough that accurate experimental data is available. Specifically, this should allow the numerical method, or methods, used to be tested before moving on to more complex geometries. This work could potentially result in refined estimates of key parameters that are related not only the computations but also the experimental procedure. The simulations should, more precisely, make it possible to quantify the time and salt content needed to achieve a certain gradient of nanoparticles in a particular geometry. It will perhaps even be possible to find an optimum with regards to the choice of the two former variables.

Once a sufficiently accurate methodology has been developed the next step would be to consider more complex systems, which could possibly be regarded as more practically important. With help of the same type of methods as before, simulations can be performed for a variety of geometries with different dimensionalities to yield predictions how the NP patterns evolve with time. Again, it might even be possible to find the amount and mode by which the salt should be added and how long time these ions should be allowed to diffuse to achieve a particular gradient.

1.1 Task

This diploma work will, to a large extent, involve using the computer software COMSOL Multiphyisics® to simulate the diffusion of counterions, in this case citrate, in various geometries. Initially, the aim will be to consider one-dimensional problems for which comparable experimental results are already available. It should hence be possible to directly compare the calculations with reference data, and thus optimize the models used in the simulations. Another goal with this part of the project will be to try and determine the time and salt content required for a certain concentration profile and thus a particular nanoparticle gradient to develop, since such data is not available at the present. Thereafter, the work ought to primarily involve extending the computer simulations to more complex systems with higher dimensionalities. Concomitantly, efforts will be made to obtain measurements that are comparable to the computed data. This should, more precisely, be achieved by using experimental setups that mirror the model systems.

Though this project will primarily be theoretical in nature, and mainly be focused on the earlier mentioned computer simulations, some experiments are also meant be performed. This part of the work should , for instance, involve using different analytical tools, such as SEM, in order to extract relevant data from empirical studies. To put these results into context, efforts will also be made to gather information about the underlying physical mechanism as well as possible applications for this self-assembly process. The former type of knowledge should, in particular, be important in order to be able to understand the limitations of the method and thus the types of structures that provide suitable model systems.

Though the exact nature of the model systems that are to be analysed, as part of this project, has not yet been established, the aim is to consider at least two three-dimensional systems. One geometry of interest is an experimental setup with which it is possible to create nanoparticle gradients, on a substrate surface, that are radially symmetric. Specifically, one part of the project will involve designing, constructing, testing and simulating a system that is suitable for this purpose. An additional goal is to examine some type of gel system, made up by fibres onto which gold nanoparticles can be deposited. Though the ultimate goal would be to consider a geometry in which it is possible to obtain truly three-dimensional gradients of NPs experimentally, the inherent complexity of gel systems makes this a daunting prospect.

In order to deduce what is required of the gel in order for the deposition to proceed as expected, the process by which nanoparticles diffuses through such

systems must first be researched. This should provide enough background information to allow simulations to be performed. Moreover, it should at least be possible to obtain comparable experimental data by studying the transport of ions through a suitable setup, even if the attempts at patterning the structure with nanoparticles should fail. Specifically, it ought to be noted that the development of models that describe the diffusion of nanoparticles through gel-like structures is the subject of current research, as is concluded by both Cu and Saltzman as well as Cai, Panyukov and Rubinstein [6, 7]. Therefore, it is by no means certain that a suitable system can be found within the time frame for this project.

1.2 Boundaries and Limitations

Though mechanism governing the diffusion of the nanoparticles and the ions are in principle the same, no efforts will be made to simulate the transport of the NPs, the absorption of such particles on surfaces nor the coupling between these processes. All these subjects will be thoroughly discussed in the report, however. With regards to the model systems used for the experimental part of the project, these are only supposed to be used to obtain measurements comparable to the computed data. Even if potential applications might be mentioned in the final report, these systems, or modified versions of them, will not be further studied. In particular, no efforts will be made to use these setups for biological research, which is otherwise one of the fields of science where surfaces modified with nanoparticles have many important uses, as is discussed by Lundgren et al [1].

Chapter 2

Mathematical Modelling.

This chapters details three specific aspects of the development of the different mathematical models that were used as part of this project. In the first sections, some of the general types of transport phenomena that are applicable for the systems of interest will be discussed. This will be followed by presentation of two distinctive formulations of the 1D diffusion problem, which represents the physical situation described in section 3.1.1, to which analytical solutions can be found. In the final part of this chapter, meanwhile, a pair of key concepts, in the form of the DLVO theory and the RSA model, will be presented. As is further explained in section 3.2.2, these are, specifically, used to relate the calculated citrate concentration with a certain particle coverage.

2.1 Molecular Transport Phenomena

For a given electrolyte solution there will exist a certain number of forces, which completely govern the transport within the system. Since the origin of the underlying mechanisms can differ greatly, this also holds true for the mathematical expressions that are used to describe them. In some cases there even exists several competing models, which may be based on contrasting approximations or even completely different theories.

For ions that are dissolved in an aqueous medium, the primary forces of interest can be separated into two types. Firstly, there may exist one or more forces originating from outside the system. Common examples include gravitational and electromagnetic fields as well as pressure gradients. While

the presence of an external electrical potential should only affect the motion of the ions, a non-uniform density distribution should result in convective currents within the entire fluid medium. Since the system considered in this work were assumed not to be affected by external forces, these will not be further discussed, however. Many different types of intrinsic interactions will, additionally, exist between the individual molecules and particles that make up the system. Due to the microscopic origin of these internal forces, these are not explicitly included in the statements of the, macroscopic, transport equations, provided in section 2.1.1. Even so, this type phenomena will contribute to the motion of both the solvent and solute molecule as well as any particles suspended in the liquid. As will be explained in section 2.1.2, however, the concept of Brownian motion can be regarded as an indirect result of these interactions. In the remainder of this section, only the key formulas, for describing the transport of molecules and particles in liquid media, will be presented. Readers that are more keenly interested in the underlying theories ar therefore highly recommended to seek out the excellent literary sources that are referenced in the text.

2.1.1 Fick's Laws of Diffusion

In a dilute solution of inert and uncharged colloids the only forces of interest will, given that there are no external force fields present, originate from collisions with the solvent molecules [8]. Under such conditions the particle transport can be adequately described by the Fickian diffusion equations [9]. Specifically, Fick's first law can be derived within the framework of the random walk model, which is described in section 2.1.2. According to this formula, the flux $\boldsymbol{J}_i$, of a species i, is directly proportional to the concentration gradient, $\boldsymbol{\nabla} c_i$, so that

$$\boldsymbol{J}_i = -D_i \boldsymbol{\nabla} c_i, \tag{2.1.1.1}$$

where D_i is the diffusion constant [6, 8]. If this relation is combined with the statement of mass conservation

$$\frac{\partial c_i}{\partial t} = -\boldsymbol{\nabla} \cdot \boldsymbol{J}_i, \tag{2.1.1.2}$$

Fick's second law,

$$\frac{\partial c_i}{\partial t} = \boldsymbol{\nabla} \cdot (D_i \boldsymbol{\nabla} c_i), \tag{2.1.1.3}$$

is obtained. Given proper statements of the boundary and initial conditions, this differential equation can be solved in order to determine the concentration at every point in space $\boldsymbol{r}$ and time t, $c_i(\boldsymbol{r},t)$, for each species i.

Generally, it is necessary to consider both convection, diffusion as well as migration effects when formulating the equations, which describe the macroscopic motion of charged particles, or molecules, in a fluid medium [10, 9, 11]. As was explained earlier, these three transport mechanism result from gradients in either the pressure or the density, the concentration and the electrical potential respectively. In this work, however, only the diffusive motion will be taken into account. Even so, the COMSOL Multiphysics® interface "Transport of Diluted Species", which has been developed for solving physical problems of this type, allows all three phenomena to be simulated. As was mentioned in section 3.2.3, this is achieved by providing the program with explicit expressions for any velocity and electric fields that might be present as well as the rate laws for all chemical reactions, involving the molecules of interest [10]. Accordingly, the mass balance equation, for each species i, takes on the form

$$\frac{\mathrm{d}c_i}{\mathrm{d}t} = \boldsymbol{\nabla}\left(-D_i\boldsymbol{\nabla}c_i - Z_i\mu_i F_0 c_i \boldsymbol{\nabla}V + c_i\boldsymbol{v}\right) = R_i \qquad (2.1.1.4)$$

where D_i, c_i, Z_i and μ_i are the diffusion coefficient, concentration, valency and electronic mobility, respectively. While the third term, on the left hand side, represents the convection, due to the velocity field $\boldsymbol{v}$, the fourth corresponds to the migration, which is driven by the electrical potential V. The Faraday constant F_0, meanwhile, is defined as $F_0 \equiv eN_A$, where e is the elementary charge and N_A is the Avogadro constant. Even though physical situations considered in this project are influenced by the effects of both convection, migration and chemical reactions as well as diffusion, the chosen model only takes the latter of these mechanisms into account. This is equivalent to setting $V = 0$, $v = 0$ and $R_i = 0$, $\forall i$, in the continuity equation, (2.1.1.4), which returns Fick's second law, (2.1.1.3).

2.1.2 Brownian Motion

The random movements of particles suspended in a liquid, which is due to the statistical nature of the interactions with the solvent molecule, is if often referred to as Brownian motion [8]. Though first discovered by sir Robert Brown, in the 1820s, it was Einstein who developed the mathematical formalism required for describing this process mathematically [8]. In particular,

he introduced the so called "random walk" concept, in the beginning of the 20^{th} century. This model describes the motion of a diffusing particle as a series of equally long, yet uncorrelated, steps, which directions are randomly chosen [8, 6].

By modelling the diffusion process as a random walk, Einstein managed to deduce the following formula for the diffusion coefficient,

$$D_{c\to 0} = \frac{\langle x^2 \rangle}{2t}, \tag{2.1.2.1}$$

which appears in Fick's first and second laws, as the equations (2.1.1.1) and (2.1.1.3) respectively show [8, 6]. Here, the nominator represents the average of the squared distance that the particles move during a certain time t [8, 6]. In accordance with the notation adopted by Cu, the subscript $c \to 0$ indicates that this relation, strictly, only holds in the limit of infinite dilution [8, 6]. Although the movements of the individual particles have no preferred direction, there will, in the presence of concentration gradients, be a net motion towards the more dilute regions [6]. Given that the colloids are not subjected to any external forces, these will, thus, gradually spread out until, $t = \infty$, at which time the distribution is entirely uniform [6].

Einstein is also derived an alternative expression for D, based on the assumption that the diffusion process is exclusively determined by the hydrodynamic drag force [6]. As a result of these efforts, he arrived at the equation

$$D_{c\to 0} = \frac{k_B T}{C_f}. \tag{2.1.2.2}$$

This expression is often referred to as the Einstein relation, where k_B is the Boltzmann constant, T the absolute temperature, measured in Kelvin, and C_f is the frictional drag coefficient [6]. As was discovered by Stokes, the latter parameter is, in the case of spherical particles moving through a continuous liquid, a function of the hydrodynamic radius of the particle, a_{hyd}, as well as the viscosity of the surrounding medium, μ,

$$C_f = 6\pi\mu a_{\text{hyd}}. \tag{2.1.2.3}$$

If this formula is substituted into (2.1.2.2), the familiar Stokes-Einstein equation,

$$D_{c\to 0} = \frac{k_B T}{6\pi\mu a_{\text{hyd}}}, \tag{2.1.2.4}$$

is obtained.

2.2 Analytically Solvable 1D Models.

In this section the one-dimensional model of the experimental setup, described in section 3.1.1, will be introduced. Specifically, two different mathematical formulations of this molecular transport problem, which can be solved analytically, will be presented in the first two subsections. Note that all the numerical results, that can be obtained by introducing the proper parameter values into these models, can be found in section 4.1.

In short, the task at hand involves modelling the diffusion of a single species, with a certain concentration $c(x,t)$, in one dimension. As was discussed in section 2.1, the governing equation for this process is Fick's second law,

$$\frac{\partial c}{\partial t} = D\frac{\partial^2 c}{\partial x^2}, \tag{2.2.0.5}$$

that is obtained by combining Fick's first law

$$J = -D\frac{\partial c}{\partial x}, \tag{2.2.0.6}$$

with the continuity equation

$$\frac{\partial c}{\partial t} = -\frac{\partial J}{\partial x}, \tag{2.2.0.7}$$

which have all been stated under the assumption that the diffusion coefficient has no spatial dependence. Though the same equation, (2.2.0.5), is solved in each of the cases presented below, the applied initial and boundary conditions differ.

2.2.1 Infinite domain.

In the simplest model considered, the domain is assumed to have an infinite extension with the interface between the two liquid phases positioned at $x = 0$. It is also assumed that the concentration profile initially takes the form of a step function with $c(x,0) = c_0$ for $x \leq 0$ and $c(x,0) = 0$ for $x > 0$. The most appropriate boundary conditions for this geometry, defined by the interval $x \in]-\infty,\infty[$, are to let $c(x,t) \to c_0$ and $c(x,t) \to 0$ when $x \to -\infty$ and $x \to \infty$ respectively. Mathematically, the task is thus to find a solution

to the problem

$$\begin{cases} \frac{\partial}{\partial t}c(x,t) = D\frac{\partial^2}{\partial x^2}c(x,t) \\ c(x,0) = \begin{cases} c_0, & x \leq 0 \\ 0, & x > 0 \end{cases} \\ c(x,t) \xrightarrow[x\to-\infty]{} c_0 \\ c(x,t) \xrightarrow[x\to+\infty]{} 0 \end{cases}, \tag{2.2.1.1}$$

which represents the system that is schematically depicted in figure 2.1. Note that this is the same problem that is consider by Lundgren [5].

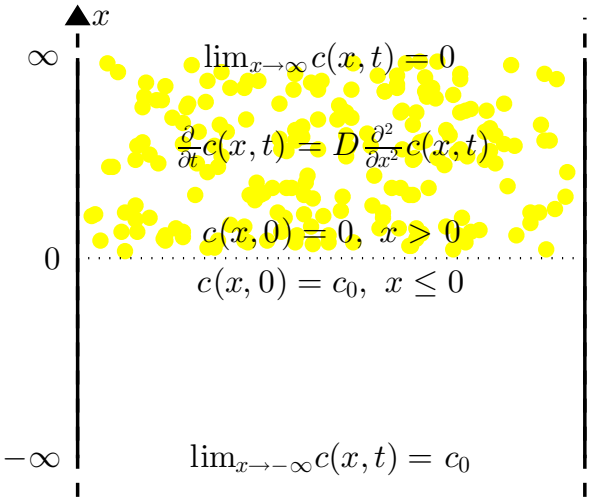

Figure 2.1: Illustration of the system represented by the initial and boundary value problem inequation (2.2.1.1), which describes the diffusion of a single species in one-dimensional domain that extends from $-\infty$ to $+\infty$.

A convenient method for handling the above partial differential equation, PDE, is to first apply a suitable transform to reduce it to an ordinary differential equation, ODE. In this case there are two possibilities. One conceivable method is to apply a Fourier transform with respect to the spatial coordinate x and use the boundary conditions to get rid of the second derivative, $\partial^2/\partial x^2$. Alternatively, the equation can be Laplace transformed in order to remove the explicit time dependence, specifically the derivative $\partial/\partial t$, which

is achieved with help of the the initial condition. Before proceeding with the latter approach it is convenient to first give a short summery of the characteristic features of this specific transform.

According to Folland, the Laplace transform is a special case of the Fourier transform which is applicable for functions $f(t)$ that are piecewise continuous on the half-line, $t \in [0,\infty[$ and satisfy the inequality

$$\|f(t)\| \leq C\mathrm{e}^{\upsilon t}, \tag{2.2.1.2}$$

where $C \geq 0$ and $\upsilon \in]-\infty,\infty[$ are some constants [12]. The same mathematical formalism is also applicable for cases where $f(t)$ is defined on $t \in]-\infty,\infty[$ provided that $f(t) = 0$ for $t < 0$. Specifically, the Laplace transform of the $f(t)$ is defined as the function

$$\tilde{f}(\omega) = \mathscr{L}\left\{f(t)\right\}(\omega) = \int_0^\infty f(t)\mathrm{e}^{-\omega t}\mathrm{d}t, \tag{2.2.1.3}$$

where ω is a complex variable such that $\tilde{f}(\omega)$ is analytical, that is differentiable, in the domain $\mathrm{Re}(\omega) > \upsilon$. Equally, $f(t)$ can be obtained from $\tilde{f}(\omega)$ using the inversion formula

$$f(t) = \mathscr{L}^{-1}\left\{\tilde{f}(\omega)\right\}(t) = \lim_{r\to\infty}\frac{1}{2\pi i}\int_{b-ir}^{b+ir} f(t)\mathrm{e}^{\omega t}\mathrm{d}\omega, \tag{2.2.1.4}$$

provided that $b > \upsilon$, and $i = \sqrt{-1}$. It is entirely possible to derive the explicit form of the Laplace transform, or indeed its inverse, for a particular function from the above definitions together with complex variable calculus. Yet, it is often more convenient to use a suitable table with specific transform formulas, such as the one provided by Råde and Westergren [13].

The first step, in this derivation, will be to transform the PDE in (2.2.1.1) with respect to t. Specifically, given the definition

$$\tilde{c}(x,\omega) = \mathscr{L}\left\{c(x,t)\right\}(x,\omega), \tag{2.2.1.5}$$

and by introducing the explicit Laplace transforms tabulated in the mathe-

matical handbook by Råde and Westergren it can be shown that [13]

$$\begin{aligned}
&\mathscr{L}\left\{\frac{\partial}{\partial t}c(x,t)\right\}(x,\omega) = \mathscr{L}\left\{D\frac{\partial^2}{\partial x^2}c(x,t)\right\}(x,\omega)\\
\Leftrightarrow&\Big\{\mathscr{L}\left\{C_1 f_1(t) + C_2 f_2(t)\right\}(\omega) = C_1\tilde{f}_1(\omega) + C_2\tilde{f}_2(\omega), \qquad (2.2.1.6)\\
&\quad \mathscr{L}\left\{f'(t)\right\}(\omega) = \omega\tilde{f}(\omega) - \lim_{t\to 0-} f(t)\Big\} \qquad (2.2.1.7)\\
\Leftrightarrow&\omega\tilde{c}(x,\omega) - \lim_{t\to 0-} c(x,t) = D\frac{\partial^2}{\partial x^2}\tilde{c}(x,\omega)\\
\Leftrightarrow&\frac{\partial^2}{\partial x^2}\tilde{c}(x,\omega) - \frac{\omega}{D}\tilde{c}(x,\omega) = -\frac{1}{D}\lim_{t\to 0-} c(x,t). \qquad (2.2.1.8)
\end{aligned}$$

Due to the initial condition, which has the form of a step function, it is convenient to solve (2.2.1.8) separately in each of the two domains $x \in]-\infty,0]$ and $x \in]0,\infty[$. This requires, however, that additional boundary conditions are defined, specifically by demanding that the solution is continuous and smooth at $x = 0$ so that

$$\begin{cases}\lim\limits_{x\to 0-} c(x,t) = \lim\limits_{x\to 0+} c(x,t)\\ \lim\limits_{x\to 0-} \dfrac{\partial}{\partial x}c(x,t) = \lim\limits_{x\to 0+} \dfrac{\partial}{\partial x}c(x,t)\end{cases}. \qquad (2.2.1.9)$$

For the case $x \leq 0$, equation (2.2.1.8) can be seen to take on the following form

$$\begin{aligned}
&\frac{\partial^2}{\partial x^2}\tilde{c}(x,\omega) - \frac{\omega}{D}\tilde{c}(x,\omega) = -\frac{1}{D}\lim_{t\to 0-} c(x,t),\ x \leq 0\\
\Leftrightarrow&\left\{(2.2.1.1) \Rightarrow \lim_{t\to 0-} c(x,t)\big|_{x\leq 0} = c_0\right\}\\
&\frac{\partial^2}{\partial x^2}\tilde{c}(x,\omega) - \frac{\omega}{D}\tilde{c}(x,\omega) = -\frac{c_0}{D},\ x \leq 0. \qquad (2.2.1.10)
\end{aligned}$$

It can be easily seen that the general solution to the homogeneous form of this linear differential equation,

$$\frac{\partial^2}{\partial x^2}\tilde{c}(x,\omega) - \frac{\omega}{D}\tilde{c}(x,\omega) = 0,\ x \leq 0, \qquad (2.2.1.11)$$

is given by

$$\tilde{c}_{\text{hom}}(x,\omega) = C_+ \mathrm{e}^{\sqrt{\frac{\omega}{D}}x} + C_- \mathrm{e}^{-\sqrt{\frac{\omega}{D}}x},\ x \leq 0, \qquad (2.2.1.12)$$

since

$$\frac{\partial^2}{\partial x^2}\left[C_+\mathrm{e}^{\sqrt{\frac{\omega}{D}}x}+C_-\mathrm{e}^{-\sqrt{\frac{\omega}{D}}x}\right]-\frac{\omega}{D}\left[C_+\mathrm{e}^{\sqrt{\frac{\omega}{D}}x}+C_-\mathrm{e}^{-\sqrt{\frac{\omega}{D}}x}\right]$$
$$=\left[\left(\sqrt{\frac{\omega}{D}}\right)^2 C_+\mathrm{e}^{\sqrt{\frac{\omega}{D}}x}+\left(-\sqrt{\frac{\omega}{D}}\right)^2 C_-\mathrm{e}^{-\sqrt{\frac{\omega}{D}}x}\right]-\frac{\omega}{D}\left[C_+\mathrm{e}^{\sqrt{\frac{\omega}{D}}x}+C_-\mathrm{e}^{-\sqrt{\frac{\omega}{D}}x}\right]$$
$$=\frac{\omega}{D}C_+\mathrm{e}^{\sqrt{\frac{\omega}{D}}x}+\frac{\omega}{D}C_-\mathrm{e}^{-\sqrt{\frac{\omega}{D}}x}-\frac{\omega}{D}C_+\mathrm{e}^{\sqrt{\frac{\omega}{D}}x}-\frac{\omega}{D}C_-\mathrm{e}^{-\sqrt{\frac{\omega}{D}}x}=0.$$

Meanwhile, the particular solution can be assumed to have the form

$$\tilde{c}_{\mathrm{par}}(x,\omega)=C_{\mathrm{I}}x^2+C_{\mathrm{II}}x+C_{\mathrm{III}},\ x\leq 0. \tag{2.2.1.13}$$

When substituted into (2.2.1.10), this formula yields the equation

$$\begin{aligned}-\frac{c_0}{D}&=\frac{\partial^2}{\partial x^2}\left(C_{\mathrm{I}}x^2+C_{\mathrm{II}}x+C_{\mathrm{III}}\right)-\frac{\omega}{D}\left(C_{\mathrm{I}}x^2+C_{\mathrm{II}}x+C_{\mathrm{III}}\right)\\ \Leftrightarrow -\frac{c_0}{D}&=2C_{\mathrm{I}}-\frac{\omega}{D}C_{\mathrm{I}}x^2-\frac{\omega}{D}C_{\mathrm{II}}x-\frac{\omega}{D}C_{\mathrm{III}}\\ \Leftrightarrow \frac{c_0}{D}&=\frac{\omega}{D}C_{\mathrm{I}}x^2+\frac{\omega}{D}C_{\mathrm{II}}x+\frac{\omega}{D}C_{\mathrm{III}}-2C_{\mathrm{I}},\end{aligned} \tag{2.2.1.14}$$

which is only satisfied, for all $x\leq 0$, if

$$\begin{cases}C_{\mathrm{I}}=0\\ C_{\mathrm{II}}=0\\ C_{\mathrm{III}}=\frac{c_0}{\omega}\end{cases}. \tag{2.2.1.15}$$

In other words,(2.2.1.14) takes on the form

$$\tilde{c}_{\mathrm{par}}(x,\omega)=\frac{c_0}{\omega},\ x\leq 0, \tag{2.2.1.16}$$

which, in turn, means that

$$\tilde{c}(x,\omega)=\tilde{c}_{\mathrm{hom}}(x,\omega)+\tilde{c}_{\mathrm{par}}(x,\omega)\Rightarrow\{(2.2.1.12),(2.2.1.16)\} \tag{2.2.1.17}$$
$$\Rightarrow\tilde{c}(x,\omega)=C_+\mathrm{e}^{\sqrt{\frac{\omega}{D}}x}+C_-\mathrm{e}^{-\sqrt{\frac{\omega}{D}}x}+\frac{c_0}{\omega},\ x\leq 0. \tag{2.2.1.18}$$

On the positive x-axis, meanwhile, the ODE of interest can be seen to be to be identical to the homogeneous equation (2.2.1.11) since

$$\begin{aligned}\{(2.2.1.8)\}\Rightarrow&\frac{\partial^2}{\partial x^2}\tilde{c}(x,\omega)-\frac{\omega}{D}\tilde{c}(x,\omega)=-\lim_{t\to 0-}c(x,t),\ x>0\\ \Leftrightarrow&\left\{(2.2.1.1)\Rightarrow\lim_{t\to 0-}c(x,t)\Big|_{x<0}=0\right\} \qquad (2.2.1.19)\\ \Leftrightarrow&\frac{\partial^2}{\partial x^2}\tilde{c}(x,\omega)-\frac{\omega}{D}\tilde{c}(x,\omega)=0,\ x>0. \qquad (2.2.1.20)\end{aligned}$$

Given that (2.2.1.11) has the solution (2.2.1.12) it must therefore be concluded that

$$\tilde{c}(x,\omega) = C'_{+}\mathrm{e}^{\sqrt{\frac{\omega}{D}}x} + C'_{-}\mathrm{e}^{-\sqrt{\frac{\omega}{D}}x},\ x > 0, \tag{2.2.1.21}$$

wherefore

$$\tilde{c}(x,\omega) = \begin{cases} C_{+}\mathrm{e}^{\sqrt{\frac{\omega}{D}}x} + C_{-}\mathrm{e}^{-\sqrt{\frac{\omega}{D}}x} + \frac{c_0}{\omega}, & x < 0 \\ C'_{+}\mathrm{e}^{\sqrt{\frac{\omega}{D}}x} + C'_{-}\mathrm{e}^{-\sqrt{\frac{\omega}{D}}x}, & x > 0, \end{cases}. \tag{2.2.1.22}$$

The coefficients, C_+, C_-, C'_+ and C'_-, in this expression can be determined with help of the Laplace transform of the boundary condition,

$$\begin{aligned} \{(2.2.1.1)\} \Rightarrow & \begin{cases} \mathscr{L}\left\{\lim\limits_{x\to-\infty} c(x,t)\right\}(x,\omega) = \mathscr{L}\{c_0\}(\omega) \\ \mathscr{L}\left\{\lim\limits_{x\to\infty} c(x,t)\right\}(x,\omega) = 0, \end{cases} \\ \Leftrightarrow & \left\{(2.2.1.6),\ \mathscr{L}\{1\}(\omega) = \frac{1}{\omega}\right\} \qquad (2.2.1.23) \\ \Leftrightarrow & \begin{cases} \lim\limits_{x\to-\infty} \tilde{c}(x,\omega) = \dfrac{c_0}{\omega} \\ \lim\limits_{x\to\infty} \tilde{c}(x,\omega) = 0 \end{cases}. \qquad (2.2.1.24) \end{aligned}$$

In particular, when the formula (2.2.1.22) is introduced in these equations, the following result is obtained

$$\begin{cases} \lim\limits_{x\to-\infty}\left(C_{+}\mathrm{e}^{\sqrt{\frac{\omega}{D}}x} + C_{-}\mathrm{e}^{-\sqrt{\frac{\omega}{D}}x} + \dfrac{c_0}{\omega}\right) = \dfrac{c_0}{\omega}, & x \le 0 \\ \lim\limits_{x\to\infty}\left(C'_{+}\mathrm{e}^{\sqrt{\frac{\omega}{D}}x} + C'_{-}\mathrm{e}^{-\sqrt{\frac{\omega}{D}}x}\right) = 0 & x > 0 \end{cases}$$
$$\begin{cases} C_{+}\lim\limits_{x\to-\infty}\mathrm{e}^{\sqrt{\frac{\omega}{D}}x} + C_{-}\lim\limits_{x\to-\infty}\mathrm{e}^{-\sqrt{\frac{\omega}{D}}x} = 0, & x \le 0 \\ C'_{+}\lim\limits_{x\to\infty}\mathrm{e}^{\sqrt{\frac{\omega}{D}}x} + C'_{-}\lim\limits_{x\to\infty}\mathrm{e}^{-\sqrt{\frac{\omega}{D}}x} = 0, & x > 0 \end{cases}, \tag{2.2.1.25}$$

which can only be satisfied provided that $C_- = 0$ and $C'_+ = 0$. Thus (2.2.1.22) takes on the form

$$\tilde{c}(x,\omega) = \begin{cases} C_{+}\mathrm{e}^{\sqrt{\frac{\omega}{D}}x} + \frac{c_0}{\omega}, & x \le 0 \\ C'_{-}\mathrm{e}^{-\sqrt{\frac{\omega}{D}}x}, & x > 0 \end{cases}. \tag{2.2.1.26}$$

The next step is to use the Laplace transforms of the additional boundary

conditions, (2.2.1.9),

$$\begin{cases} \mathscr{L}\left\{\lim\limits_{x\to 0-} c(x,t)\right\}(x,\omega) = \mathscr{L}\left\{\lim\limits_{x\to 0+} c(x,t)\right\}(x,\omega) \\ \mathscr{L}\left\{\lim\limits_{x\to 0-} \dfrac{\partial}{\partial x} c(x,t)\right\}(x,\omega) = \mathscr{L}\left\{\lim\limits_{x\to 0+} \dfrac{\partial}{\partial x} c(x,t)\right\}(x,\omega) \end{cases}$$
$$\Leftrightarrow \begin{cases} \lim\limits_{x\to 0-} \tilde{c}(x,\omega) = \lim\limits_{x\to 0+} \tilde{c}(x,\omega) \\ \lim\limits_{x\to 0-} \dfrac{\partial}{\partial x}\tilde{c}(x,\omega) = \lim\limits_{x\to 0+} \dfrac{\partial}{\partial x}\tilde{c}(x,\omega) \end{cases}, \tag{2.2.1.27}$$

together with equation (2.2.1.26) to determine C_+ and C'_-

$$\begin{cases} \lim\limits_{x\to 0-} \left(C_+ \mathrm{e}^{\sqrt{\frac{\omega}{D}}x} + \dfrac{c_0}{\omega}\right) = \lim\limits_{x\to 0+} \left(C'_- \mathrm{e}^{-\sqrt{\frac{\omega}{D}}x}\right) \\ \lim\limits_{x\to 0-} \dfrac{\partial}{\partial x}\left(C_+ \mathrm{e}^{\sqrt{\frac{\omega}{D}}x} + \dfrac{c_0}{\omega}\right) = \lim\limits_{x\to 0+} \dfrac{\partial}{\partial x}\left(C'_- \mathrm{e}^{-\sqrt{\frac{\omega}{D}}x}\right) \end{cases}$$
$$\Leftrightarrow \begin{cases} C_+ + \frac{c_0}{\omega} = C'_- \\ \sqrt{\frac{\omega}{D}} C_+ = -\sqrt{\frac{\omega}{D}} C'_- \end{cases}$$
$$\Leftrightarrow \begin{cases} C_+ + \frac{c_0}{\omega} = -C_+ \\ C'_- = -C_+ \end{cases}$$
$$\Leftrightarrow \begin{cases} C_+ = -\frac{c_0}{2}\frac{1}{\omega} \\ C'_- = \frac{c_0}{2}\frac{1}{\omega} \end{cases} \tag{2.2.1.28}$$

Using these conditions (2.2.1.26) can be rewritten onto the form

$$\tilde{c}(x,\omega) = \begin{cases} -\frac{c_0}{2}\frac{1}{\omega}\mathrm{e}^{\sqrt{\frac{\omega}{D}}x} + c_0\frac{1}{\omega}, & x \le 0 \\ \frac{c_0}{2}\frac{1}{\omega}\mathrm{e}^{-\sqrt{\frac{\omega}{D}}x}, & x > 0 \end{cases}. \tag{2.2.1.29}$$

In order to obtain an expression for $c(x,t)$, it is necessary to apply the inverse Laplace transform to (2.2.1.29). Once again, it is convenient to make use of the list of transforms provided by Råde and Westergren, with help of which

it is possible to show that [13]

$$
\begin{aligned}
c(x,t) &= \mathscr{L}^{-1}\left\{\tilde{c}(x,\omega)\right\}(x,t) \\
&= \begin{cases} \mathscr{L}^{-1}\left\{-\frac{c_0}{2}\frac{1}{\omega}\mathrm{e}^{\sqrt{\frac{\omega}{D}}x}+c_0\frac{1}{\omega}\right\}(x,t), & x\leq 0 \\ \mathscr{L}^{-1}\left\{\frac{c_0}{2}\frac{1}{\omega}\mathrm{e}^{-\sqrt{\frac{\omega}{D}}x}\right\}(x,t), & x>0 \end{cases} \\
= \{(2.2.1.6)\} &= \begin{cases} -\frac{c_0}{2}\mathscr{L}^{-1}\left\{\frac{1}{\omega}\mathrm{e}^{\sqrt{\frac{\omega}{D}}x}\right\}(x,t)+c_0\mathscr{L}^{-1}\left\{\frac{1}{\omega}\right\}(x,t), & x\leq 0 \\ \frac{c_0}{2}\mathscr{L}^{-1}\left\{\frac{1}{\omega}\mathrm{e}^{-\sqrt{\frac{\omega}{D}}x}\right\}(x,t), & x>0 \end{cases} \\
&= \left\{(2.2.1.23),\ \mathscr{L}\left\{\mathrm{erfc}\left(\frac{\upsilon}{2\sqrt{t}}\right)\right\}(\omega)=\frac{1}{\omega}\mathrm{e}^{\upsilon\sqrt{\omega}},\ \upsilon>0,\right. \\
&\qquad \text{for } \upsilon = \begin{cases} -\frac{x}{\sqrt{D}}, & x\leq 0 \\ \frac{x}{\sqrt{D}}, & x>0 \end{cases} \Bigg\} \\
&= \begin{cases} -\frac{c_0}{2}\mathrm{erfc}\left(-\frac{x}{\sqrt{D}}\frac{1}{2\sqrt{t}}\right)+c_0, & x\leq 0 \\ \frac{c_0}{2}\mathrm{erfc}\left(\frac{x}{\sqrt{D}}\frac{1}{2\sqrt{t}}\right), & x>0 \end{cases} \\
\Leftrightarrow c(x,t) &= \begin{cases} c_0-\frac{c_0}{2}\mathrm{erfc}\left(-\frac{x}{2\sqrt{Dt}}\right), & x\leq 0 \\ \frac{c_0}{2}\mathrm{erfc}\left(\frac{x}{2\sqrt{Dt}}\right), & x>0 \end{cases}.
\end{aligned}
\tag{2.2.1.30}
\tag{2.2.1.31}
$$

Here, $\mathrm{erfc}(y)$ is the complementary error function, which is related to the error function $\mathrm{erf}(y)$ via

$$\mathrm{erfc}(y) = 1-\mathrm{erf}(y), \tag{2.2.1.32}$$

that is in turn defined as [13]

$$\mathrm{erf}(y) = \frac{2}{\sqrt{\pi}}\int_0^y \mathrm{e}^{-y'^2}\mathrm{d}y'. \tag{2.2.1.33}$$

It has thus been concluded that the solution to the problem (2.2.1.1) is given by the formula

$$c(x,t) = \frac{c_0}{2}\mathrm{erfc}\left(\frac{x}{2\sqrt{Dt}}\right) = \frac{c_0}{2}\left(1-\mathrm{erf}\left(\frac{x}{2\sqrt{Dt}}\right)\right), \tag{2.2.1.34}$$

for $x>0$. Furthermore this expression is identical to formula (eq. 6.2) in Lundgrens thesis, which according to the author yields predictions that are reasonably consistent with experimental data [5].

2.2.2 Semi-infinite domain.

A more physically accurate model for the problem at hand can be formulated by making suitable changes to the boundary and initial conditions defined in (2.2.1.1). In princip, the solution is constrained to the positive half-axis, so that it is defined only for $x \in [0,\infty,[$. Still, the model system will, as before, consist of two domains. One of these, namely $x \in [0,l_h]$, represents the part of the cuvette that contains the buffer solution, which is assumed to have been filled up to a height l_h and have a concentration c_0. The region above, $x \in]l_h,\infty[$, is, on the other hand, assumed to contain the gold sol, in which the citrate concentration equals $c_\infty \ll c_0$, initially. It is, furthermore, appropriate to set the flux J to zero at $x = 0$. According to Fick's first law, (2.2.0.6), this is equivalent to demanding that the concentration gradient vanishes at the same boundary. In other words, the reformulated version of the problem (2.2.1.1) is

$$\begin{cases} \frac{\partial}{\partial t}c(x,t) = D\frac{\partial^2}{\partial x^2}c(x,t) \\ c(x,0) = \begin{cases} c_0, & x \in [0,l_h] \\ c_\infty, & x \in]l_h,\infty[\end{cases} \\ \frac{\partial}{\partial x}c(x,t)\big|_{x=0} = 0 \\ c(x,t) \xrightarrow[x\to+\infty]{} c_\infty \end{cases}, \tag{2.2.2.1}$$

as is also illustrated in figure 2.2.

The steps required to find the solution to (2.2.2.1) will largely be consistent with the ones described in section 2.2.1. In particular, since the PDEs in (2.2.2.1) and (2.2.1.1) are identical, the ODE obtained by Laplace transforming Fick's second law is has the same form as (2.2.1.8),

$$\frac{\partial^2}{\partial x^2}\tilde{c}(x,\omega) - \frac{\omega}{D}\tilde{c}(x,\omega) = -\frac{1}{D}\lim_{t\to 0-} c(x,t). \tag{2.2.2.2}$$

Due to the different initial conditions, however, the right hand sides of equations (2.2.1.8) and (2.2.2.2) are similar but not identical. In particular, by introducing the expression for $c(x,0)$ in (2.2.2.1) into (2.2.2.2) one can deduced that

$$\frac{\partial^2}{\partial x^2}\tilde{c}(x,\omega) - \frac{\omega}{D}\tilde{c}(x,\omega) = \begin{cases} -\frac{c_0}{D}, & 0 \le x \le l_h \\ -\frac{c_\infty}{D}, & l_h < x < \infty \end{cases}. \tag{2.2.2.3}$$

This equation can be seen to have the same form as the ODE (2.2.1.10), in each of the intervals $0 \le x \le l_h$ and $l_h < x < \infty$ respectively. Hence, the

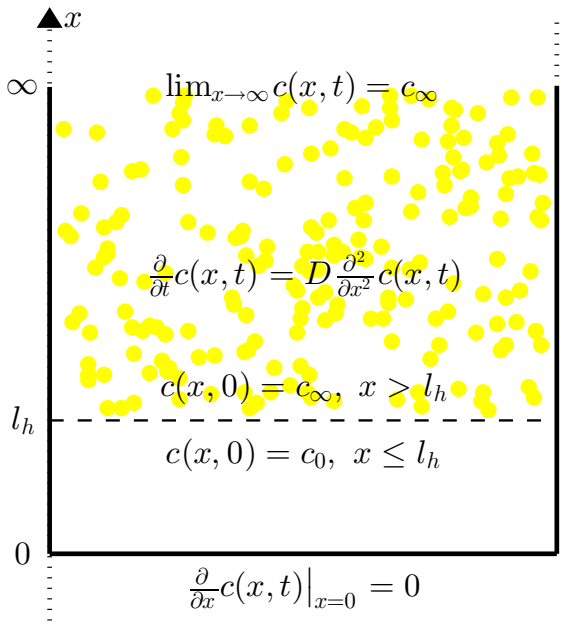

Figure 2.2: Illustration of the system represented by the initial and boundary value problem inequation (2.2.2.1), which describes the diffusion of a single species in a semi-infinite and one-dimensional domain.

solution must be given by (2.2.1.18), provided that the factor c_0 in the third term is substituted for c_∞ in the this case,

$$\tilde{c}(x,\omega) = \begin{cases} C_+ \mathrm{e}^{\sqrt{\frac{\omega}{D}}x} + C_- \mathrm{e}^{-\sqrt{\frac{\omega}{D}}x} + \frac{c_0}{\omega}, & 0 \leq x \leq l_h \\ C'_+ \mathrm{e}^{\sqrt{\frac{\omega}{D}}x} + C'_- \mathrm{e}^{-\sqrt{\frac{\omega}{D}}x} + \frac{c_\infty}{\omega}, & l_h < x < \infty \end{cases} . \tag{2.2.2.4}$$

The formula (2.2.2.4) shall now be simplified with help of the Laplace transforms of the original boundary conditions, which are stated in (2.2.2.1)

$$\begin{aligned} & \begin{cases} \mathscr{L}\left\{\lim_{x\to 0}\frac{\partial}{\partial x}c(x,t)\right\}(x,\omega) = 0 \\ \mathscr{L}\left\{\lim_{x\to\infty} c(x,t)\right\}(x,\omega) = \mathscr{L}\left\{c_\infty\right\}(\omega), \end{cases} \\ \Leftrightarrow\ & \{(2.2.1.6),\ (2.2.1.23)\} \\ \Leftrightarrow\ & \begin{cases} \lim_{x\to 0}\frac{\partial}{\partial x}\tilde{c}(x,\omega) = 0 \\ \lim_{x\to\infty}\tilde{c}(x,\omega) = \frac{c_\infty}{\omega} \end{cases} . \end{aligned} \tag{2.2.2.5}$$

In particular, when (2.2.2.4) is substituted into (2.2.2.5) the result is

$$\begin{cases} \lim\limits_{x\to 0}\dfrac{\partial}{\partial x}\left[C_+\mathrm{e}^{\sqrt{\frac{\omega}{D}}x}+C_-\mathrm{e}^{-\sqrt{\frac{\omega}{D}}x}+\dfrac{c_0}{\omega}\right]=0 \\ \lim\limits_{x\to\infty}\left[C'_+\mathrm{e}^{\sqrt{\frac{\omega}{D}}x}+C'_-\mathrm{e}^{-\sqrt{\frac{\omega}{D}}x}+\dfrac{c_\infty}{\omega}\right]=\dfrac{c_\infty}{\omega} \end{cases}$$

$$\Leftrightarrow \begin{cases} \sqrt{\frac{\omega}{D}}C_+-\sqrt{\frac{\omega}{D}}C_-=0 \\ C'_+\lim\limits_{x\to\infty}\mathrm{e}^{\sqrt{\frac{\omega}{D}}x}+C'_-\lim\limits_{x\to\infty}\mathrm{e}^{-\sqrt{\frac{\omega}{D}}x}=0 \end{cases}$$

$$\Rightarrow \begin{cases} C_+=C_- \\ C'_+=0 \end{cases} \quad \Rightarrow\{(2.2.2.4)\} \tag{2.2.2.6}$$

$$\Rightarrow \tilde{c}(x,\omega)=\begin{cases} C_-\left(\mathrm{e}^{\sqrt{\frac{\omega}{D}}x}+\mathrm{e}^{-\sqrt{\frac{\omega}{D}}x}\right)+\frac{c_0}{\omega}, & 0\le x\le l_h \\ C'_-\mathrm{e}^{-\sqrt{\frac{\omega}{D}}x}+\frac{c_\infty}{\omega}, & l_h<x<\infty \end{cases}. \tag{2.2.2.7}$$

In order to determine C_- and C'_-, it is, as earlier, necessary to introduce extra conditions on $c(x,t)$. In particular, these will be the same as those found in (2.2.1.9). The only exception is that in this case they apply at the interior boundary, $x=l_h$, rather than at $x=0$, and are hence given by the limits,

$$\begin{cases} \lim\limits_{x\to l_h-}c(x,t)=\lim\limits_{x\to l_h+}c(x,t) \\ \lim\limits_{x\to l_h-}\dfrac{\partial}{\partial x}c(x,t)=\lim\limits_{x\to l_h+}\dfrac{\partial}{\partial x}c(x,t) \end{cases}, \tag{2.2.2.8}$$

In accordance with (2.2.1.27), these have the following Laplace transforms

$$\begin{cases} \mathscr{L}\left\{\lim\limits_{x\to l_h-}c(x,t)\right\}(x,\omega)=\mathscr{L}\left\{\lim\limits_{x\to l_h+}c(x,t)\right\}(x,\omega) \\ \mathscr{L}\left\{\lim\limits_{x\to l_h-}\dfrac{\partial}{\partial x}c(x,t)\right\}(x,\omega)=\mathscr{L}\left\{\lim\limits_{x\to l_h+}\dfrac{\partial}{\partial x}c(x,t)\right\}(x,\omega) \end{cases}$$

$$\Leftrightarrow \begin{cases} \lim\limits_{x\to l_h-}\tilde{c}(x,\omega)=\lim\limits_{x\to l_h+}\tilde{c}(x,\omega) \\ \lim\limits_{x\to l_h-}\dfrac{\partial}{\partial x}\tilde{c}(x,\omega)=\lim\limits_{x\to l_h+}\dfrac{\partial}{\partial x}\tilde{c}(x,\omega) \end{cases}. \tag{2.2.2.9}$$

By substituting the solution (2.2.2.7) into (2.2.2.9), it is, in particular, found

that

$$
\begin{aligned}
&\{(2.2.2.9),\ (2.2.2.7)\}\\
\Rightarrow &\begin{cases}
\lim\limits_{x\to l_h-}\left[C_-\left(\mathrm{e}^{\sqrt{\frac{\omega}{D}}x}+\mathrm{e}^{-\sqrt{\frac{\omega}{D}}x}\right)+\dfrac{c_0}{\omega}\right]=\lim\limits_{x\to l_h+}\left[C'_-\mathrm{e}^{-\sqrt{\frac{\omega}{D}}x}+\dfrac{c_\infty}{\omega}\right]\\
\lim\limits_{x\to l_h-}\dfrac{\partial}{\partial x}\left[C_-\left(\mathrm{e}^{\sqrt{\frac{\omega}{D}}x}+\mathrm{e}^{-\sqrt{\frac{\omega}{D}}x}\right)+\dfrac{c_0}{\omega}\right]=\lim\limits_{x\to l_h+}\dfrac{\partial}{\partial x}\left[C'_-\mathrm{e}^{-\sqrt{\frac{\omega}{D}}x}+\dfrac{c_\infty}{\omega}\right]
\end{cases}\\
\Leftrightarrow &\begin{cases}
C_-\left(\mathrm{e}^{\sqrt{\frac{\omega}{D}}l_h}+\mathrm{e}^{-\sqrt{\frac{\omega}{D}}l_h}\right)+\frac{c_0}{\omega}=C'_-\mathrm{e}^{-\sqrt{\frac{\omega}{D}}l_h}+\frac{c_\infty}{\omega}\\
C_-\left(\sqrt{\frac{\omega}{D}}\mathrm{e}^{\sqrt{\frac{\omega}{D}}l_h}-\sqrt{\frac{\omega}{D}}\mathrm{e}^{-\sqrt{\frac{\omega}{D}}l_h}\right)=-\sqrt{\frac{\omega}{D}}C'_-\mathrm{e}^{-\sqrt{\frac{\omega}{D}}l_h}
\end{cases}\\
\Leftrightarrow &\begin{cases}
C'_-\mathrm{e}^{-\sqrt{\frac{\omega}{D}}l_h}+\frac{c_\infty-c_0}{\omega}=C_-\left(\mathrm{e}^{\sqrt{\frac{\omega}{D}}l_h}+\mathrm{e}^{-\sqrt{\frac{\omega}{D}}l_h}\right)\\
-C'_-\mathrm{e}^{-\sqrt{\frac{\omega}{D}}l_h}=C_-\left(\mathrm{e}^{\sqrt{\frac{\omega}{D}}l_h}-\mathrm{e}^{-\sqrt{\frac{\omega}{D}}l_h}\right)
\end{cases}\quad .
\end{aligned}
\tag{2.2.2.10}
$$

From the latter equality in (2.2.2.10), the following relation between the coefficients C_- and C'_- can be deduced

$$
\begin{aligned}
-C'_-\mathrm{e}^{-\sqrt{\frac{\omega}{D}}l_h}&=C_-\left(\mathrm{e}^{\sqrt{\frac{\omega}{D}}l_h}-\mathrm{e}^{-\sqrt{\frac{\omega}{D}}l_h}\right)\\
\Leftrightarrow C'_-&=-C_-\left(\mathrm{e}^{\sqrt{\frac{\omega}{D}}l_h}-\mathrm{e}^{-\sqrt{\frac{\omega}{D}}l_h}\right)\mathrm{e}^{\sqrt{\frac{\omega}{D}}l_h},
\end{aligned}
\tag{2.2.2.11}
$$

which, as is shown below, can be substituted into the former of the two equations to yield an explicit formula for C_-

$$
\begin{aligned}
C'_-\mathrm{e}^{-\sqrt{\frac{\omega}{D}}l_h}-\frac{c_0-c_\infty}{\omega}&=C_-\left(\mathrm{e}^{\sqrt{\frac{\omega}{D}}l_h}+\mathrm{e}^{-\sqrt{\frac{\omega}{D}}l_h}\right)\\
\Leftrightarrow -\frac{c_0-c_\infty}{\omega}&=C_-\left(\mathrm{e}^{\sqrt{\frac{\omega}{D}}l_h}+\mathrm{e}^{-\sqrt{\frac{\omega}{D}}l_h}\right)-C'_-\mathrm{e}^{-\sqrt{\frac{\omega}{D}}l_h}\Leftrightarrow\{(2.2.2.11)\}\\
\Leftrightarrow -\frac{c_0-c_\infty}{\omega}&=C_-\left(\mathrm{e}^{\sqrt{\frac{\omega}{D}}l_h}+\mathrm{e}^{-\sqrt{\frac{\omega}{D}}l_h}\right)\\
&\quad+C_-\left(\mathrm{e}^{\sqrt{\frac{\omega}{D}}l_h}-\mathrm{e}^{-\sqrt{\frac{\omega}{D}}l_h}\right)\mathrm{e}^{\sqrt{\frac{\omega}{D}}l_h}\mathrm{e}^{-\sqrt{\frac{\omega}{D}}l_h}\\
\Leftrightarrow -\frac{c_0-c_\infty}{\omega}&=C_-\left(\mathrm{e}^{\sqrt{\frac{\omega}{D}}l_h}+\mathrm{e}^{-\sqrt{\frac{\omega}{D}}l_h}+\mathrm{e}^{\sqrt{\frac{\omega}{D}}l_h}-\mathrm{e}^{-\sqrt{\frac{\omega}{D}}l_h}\right)\\
\Leftrightarrow -\frac{c_0-c_\infty}{\omega}&=2C_-\mathrm{e}^{\sqrt{\frac{\omega}{D}}l_h}\\
\Leftrightarrow C_-&=-\frac{c_0-c_\infty}{2}\frac{\mathrm{e}^{-\sqrt{\frac{\omega}{D}}l_h}}{\omega}.
\end{aligned}
\tag{2.2.2.12}
$$

Next, an expression for C'_- can be obtained by simply inserting (2.2.2.12)

into (2.2.2.11), with the result [13]

$$C'_{-} = -\left(-\frac{c_0 - c_\infty}{2}\frac{\mathrm{e}^{-\sqrt{\frac{\omega}{D}}l_h}}{\omega}\right)\left(\mathrm{e}^{\sqrt{\frac{\omega}{D}}l_h} - \mathrm{e}^{-\sqrt{\frac{\omega}{D}}l_h}\right)\mathrm{e}^{\sqrt{\frac{\omega}{D}}l_h}$$

$$\Leftrightarrow C'_{-} = \frac{c_0 - c_\infty}{2}\frac{\mathrm{e}^{\sqrt{\frac{\omega}{D}}l_h} - \mathrm{e}^{-\sqrt{\frac{\omega}{D}}l_h}}{\omega}. \tag{2.2.2.13}$$

Given the explicit formulas for the coefficients C_{-} and C'_{-}, (2.2.2.12) and (2.2.2.13) respectively, the Laplace transform of the concentration, $\tilde{c}(x,\omega)$, can be determined by substitting these equations into (2.2.2.7), which yields

$$\begin{aligned}
\tilde{c}(x,\omega) &= \begin{cases} -\frac{c_0-c_\infty}{2}\frac{\mathrm{e}^{-\sqrt{\frac{\omega}{D}}l_h}}{\omega}\left(\mathrm{e}^{\sqrt{\frac{\omega}{D}}x} + \mathrm{e}^{-\sqrt{\frac{\omega}{D}}x}\right) + \frac{c_0}{\omega}, & 0 \le x \le l_h \\ \frac{c_0-c_\infty}{2}\frac{\mathrm{e}^{\sqrt{\frac{\omega}{D}}l_h} - \mathrm{e}^{-\sqrt{\frac{\omega}{D}}l_h}}{\omega}\mathrm{e}^{-\sqrt{\frac{\omega}{D}}x} + \frac{c_\infty}{\omega}, & l_h < x < \infty \end{cases} \\
\Leftrightarrow \tilde{c}(x,\omega) &= \begin{cases} \frac{c_0}{\omega} - \frac{c_0-c_\infty}{2}\left[\frac{\mathrm{e}^{-\sqrt{\frac{\omega}{D}}(l_h-x)}}{\omega} + \frac{\mathrm{e}^{-\sqrt{\frac{\omega}{D}}(x+l_h)}}{\omega}\right], & 0 \le x \le l_h \\ \frac{c_\infty}{\omega} + \frac{c_0-c_\infty}{2}\left[\frac{\mathrm{e}^{-\sqrt{\frac{\omega}{D}}(x-l_h)}}{\omega} - \frac{\mathrm{e}^{-\sqrt{\frac{\omega}{D}}(x+l_h)}}{\omega}\right], & l_h < x < \infty \end{cases},
\end{aligned} \tag{2.2.2.14}$$

From this relation, the concentration profile $c(x,t)$ can be obtained by applying the inverse transform, (2.2.1.4),

$$\begin{aligned}
& c(x,t) = \mathscr{L}^{-1}\left\{\tilde{c}(x,\omega)\right\}(x,t) \\
\Leftrightarrow & \left\{(2.2.1.6),\ (2.2.1.23),\ (2.2.1.30) \text{ for } \begin{cases} \upsilon = \frac{l_h - x}{\sqrt{D}},\ \upsilon = \frac{x+l_h}{\sqrt{D}}, & 0 \le x \le l_h \\ \upsilon = \frac{x-l_h}{\sqrt{D}},\ \upsilon = \frac{x+l_h}{\sqrt{D}}, & l_h < x < \infty \end{cases}\right\} \\
\Leftrightarrow & c(x,t) = \begin{cases} c_0 - \frac{c_0-c_\infty}{2}\left[\mathrm{erfc}\left(\frac{l_h-x}{\sqrt{Dt}}\right) + \mathrm{erfc}\left(\frac{x+l_h}{\sqrt{Dt}}\right)\right], & 0 \le x \le l_h \\ c_\infty + \frac{c_0-c_\infty}{2}\left[\mathrm{erfc}\left(\frac{x-l_h}{\sqrt{Dt}}\right) - \mathrm{erfc}\left(\frac{x+l_h}{\sqrt{Dt}}\right)\right], & l_h < x < \infty \end{cases}.
\end{aligned} \tag{2.2.2.15}$$

In conclusion, the citrate concentration will, according to the model (2.2.2.1), follow the profile

$$c(x,t) = c_\infty + \frac{c_0 - c_\infty}{2}\left[\mathrm{erfc}\left(\frac{x - l_h}{\sqrt{Dt}}\right) - \mathrm{erfc}\left(\frac{x + l_h}{\sqrt{Dt}}\right)\right], \tag{2.2.2.16}$$

for $x \in]l_h,\infty[$. As will be shown in the result section, the agreement between the predictions that can be made using this equation and numerical simulations is very good. Though the deviation from the experimental data is more significant, it is still comparatively small.

2.3 The DLVO Theory & The RSA Model.

The DLVO theory and the RSA model, which are the main subjects of this section, represent fundamental concepts for modelling colloid suspensions. Specifically, the former, which shall be first be presented, provides the formalism needed to describe the interactions that exist between, charged, colloids. The second subsection, meanwhile, is centred around the version of the RSA method that can be used to model the adsorption of such particles on, flat, surfaces.

2.3.1 The DLVO Theory.

The DLVO theory states that the potential arising from the pairwise interactions between colloidal particles is given by the sum [14]

$$u_{\mathrm{tot}}(r) = u_{\mathrm{Born}}(r) + u_{\mathrm{vdW}}(r) + u_{\mathrm{d.l.}}(r). \tag{2.3.1.1}$$

Higashitani further explains that the first term, u_{Born}, represents the so called Born repulsion, which arises when the electron clouds of the particles begin to overlap. This author, moreover, suggests that it is most convenient to assume that this potential becomes infinitely large, and positive, at very short surface-to-surface separations, d. He, specifically, states that

$$u_{\mathrm{Born}}(r) = \begin{cases} +\infty, & r \leq r_{\mathrm{lim}} \\ 0, & r > r_{\mathrm{lim}} \end{cases}, \tag{2.3.1.2}$$

for,

$$d < d_{\mathrm{lim}} = 4\,\text{Å} \tag{2.3.1.3}$$

$$\Rightarrow r < r_{\mathrm{lim}} = \{r = d + 2a_p\} = 4\,\text{Å} + 2 \cdot 5\,\text{Å} \tag{2.3.1.4}$$

$$\Rightarrow r < r_{\mathrm{lim}} = 14\,\text{Å}. \tag{2.3.1.5}$$

Yet, in this project only the terms that represent the, attractive, van der Waals forces, u_{vdW}, and the, repulsive, electric double layer interaction, $u_{\mathrm{d.l.}}$ have been taken into account. Specifically, these contributions can, respectively, be calculated from the formulas

$$u_{\mathrm{vdW}}(r) = -\frac{A_{\mathrm{H}}}{6}\left(\frac{2a_p^2}{r^2 - 4a_p^2} + \frac{2a_p^2}{r^2} + \ln\left(\frac{r^2 - 4a_p^2}{r^2}\right)\right), \tag{2.3.1.6}$$

and

$$u_{\text{d.l.}}(d) = 4\pi a_p^2 Y^2 \left(\frac{k_B T}{e}\right) \frac{1}{d + 2a_p} e^{-d\kappa}, \tag{2.3.1.7}$$

where $d = r - 2a_p$ is the surface-to-surface separation and r the center-to-center distance. Moreover,

$$Y = 8\tanh\left(\frac{e\psi_s}{4k_B T}\right) \frac{1}{1 + \sqrt{1 - \frac{2\kappa a_p + 1}{(\kappa a_p + 1)^2} \tanh^2\left(\frac{e\psi_s}{4k_B T}\right)}}, \tag{2.3.1.8}$$

while

$$\kappa^{-1} = \left[\frac{\varepsilon_r \varepsilon_0 k_B T}{1000 e^2 N_A 2I}\right], \tag{2.3.1.9}$$

is the Debye screening length and

$$I = \frac{1}{2} \sum_i c_i Z_i^2. \tag{2.3.1.10}$$

the ionic strength.

The typical form of the total potential, u_{tot}, as a function of the interparticle distance, is schematically depicted in figure 2.3. This diagram indicates, in agreement with the discussions by, among others, Guozhong as well as Higashitani, that both the van der Waals and the electric double layer terms vanish at sufficiently large, or strictly speaking infinite, separations [15, 14]. As is argued by the former author, the lack of overlap between the electrical double layers in this regime should mean that there is no repulsion [15]. The only interaction of interest should, in other words, be a weak attraction resulting from the van der Waals forces [15]. Provided that the counterion concentration is high enough, so that the double layer repulsion is effectively screened, a minima in the interaction energy may, therefore, appear. If this, so called, secondary minimum is present there is a significant chance for the particles to combine into aggregates through a process normally referred to as flocculation. As can be seen from figure 2.4 this is not always the case, however. This diagram, specifically, shows the interaction potential for the case when gold nanoparticles of size $2a_p = 10$ nm and with an, assumed, surface potential $\psi_s = -50$ mV are suspended in a $c_{\text{Ci}} = 10$ mM buffer solution [1]. For comparison, one could inspect figure 3.7 in section

[1] When calculating the ionic strength, it was assumed that the system had a pH of 4.

3.2, which shows an SEM image of a functionalised gold substrate that has been immersed in a Au NP suspension. Yet, if the interparticle distance is further decreased the ion clouds surrounding the particles will begin to overlap. This should, in turn, lead to an increased repulsion between the individual colloids. As a result, the potential energy curve typically displays a primary maximum, $u_{\mathrm{tot}}^{\mathrm{max}}$, which is known as the repulsive barrier. This terminology stems from the fact that it is only if the thermal energy, $k_B T$, is of the same order of magnitude as the barrier height that the particles can come into close proximity to one another. According to Guozhong, there is only likely to occur if the maximum value $u_{\mathrm{tot}}^{\mathrm{max}} \gtrsim 10 k_B T$. Due to the deep minimum in the potential, which appears at very small interparticle distances, there is, however, a significant chance that the particles will start to agglomerate, if this criterium is reached.

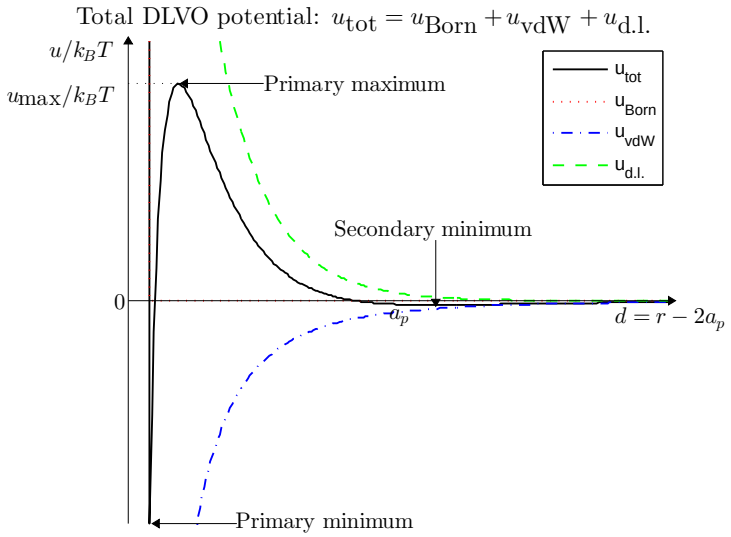

Figure 2.3: Schematic diagram that illustrates the typical dependence of the total interaction potential between two colloidal particles, u_{tot}, on the surface-to-surface distance, d as predicted by the DLVO theory. The corresponding graph, in the form of the black solid curve, has, in accordance with (2.3.1.1), been calculated by summing (2.3.1.2), (2.3.1.6) and (2.3.1.7). The individual contributions from the Born repulsion, red dotted curve, van der Waals attraction, blue dash-dotted curve, and electric double layer interaction, green dashed curved, have also been plotted.

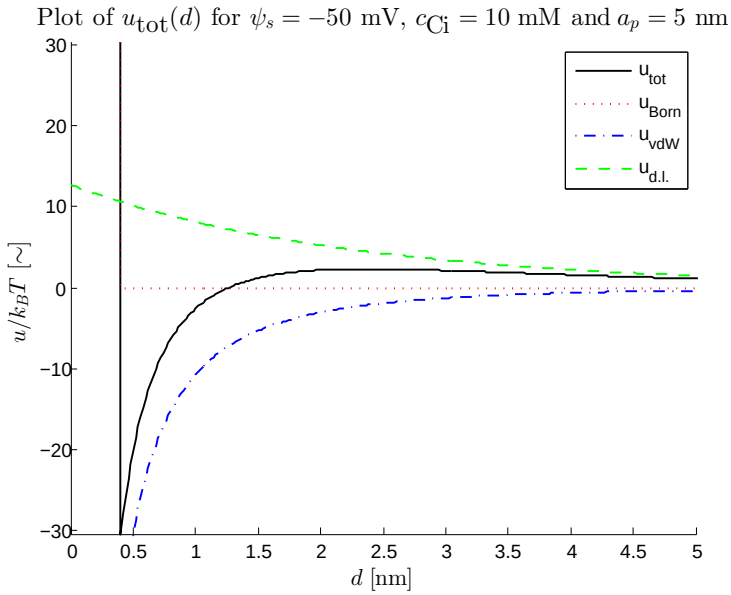

Figure 2.4: Diagram showing the total interaction potential between two colloidal particles, u_{tot}, as a function of the surface-to-surface distance, d, predicted by the DLVO theory. The corresponding graph, in the form of the black solid curve, has, in accordance with (2.3.1.1), been calculated by summing (2.3.1.2), (2.3.1.6) and (2.3.1.7) for $2a_p = 10$ nm, $\psi_s = -50$ mV and $c_{\mathrm{Ci}} = 10$ mM. Moreover, the individual contributions from the Born repulsion, red dotted curve, van der Waals attraction, blue dash-dotted curve, and electric double layer interaction, green dashed curved, have also been plotted.

2.3.2 The RSA Model.

Combining the DLVO Theory with the RSA Model.

The random sequential adsorption, or RSA, model, is a crude but effective Monte-Carlo type method for simulating adsorption processes. According to Adamczyk, Nattich and Batbasz as well as Adamczyk and Warszynski, it is, in its most basic form, based on the following scheme [16, 17]:

1. A virtual adsorbing particle is generated, with a random initial position and orientation.

2. Provided that the, randomly, selected area is unoccupied, the virtual particle will, according to the "localized and irreversible adsorption postulate", stick to the surface with unit probability and, furthermore, remain at this location throughout the entire deposition process.

3. If an overlap exists between the newly arrived and previously deposited particles then the adsorption criterion is not fulfilled and no adsorption

occurs. Instead a new, unbiased, attempt is made, in accordance with the earlier procedure.

4. This process is continued until no more particles can be placed on the surface. At this point, the so called jamming, or maximum packing, limit has been reached and the substrate should be regarded as being "completely covered".

The relatively simple version of the RSA model described above can be made more general by combining it with the DLVO theory. In particular, doing so allows the presence of interparticle interactions to be taken into account, which effectively extends the range of applicability of the former beyond the limiting case of adsorbing hard spheres. The aim is, more precisely, to describe how the presence of such forces can be taken into account by introducing an effective particle radius, within the framework of the RSA model.

According to Semmler, Mann, Rička and Borkovec as well as Lundgren, it is possible to show that the saturation coverage is, in this case, related to the theoretical jamming limit via the formula [5, 18]

$$\theta_p^{\max} = \theta_p^{\text{jam}} \left(\frac{a_p}{a_p^{\text{eff}}} \right)^2 . \tag{2.3.2.1}$$

In agreement with Lundgrens study, it shall be assumed that a_p^{eff} is defined by the equation

$$\frac{u_{\text{tot}}(2a_p^{\text{eff}})}{k_B T} = \frac{1}{\Lambda}, \tag{2.3.2.2}$$

where u_{tot} is the total pairwise interaction potential [5]. While the parameter Λ has no specific physical interpretation, its inverse $1/\Lambda$, consequently, represents the interaction potential for an interparticle separation of $d = 2a_p^{\text{eff}}$. Unsurprisingly, its value, while confined to the interval $1 < \Lambda < \exp(1)$, is most often chosen so as to give the best possible fit between the calculations and the experimental data. Here, it shall, specifically, be assumed that

$$\Lambda = \frac{\exp(1) - 1}{2}, \tag{2.3.2.3}$$

in agreement with Lundgrens thesis work. Yet, one should note that different values have been used in other studies, primarily depending on the nature of the particles and substrates used in the experiments. Semmler, Mann, Rička and Borkovec for example chose $\Lambda = \exp(1)$ [19].

The results presented in this report, as well as Lundgrens study, have been obtained with help of numerical calculations and by assuming that the pairwise interaction potential is given by the sum of the contributions from (2.3.1.6) and (2.3.1.7). Before moving on, it shall be noted that several alternative techniques exist for simulating the absorption of interacting nanoparticles. This not only includes contrasting extensions of the RSA model, but also methods based on entirely different concepts.

Chapter 3

Experiments & Simulations.

The first part of this section will detail the different experimental setups that have been developed, for the purpose of obtaining substrates with well-defined, yet non-uniform, particle coverage. This presentation shall, initially, focus on the setup used by Lundgren to cover functionalised gold surfaces with one-dimensional nanoparticle gradients [5]. This will be followed by a description of the development of methods for immobilising Au NPs in radially symmetric patterns. The purpose of the next section, 3.2, on the other hand, is to introduce the reader to the instruments and computer programs implemented in this project. Firstly, the scanning electron microscope and the ImageJ® software will be presented, in that order. The final part of this section, meanwhile, is dedicated to the, perhaps, most important tool used in this project, namely the COMSOL Multiphysics® software.

3.1 Experimental Setups

As was mentioned earlier, the description of the experimental setups has been separated into two distinctive parts. In the first of the two following subsections, an effectively one-dimensional geometry shall, specifically, be considered. It shall be noted, however, that none of the experiments, performed as part of this study, are related to this geometry. Instead, the measured data presented in section 4.1 was originally obtained by Lundgren and his colleges [1]. For obvious reasons, the presentation of the setups, which were designed for creating radially symmetric particle gradients, that follows thereafter is more detailed. In particular, not only does this subsection give a complete

description of the final geometries, it also includes detailed discussions of the alternative designs that were considered during the development process.

3.1.1 Setup for Creating 1D Gradients

In his PhD thesis, Lundgren presents the so called backfilling approach for coating dithiol covered gold substrates with one-dimensional gradients of gold nanoparticles [5]. As can be seen from the schematic depiction of this method found in figure 3.1, the first step involves immersing the substrate in a cuvette filled with a sol of Au NPs, with a low ionic strength. Since the latter are negatively charged, due to layers of citrate ions bound to the surfaces of the individual colloids, these will repel one another. This effect will, due to screening, be especially strong at such low citrate buffer concentrations. As Lundgrens research has shown, the strength of the double layer repulsion is, moreover, directly related to the spacing between the immobilised particles. Specifically, smaller interparticle distances and a more complete coverage is achieved at higher ionic strengths.

The backfilling method is, as Lundgren states, based on the prospect of controlling the separation between the surface adsorbed colloids by tuning the electrolyte concentration [5]. Specifically, the above discussion implies that the initial particle pattern, which is typically uniform, can be made denser by increasing the buffer concentration. In particular, the injection of a concentrated solution of citrate buffer below the, lighter, nanoparticle suspension will compel the ions to diffuse from the lower to the upper phase. The decrease in the buffer concentration with the distance from the interface can, thus, be modelled as a one-dimensional gradient. As a result, a coverage profile, with a similar shape, should develop on the surface of the substrate, which is immersed in the Au NP sol. In other words, the number of adsorbed particles per unit area should be highest at the bottom of the substrate and, moreover, decrease continuously along its length. This statement is verified by the experiments by Lundgren and his co-workers, as can be seen from their, as of yet unpublished, paper [20].

As a final step in the experimental procedure, one must somehow halt the particle deposition process. In order to hinder the highly concentrated buffer solution and the nanoparticle suspension from mixing, the cuvette should, according to Lundgren, be emptied from the bottom before the substrate is removed [5]. Otherwise, it is likely that the gold colloids, in the suspension, start to coagulate and that the pattern, formed by the immobilised nanoparticles, is ruined. In spite of the relative simplicity of this concept, Lundgrens

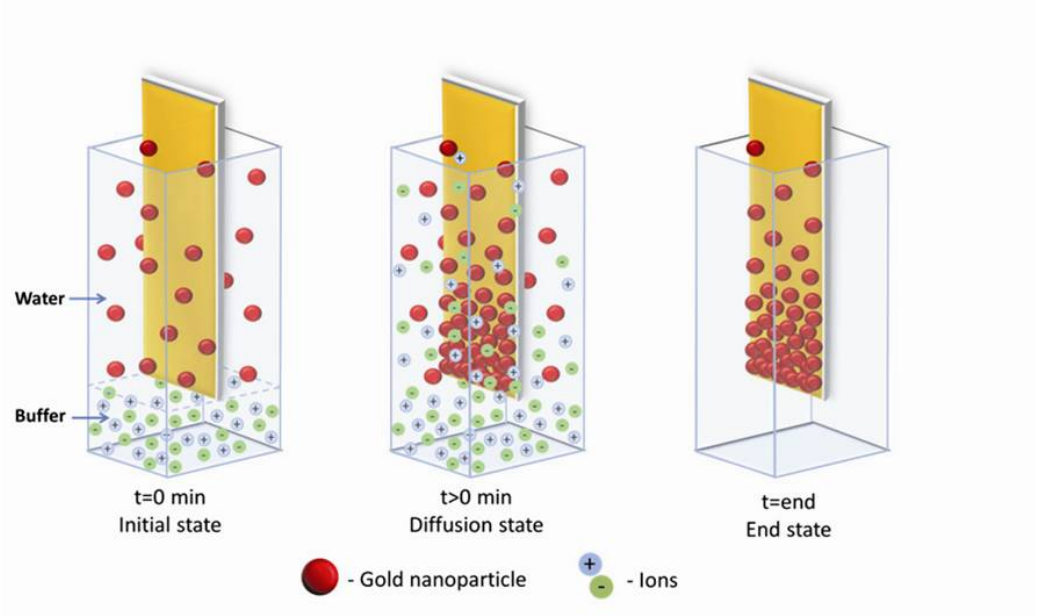

Figure 3.1: A sequence of illustrations, which shows the method, developed by Lundgren, for depositing Au NP gradients on, functionalised, gold surfaces. This procedure involves filling a cuvette with a buffered gold nanoparticle suspension before the substrate is lowered into position. Next, a concentrated citrate buffer is inject at the bottom of the container until the interface reaches the lower edge of the sample. It is, specifically, the deposition process that follows, thereafter, that is schematically depicted in this figure. From left to right, the images shows the system at $t = 0$, moments after the preperatory steps have been completed, for some $t > 0$, during the diffusion process and at $t = \text{end}$, just after the liquid contents have been removed, respectively.

research shows that highly reproducible and practically applicable results can be achieved by following the procedure described above. The fact that the same author has shown that it is possible to treat several samples simultaneously, using this technique, can be seen as further evidence of the success of this approach. As can be seen from figure 3.2, this is achieved by placing the substrates in parallel inside a single channel which is then filled with the Au NP suspension before the concentrated buffer is injected.

3.1.2 Setup for Creating Radially Symmetric Gradients

In this section different experimental setups for coating flat surfaces with radially symmetric nanoparticle gradients, which are conceptually similar to the design sketched in figure 3.3, will be presented. When possible, this will

Figure 3.2: Photograph showing the simultaneous coating of multiple surfaces with gradients of Au NPs. Specifically, the brightly and darkly coloured vertically placed substrates correspond to gold coated glass and silicon substrates respectively. It is, moreover, possible to distinguish a bluish region between the upper nanoparticle suspension, which has a deep red colour, and the, relatively, clear concentrated buffer found at the bottom of the container. Specifically, this intermediate layer is formed due to the coagulation of the particulate matter, which in turn is a result of the high buffer concentration.

include specifications of the suitable components as well as detailed descriptions of how these should be interconnected. It shall be noted that these have been chosen so that they can, almost exclusively, be attached to one another via QUICKFIT® joints. The shapes and sizes of the cone and the socket that make up each joint are specified in terms of a so called NS number, which like the key dimensions for other types of glassware, can be found in the product catalogue from Fisher Scientific [21]. As an aid when trying to interpret these values it is advisable consult the table and the sketch found on page 7 in the product catalogue from Lenz Laborinstrumente, [22].

The next step in the development process was find an appropriate set of component, available from Fischer Scientific, with which the concept illustrated in figure 3.3 could be realised. After having reviewed the relevant product catalogue, it was inferred that an appropriate setup, in the form of "Setup 1" in figure 3.4, could be constructed from the following products, which are listed from top to bottom.

1: (F) Funnel with NS cone ("Tratt, Scilabware, Lenz, QUICKFIT®"). For more information, see page 806 in the Fisher Scientific product catalogue for 2011/12 or page 92 in the laboratory glassware catalogue from Lenz Laborglasinstrumente [21, 22].

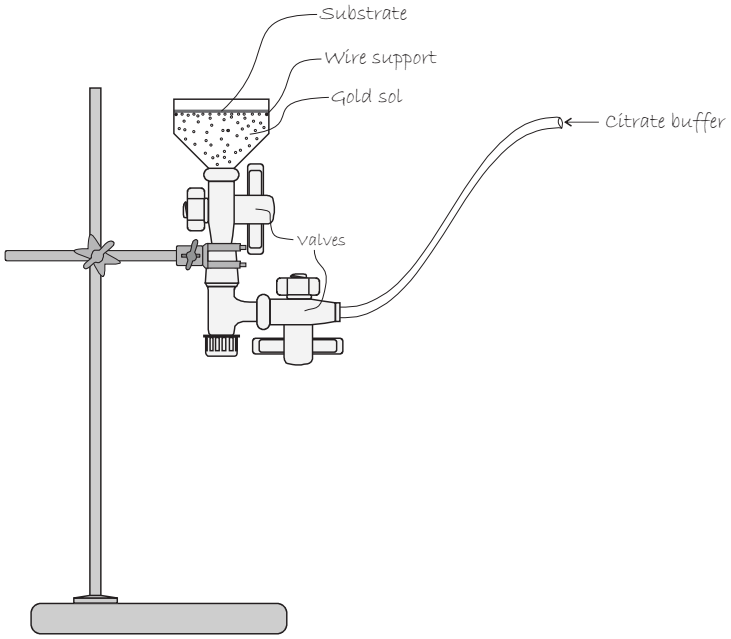

Figure 3.3: Original sketch of a plausible setup, with which a gold substrate, placed near the funnel opening, can be coated with Au NPs. Specifically, by opening the valve to the tube filled with a concentrated buffer solution, the electrolytes should begin to diffuse from the opening in the upper stop cock. This should result in the development of a radially symmetric coverage profile on the bottom face of the sample.

2: **(C)** Connectors with stopcock ("Sammanbinding med kran"). For more information, see page 63 in the laboratory glassware catalogue from Lenz Laborglasinstrumente [22].

3: For example:

(T) Test tube, ground socket ("Provrör, Scilabware, QUICKFIT® med normalslipning för glaspropp"). For more information, see page 640 in the Fisher Scientific product catalogue for 2011/12 [21].

(R) Round-bottom flasks with conical ground joint (Kolvar, Rundkolv med slipning, Scilabware, QUICKFIT®, Lenz). For more information, see page 391 in the Fisher Scientific product catalogue for 2011/12 or page 32 in the laboratory glassware catalogue from Lenz Laborglasinstrumente [21, 22].

As can be seen from the leftmost illustration in figure 3.4, the upper part of the "Setup 1" is made up of a funnel (F), with a height 125 mm and an angle 60°, that is attached to a connector (C) via a QUICKFIT® joint. In addition to the socket, to which the funnel is connected, this component also

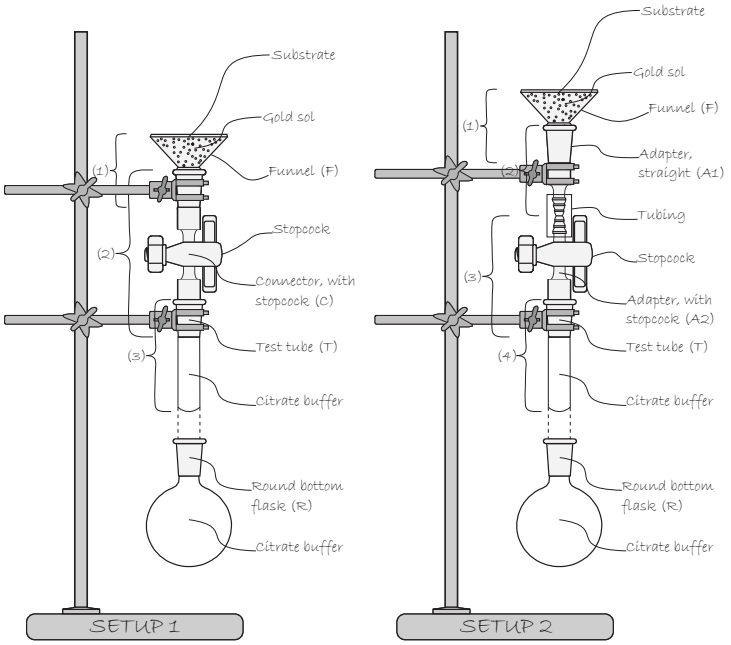

Figure 3.4: Two possible designs, which, hypothetically, could be used to coat substrates with nanoparticle gradients that are radially symmetric. These designs were, in particular, developed so as to be constructable from products supplied by Fischer Scientific.

features a stopcock as well as a cone. If necessary, the default stopcock of the NS 14/23 connector, which has inner hole diameters of 2.5 mm can be replaced with one featuring a somewhat larger bore hole, specifically 4.0 mm. Specifically, both this plug and the two distinctive glass stopcocks found on page 24 in the product catalogue from Lenz have a NS number of 14.5 [22]. The cone end of this middle component should, meanwhile, be attached to some sort of vessel that can hold the concentrated buffer solution. One could, for example, use either a test tube or a round bottom flask, with a suitable volume, given that it features a matching NS socket. Thought there are other possible choices, these two represent relatively simple geometries and are therefore suitable for modelling purposes.

A list of components, similar to the one above, for the alternative geometry, which is labelled "Setup 2" in figure 3.4, can be found below.

1: (F) Funnel with NS cone ("Tratt, Scilabware, Lenz, QUICKFIT®"). For more information, see page 806 in the Fisher Scientific product catalogue for 2011/12 or page 92 in the laboratory glassware catalogue from Lenz Laborglasinstrumente [21, 22].

2: (A1) Adapters, straight ("Adapter, Lenz, rak modell med hylsa och slan-

ganslutning"). For more information, see page 478 in the Fisher Scientific product catalogue for 2011/12 or page 62 in the laboratory glassware catalogue from Lenz Laborglasinstrumente [21, 22].

3: **(A2)** Adapters with NS stopcock, straight ("Adapter, Lenz, rak modell med kärna och kran i glas, plugg 2,5 mm"). For more information, see page 478 in the Fisher Scientific product catalgue for 2011/12 or page 62 in the laboratory glassware catalogue from Lenz Laborglasinstrumente [21, 22].

4: For example:

- **(T)** Test tube, ground socket ("Provrör, Scilabware, QUICKFIT® med normalslipning för glaspropp"). For more information, see page 640 in the Fisher Scientific product catalogue for 2011/12 [21].
- **(R)** Round-bottom flasks with conical ground joint ("Kolvar, Rundkolv med slipning, Scilabware, QUICKFIT®, Lenz'). For more information, see page 391 in the Fisher Scientific product catalogue for 2011/12 or page 32 in the laboratory glassware catalogue from Lenz Laborglasinstrumente [21, 22].

The connector, which was the central part of the previously described setup, has, in this case, been replaced by a pair of tube adapters. As earlier, a QUICKFIT® joint connects the funnel (F) with upper of the two (A1). The latter component is, in turn, attached to the lower adapter (A2), which features a stopcock together with a cone rather than a socket, via a piece of tubing. Similarly to the connector, it ought to be possible to replace the 2.5 mm stopcock with one featuring a 4.0 mm bore hole. The cone end of the lower adapter, meanwhile, is, as in the previous case, attached to a container, for the citrate buffer.

Both of setups described above are, as can be seen from figure 3.4, based on the same experimental procedure. Specifically, all glass components, below the stop cock, are first filled with the concentrated citrate buffer. Once this has been achieved the valve is closed and the upper part of the setup is rinsed clean. Next, a silicon substrate is placed in the funnel, with the gold coated surface facing down, before a sufficient amount of the nanoparticle suspension is added so that the sample completely immersed. The final step is to open the stop cock so that the citrate ions can be allowed to diffuse into the dilute region above the interface. This should give rise to a spherically symmetric concentration gradient, which, when it eventually reaches the lower face of the substrate, should result in a particle coverage profile with a radial symmetry.

Since both “Setup 1” and “Setup 2” were later proven to be unsatisfactory, due to the issues detailed in section 4.4, two other geometries were developed and, eventually, tested. In contrast to the former two cases, the relative positions of the two liquid phases were shifted in the alternative design that was first considered. Thus, the samples are prepared by first placing the gold substrate flat down on the bottom of a glass container, which is then filled with enough gold nanoparticle suspension so that the former is, well and truly, submerged. The concentrated citrate buffer is, thereafter, injected into a piece of tubing, with help of a syringe, until a well defined and nearly flat air-to-liquid interface is formed at the open end of the tube. Next, this tube end is allowed to make contact with the surface of the suspension, at a point directly above the substrate. Since the glass vessel is placed on a platform with an adjustable height, this can be achieved by slowly raising container until the, firmly fixated, tube dips into the solution. Due to the sharp concentration difference the buffer species should, as earlier, diffuse radially outwards from the point of contact between the two phases. This ought to result in a spherically symmetric gradient , which, once it reaches the gold surface, leads to the formation of the sought nanoparticle pattern. As is further explained in section 4.4 the attempts to apply this approach in practice, unfortunately, failed.

The final, and by far the most successful, design is similar to the original sketch, as a comparison between the figures 3.5 and 3.3 reveals. A contrasting feature, however, is that the two liquid phases are not separated via valves in the former case. Instead, this setup relies upon the use of a syringe to fill up the funnel, from below, first with the Au NP suspension and then with the concentrated buffer. The first step is, therefore, to insert a tube into the lower half of the funnel, which is made up of a glass colon. Specifically, one end should be situated a few millimetres above the opening, to the conical part. Next, the substrate is placed vertically above the tube opening. As was explained earlier, a sufficiently large volume of colloid suspension, for the sample to become fully immersed, is then supplied with help of a syringe. An adjustable clamp, which has previously been fastened to the piece of tubing, is then used to hinder the gold sol from pouring out during the next step in the preparation procedure. This, more precisely, involves replacing the empty syringe with one filled with concentrated citrate buffer, which is then carefully injected into the system. If the exactly the right amount of solution is added a sharp liquid-to-liquid interface should form at the end of the tube, which is situated directly underneath the gold coated substrate. Such a result is not easily achieved in practice, however. The main reason for this is that the mainly because the view of the tube opening is obscured,

since it is situated inside the conical part of the funnel. This fact should be apparent from in figure 3.6 and especially the photograph in part (b), which zooms in on the upper half of the setup. Once the two liquids have been brought into contact, the system is left to fend for itself until the buffer gradient has been deemed to have reached the functionalised surface and a radial gradient of Au NP:s has been deposited. At this point, the syringe is withdrawn, which should allow both the buffer and the suspension to pour out of the tube. Only thereafter should the substrate be removed from the funnel and rinsed with water.

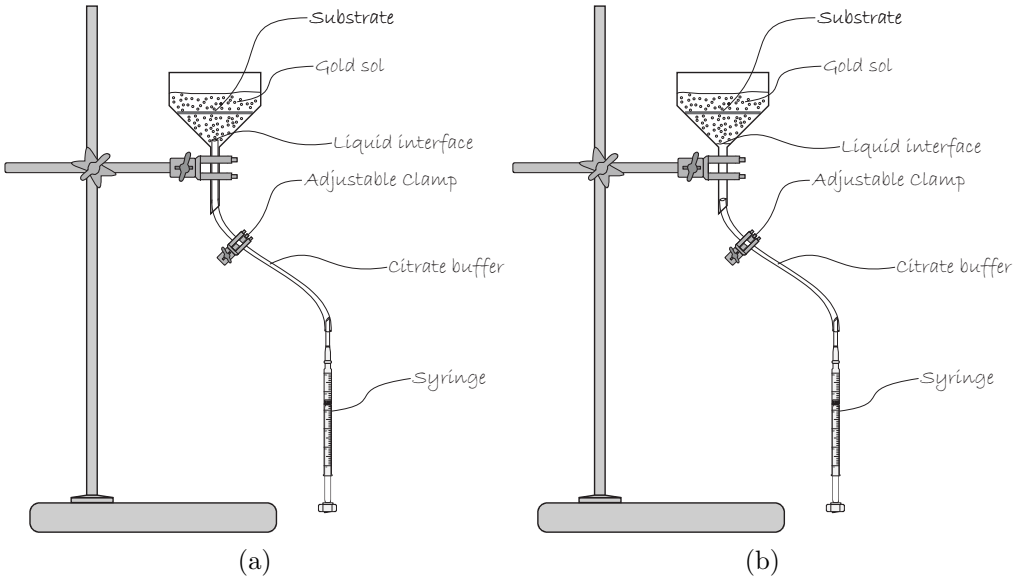

Figure 3.5: Sketches of the final designs for the experimental setup, both of which is made up of a glass funnel into which bottom a rubber tube has been pried. This length of tubing also features a syringe as well as a clamp, which have been inserted into the free end and attached to its mid-section respectively. The difference between the two variants, depicted in part (a) and (b), is that the tube extends into the conical section in the former case but not in the latter. During a typical experiment, a sufficient amount of the nanoparticle suspension is first injected into the system in sufficient amounts that the substrate, which is, thereafter, lowered into the funnel with the gold surface facing down, is going to be entirely submerged. Next, the clamp is tightened before the syringe is removed and refilled with the concentrated citrate buffer. After the latter has been reinserted into the tube, the clamp is loosened and the buffered solution is slowly injected, specifically, until the liquid-to-liquid interface reaches the end of the tube, which is situated directly underneath the substrate. Following this procedure, the system is left to tend to itself for a given period of time, whereafter the diffusion process is interrupted by removing the syringe and letting the liquid pour out.

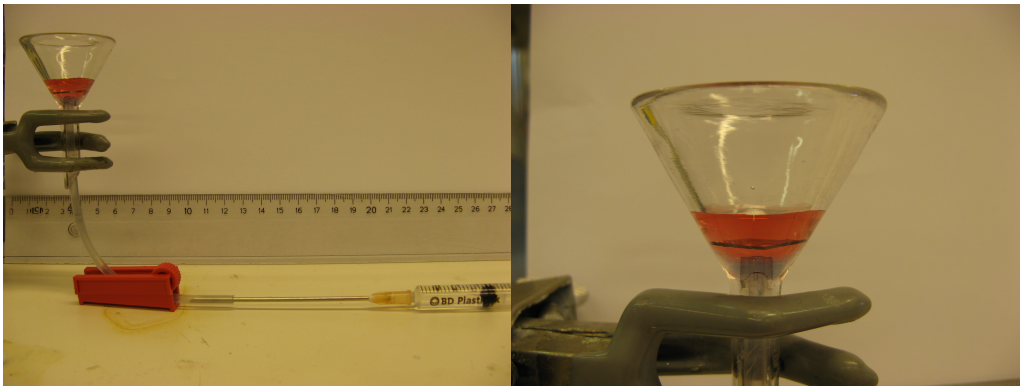

(a) (b)

Figure 3.6: Photographs of the experimental setup schematically depicted in figure 3.5. While part (a) displays all of the components, (b) gives an enlarged view of the conical section of the funnel, inside which both the substrate and the top end of the tube are situated.

3.2 Experimental and Computer Generated Data

Here, the methods, which were used to examine the nanoparticle coated gold surfaces, fabricated using the techniques described in section 3.1.2, as well as the data thus acquired, will be presented. In particular, the first part outlines some general features of scanning electron microscopes, or SEMs, since such an instrument was used to image the samples. In order to quantify the obtained coverage, these images were processed and analysed with the ImageJ® program, which is the subject of the second subsection. Finally, the COMSOL Multiphysics® software package, which was used to simulate the experiments described in section 3.1, will be introduced. This implies that the required input for the ImageJ® and COMSOL Multiphysics® have fundamentally different origins, namely experimental measurements, in the form of SEM images, and a predefined computer models respectively. Even so, the two programs can produce comparable data sets, in the form of the surface coverage at different positions on the functionalised gold surface, as should be evident from the discussion that follows.

Imaging Surfaces with SEM

Since detailing the underlying physics for electron microscopes is beyond the scope of this report, only a brief introduction shall be given. Readers that are keen to learn more, are advised to study the excellent reference literature, for example the textbooks by Petty, Zangwill and Ohring respectively [23, 24, 25]. Generally, the aim of all microscopes is to image any sample as faithfully as possible. For the case of SEMs, this is achieved by scanning an electron beam in a, so called, raster pattern over the substrate. Concomitantly, the secondary electrons, which are emitted from the surface due to the collisions between the electrons in the beam and on the surface respectively, are detected. An image of the sample is, hence, successively built up, pixel by pixel. Moreover, the brightness is, at any given point, directly related to the intensity of the stream of electrons that is emitted when the beam swept over the corresponding position on the sample.

Because the wavelengths of the incident are much lower than that of, for example, visible light, much greater resolution can be achieved than with an optical microscope. In particular, Petty claims that electrons, which are accelerated over a voltage of 100 kV, have a wavelength of about $3.7 \cdot 10^{-3}$ nm. The diffraction limit is, therefore, sufficiently narrow that objects with the atomic sizes can be distinguished. Indeed, particles with sizes on the order of 10 nm are clearly visible in the figure 3.7. This SEM image, more precisely, depicts a reference sample, prepared by immersing a cystiamine functionalised and gold covered silicon substrate in a sol of Au NP:s with a buffer concentration of ~ 10 mM.

3.2.1 Image analysis using ImageJ®

Though the free image analysis software ImageJ® has many possible applications, this brief introduction will only describe the functionalities that are relevant for the project at hand. A much broader and more detailed description can be found in the user's manual [26]. Specifically, the aim was to analyse the SEM images of the surfaces prepared with help of the methods described in section 3.1.2, for the purpose of determining the number of particles per unit area. Therefore, only a handful of the available features had to be implemented. The first step was to define the scale of the image, measured in units of m/pixel. This was achieved by first marking the scale-bar, which, as can be seen from figure 3.7, is found at the bottom of each SEM image, with a line and then clicking on `Analyze/Set Scale...`. Doing so

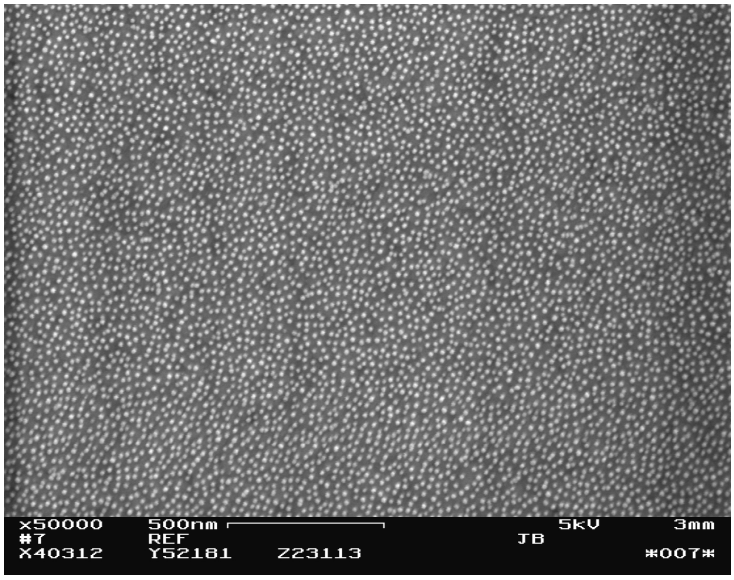

Figure 3.7: SEM image of a reference sample, in the form of a partially cysteamine functionalised and gold covered silicon substrate that has been submerged in an Au NP suspension, with a pH of 4 and a buffer concentration of 10 nm.

will, in particular, bring up a command window, in which the scaling can be defined simple by inputting the length, found on the left side of the bar. Next, the `Image/Adjust/Threshold` command is used to obtain a black and white version of the image, which, by default, is shown in greyscale. This involves choosing the upper and lower limits for the threshold so that only features that are sufficiently bright, or dark, are displayed. In the case of figure 3.7 the result of this procedure is the pattern in figure 3.8.

Before proceeding with the actual measurements, it is necessary to select the type of data that is to be determine. This process reduces to ticking the correct boxes in the list found under `Analyze/Set Measurements...`. For the case at hand it suffices to mark "Area" and "Area fraction". This means the program calculate the total, selected, area and the fraction of this part of the image that is coloured, black, respectively if one clicks on `Analyze/Measure...`. Using the `Analyze/Measure...` command, available from the window that shows the result of these calculations, it is possible to save tabulated values, for example as a `.txt` spreadsheet. The final step is to use the function `Analyze/Analyze Particles...`, which both counts the number of particles in the image and determines their individual areas. From this data, the particle coverage, in units of particles/μm^2, can be determined with help of, for example, MATLAB®.

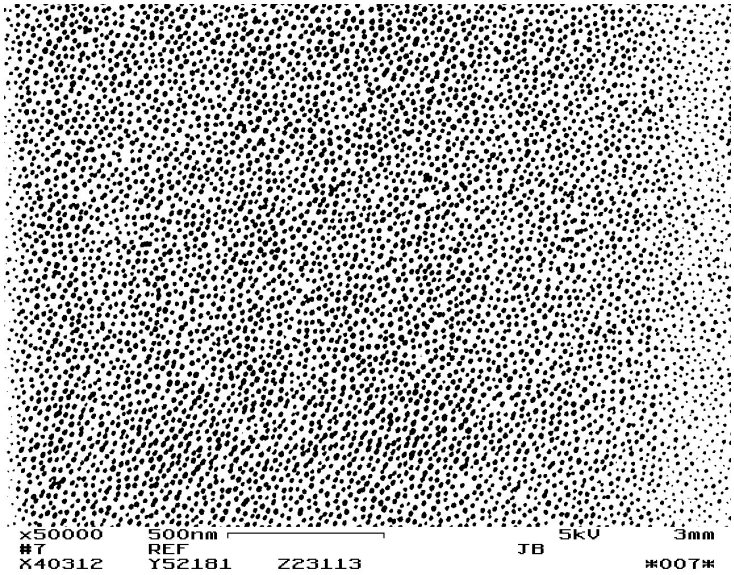

Figure 3.8: Black and white version of the SEM image in figure 3.7, that has been obtained with help of the `Image/Adjust/Threshold` feature of the imageJ® software.

It shall be noted that the method used for determining the total number of particles, in the image, is not optimal, in the sense that it is less accurate than hand-counting all the particles. An alternative, and perhaps more precise, technique is based on the `Process/Find Maxima...` command, which counts all the maxima and, as can be seen from figure 3.9 (a), marks the corresponding positions, with a cross. If the `Noise tolerance` value is chosen correctly, each such maximum should, specifically, represent an adsorbed nanoparticle, which appear bright against the underlying, gold, surface. To determine an appropriate limit, it is convenient to zoom in on an arbitrary area, such as the one shown in figure 3.9 (b). Thereafter, the number in the `Noise tolerance` field is altered, slightly, before the `Preview point selection` box is ticked. This, specifically, tells the program to re-analyse the photograph in terms of the new values on the input parameters, unbiased by any previous calculations. The set of marked points will, hence, successively be updated, allows the relative success of each calculation to be assessed. In particular, special attention should be paid to how many:

1. Crosses found are found in empty regions on the surface,
2. Nanoparticles that have been marked at multiple points,
3. NPs that the program has failed to identify and left unmarked.

If these three numbers are minimised then the optimal value on the `Noise`

`tolerance` has been found. It shall be noted, however, that if this tolerance is set higher then the number of mistakes of the first and second types will increase, at the same time as fewer errors of third kind should be observed. Manual tuning is, therefore, generally required in order to reach this optimum. As is implied by the discussion above, the procedure for determining the particle coverage from the total number of maxima is more time consuming than the one described earlier, which instead made use of the `Analyze/Analyze Particles...` function. Still, more accurate results should, according to the supervisor for this project, be obtained with help of the former technique. During the implementation, it was discovered, however, that the estimates obtained by applying either of the methods were almost the same. For the sake of convenience, only the former of two was used to analyse the SEM images of the surfaces, supposedly, covered by radially symmetric particle gradients.

3.2.2 Estimating the coverage from the citrate concentration.

The most theoretically correct route for predicting the surface coverage that corresponds to a given concentration of citrate ions is to use the formula (2.3.2.1) directly. As was mentioned in section (2.3.2), this involves determining the effective particle radius, a_p^{eff}, by numerically solving equation (2.3.2.2). Firstly though, the total potential u_{tot} must be calculated by summing the contributions from the van der Waals attractions and electric double layer repulsions, which are given by the formulas (2.3.1.6) and (2.3.1.7) respectively. An alternative and simpler approach, especially for implementation purposes, is to use the following approximate relation for the number of particles per square micrometer

$$\underline{N}_p = 37815 \cdot c_{\text{Ci}}^{0.5291}. \tag{3.2.2.1}$$

This formula, more precisely, represents the interpolant to the set of points $(c_{\text{Ci}}, \underline{N}_p)$ generated with help of the procedure described above. Though such an approximation can be deduced in an, effectively, infinite number of ways, this particular parametrisation was determined using a built-in routine, for power regression, in the Microsoft® Excel® 2010 software package. As can be seen from the diagram in figure 3.10, the deviation between the predictions of the formulas (3.2.2.1) and (2.3.2.1), respectively, increases with the citrate concentration c_{Ci}.

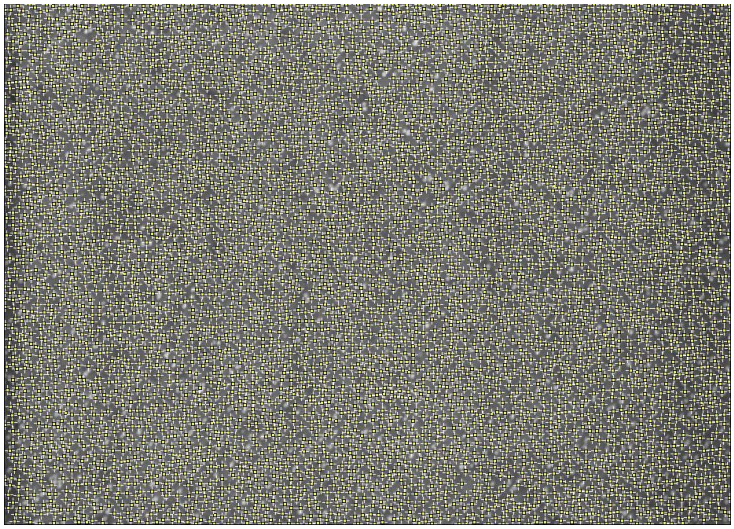

(a)

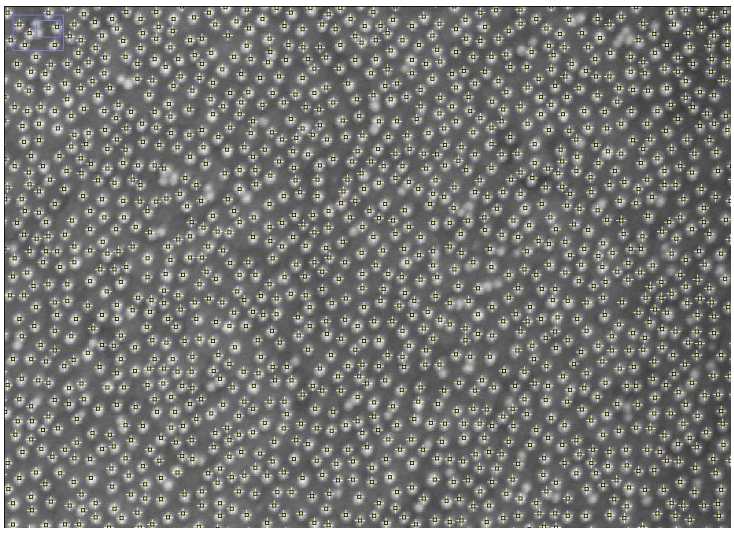

(b)

Figure 3.9: (a): Version of the SEM image in figure 3.7, in which the brightest points has been obtained with help of the `Process/Find Maxima...` feature of the imageJ® software. (b) Zoomed in view of a specific region in (a).

In order to evaluate (2.3.2.1), a number of crucial assumptions, with regards to the physical conditions, must be made. In practice, this reduces to properly choosing the, tunable, parameters that appear in the relevant expressions. Since the systems considered in this project are more or less identical to the ones that have been previously studied by Lundgren, it was deemed appropriate adopt the values that he used in his work [5]. In sum-

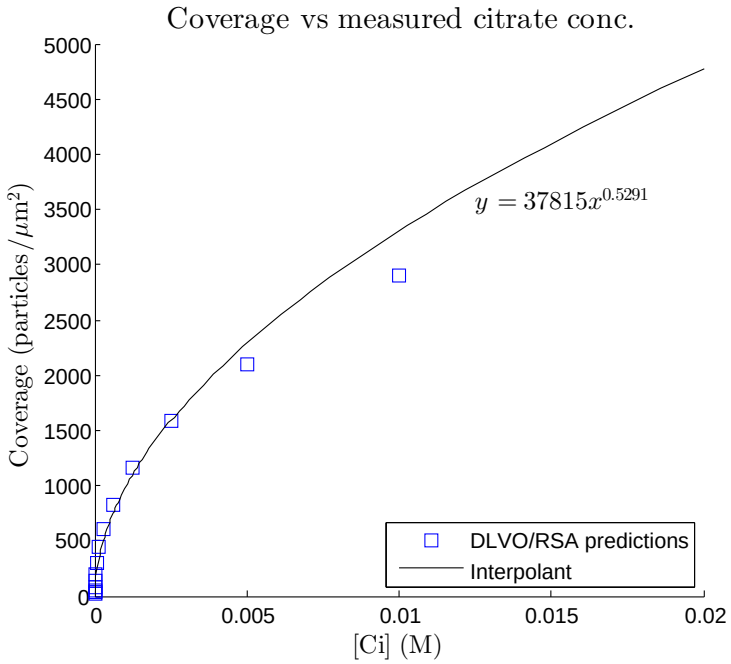

Figure 3.10: Diagram showing the predicted nanoparticle coverage as a function of the citrate concentration that has been calculated using the set of formulas in (3.2.2.2) as well as the corresponding interpolant, which parametrisation is given by (3.2.2.1). Specifically, the data points generated by the solver routine described in the text are marked with the filled blue squares while the black solid line has been derived with help of the predefined power regression model in Microsoft® Excel® 2010.

mary, the following set of formulas were evaluated for a number of different concentrations in the interval of interest, $c_{\mathrm{Ci}} \in]0{,}000001\,\mathrm{M},\ 0{,}01\,\mathrm{M}]$, using the parameter values listed in table 3.1,

$$\begin{cases} \theta_p^{\max} = \theta_p^{\mathrm{jam}} \left(\frac{a_p}{a_p^{\mathrm{eff}}}\right)^2 \\ \frac{u_{\mathrm{tot}}(2a_p^{\mathrm{eff}})}{k_B T} = \frac{1}{\Lambda} \\ u_{\mathrm{tot}}(r) = u_{\mathrm{vdW}}(r) + u_{\mathrm{d.l.}}(r) \\ u_{\mathrm{vdW}}(r) = -\frac{A_{\mathrm{H}}}{6}\left(\frac{2a_p^2}{r^2-4a_p^2} + \frac{2a_p^2}{r^2} + \ln\left(\frac{r^2-4a_p^2}{r^2}\right)\right) \\ u_{\mathrm{d.l.}}(r) = 4\pi a_p^2 Y^2 \left(\frac{k_B T}{e}\right) \frac{1}{r} e^{-(r-2a_p)\kappa} \\ Y = 8\tanh\left(\frac{e\psi_s}{4k_B T}\right) \frac{1}{1+\sqrt{1-\frac{2\kappa a_p+1}{(\kappa a_p+1)^2}\tanh^2\left(\frac{e\psi_s}{4k_B T}\right)}} \\ \kappa^{-1} = \left[\frac{\varepsilon_r \varepsilon_0 k_B T}{1000 e^2 N_A 2I}\right] \\ I = \frac{1}{2}\sum_i c_i Z_i^2 \end{cases} . \qquad (3.2.2.2)$$

Parameter	*Value*
Particle radius, a_p	$5 \cdot 10^{-9}\,\mathrm{m}$
Absolute temperature, T	$298.15\,\mathrm{K}$
Λ	$(\mathrm{e}-1)/2$
Hamakar constant, A_H	$2.5 \cdot 10^{-19}\,\mathrm{J}$
Surface potential, ψ_s	$-0.05\,\mathrm{V}$
pH	4

Table 3.1: List of parameters that were used when evaluating the formulas in (3.2.2.2), in order to determine the particle coverage, $\theta_{\max}$, as a function of the citrate concentration, c_{Ci}.

As is suggested by the last of the above formulas, the individual concentrations, c_i, of all the electrolytes i must be determined, from the total citrate concentration c_{Ci}, before the ionic strength can be calculated.

It should be apparent, from the first expression in (3.2.2.2), that the above procedure only yields a prediction of the percentage of the total surface area that is covered by particles. As is suggested by the description of the method used to analyse the SEM images in section 3.2.1, that approach instead gives a measure of the number of particles per square micrometer. Fortunately, it is relatively straightforward to derive a relation between these two entities. The first step is to note that the relative coverage, θ_p, is defined as the ratio between the sum of the cross sectional areas of the particles $\sum_i A_i^p$ and the total area of the surface A_{tot},

$$\theta_p = \sum_i \frac{A_i^p}{A_{\mathrm{tot}}}. \tag{3.2.2.3}$$

Under the assumption that all of the adsorbed particles can be regarded as perfect spheres with the same size, $2a_p = 10\,\mathrm{nm}$ then their projections on the surface should have a common area

$$A_p = \pi a_p^2 = 25\pi\,\mathrm{nm}^2. \tag{3.2.2.4}$$

This means that the sum in the nominator of (3.2.2.3) simplifies to

$$\sum_i A_i^p = N_{\mathrm{tot}}^p A_p = N_{\mathrm{tot}}^p \pi a^2 = 25\pi N_{\mathrm{tot}}^p\,\mathrm{nm}^2, \tag{3.2.2.5}$$

where N_{tot} is the total number of adsorbed particles. Thus, the number of particles per unit area,

$$\underline{N}_p = \frac{N_{\mathrm{tot}}^p}{A_{\mathrm{tot}}}, \tag{3.2.2.6}$$

and the relative coverage, θ_p, are interrelated via the equation

$$\begin{aligned}
\underline{N}_p = \{(3.2.2.3)\} = \frac{\sum A_i^p}{A_{\text{tot}}} = \{(3.2.2.5)\} = \frac{N_{\text{tot}} A_p}{A_{\text{tot}}} \Leftrightarrow \\
\Leftrightarrow \underline{N}_p = A_p \theta_p \Leftrightarrow \theta_p = \frac{\underline{N}_p}{A_p} \\
\Rightarrow \underline{N}_p = 25\pi\theta_p \,\text{nm}^2 \Leftrightarrow \theta_p = \frac{\underline{N}_p}{25\pi \,\text{nm}^2}
\end{aligned} \tag{3.2.2.7}$$

Naturally, there are some disadvantage with using the regression function (3.2.2.1), rather than the set of equations in (3.2.2.2). The first of these, for instance, suggests that the maximum surface coverage should always less than the jamming limit, since

$$a_p \leq a_p^{\text{eff}} \Leftrightarrow \frac{a_p}{a_p^{\text{eff}}} \leq 1 \Rightarrow \theta_p^{\max} \leq \theta_p^{\text{jam}}. \tag{3.2.2.8}$$

This fact is, however, not taken into account by if the approximate formula, (3.2.2.1), is directly applied. According to this expression, the coverage, specifically, increases monotonically with the citrate concentration instead of saturating at some limiting value. It is especially important to keep this in mind when studying the diagrams in the sections 4.1 and 4.2, which show the predicted number of adsorbed particles per unit area. In fact, the relation (3.2.2.7) can be used to estimate an upper limit for θ_p. Based on the assumption that all of the adsorbed particles have the same physical size, this yields the following result

$$\begin{aligned}
\lim_{c_{\text{Ci}} \to \infty} \underline{N}_p \leq \frac{\theta_p^{\text{jam}}}{A_p} \\
\Rightarrow \lim_{c_{\text{Ci}} \to \infty} \underline{N}_p \leq \frac{0.547}{25\pi} \,\text{particles/nm}^2 \approx 6964.620 \,\text{particles}/\mu\text{m}^2.
\end{aligned} \tag{3.2.2.9}$$

If the influence of polydispersity could, somehow, have been taken into, a higher value on this limit would have been obtained, however. Even so, any predictions, which imply that $\underline{N}_p > 6964.620 \,\text{particles}/\mu\text{m}^2$, are most probably flawed. In other words, any graphs, showing the coverage as a function of the citrate concentration, should asymptotically approach a horizontal line, such that $\underline{N}_p(c_{\text{Ci}}) = \{\text{constant}\} \approx 6964.620 \,\text{particles}/\mu\text{m}^2$, as c_{Ci} increases.

3.2.3 The COMSOL simulations

According to the introduction manual, COMSOL Multiphyisics® has been developed as a tool for simulating different types of model systems [27]. This,

specifically software provides a graphical interface, which allows access to powerful built-in routines for solving coupled physical problems in multiple dimensions. In particular, these solvers, generally, implement different variants of the finite elemental method, or FEM, for this purpose. As is stated in the same manual, one of the advantages with the COMSOL program is that neither specific programming skills nor in depth knowledge of numerics are required in order to achieve practically applicable results. Rather, a reasonable solution should be obtainable given that the user can provides a well-defined geometrical model, together with suitable boundary conditions. The required input arguments, more precisely, include numerical values on the model parameters, which are required in order to specify both the geometry as well as all of the relevant physical processes. Additionally, the user must also choose a suitable mesh, which subdivides the domain into a number of smaller segments. This allows the program to find approximate solutions to the physical problems, defined by the user, by numerically solving the governing differential equations at each node. Thereafter, the obtained result can be processed in a number of different ways. The data can, for example, be displayed in various types of three- or two-dimensional diagrams. Moreover, it is possible to use the solutions to calculate related quantities, such as the flux across a specific boundary.

As is suggest by the above discussion, COMSOL Multiphyisics® can not be successfully implemented unless a thorough analysis of the system of interest has been performed. In the case of molecular transport, which represents the main type of problem studied in this project, this includes determining the diffusion coefficients of all chemical species. It is likely, however, that neither the initially specified parameter values nor the numerical methods correspond to the most optimal choices. Thus, it is advisable to first consider a relatively rudimentary system for which comparable experimental data is readily available. Even without using the predefined optimisation routines, it should be possible to significantly improve the accuracy of the model and increase the efficiency of the solver by successively refining the input arguments while studying the effects of these changes.

As was explained in section 3.1, the main aim of this project is to simulate the diffusion of, charged, chemical species in one- and two-dimensional geometries. Specifically, a model for the 1D case, which corresponds to the setup detailed in section 3.1.1, was first developed. Though the aim was to eventually be able to use the same formalism to simulate the transport in more complex geometries, it was deemed appropriate to allow for improvements of the original formulation to be made beforehand. Still, the built-in modules for solving this type of optimisation problem requires that the constraints,

in this case the sought coverage profile, can somehow be quantified. At the same time, arriving at a suitable expression for the coverage $\underline{N}_p(x)$ as a function of the distance x, which could be provided as an input to the program can be difficult. Simply simulating the system for various ionic strengths and over relatively long time interval, therefore, seemed like a better, yet, less sofisticated alternatives. Specifically, by plotting these results in appropriate diagrams, which are found in the sections 4.1 and 4.2, conclusions could be drawn as to how to choose the input arguments in order to achieve a, sufficiently, good agreement between the predictions and the measurements.

Once the model parameters had been optimised, the next step was, as was mentioned earlier, to turn to more complicated model systems. In particular, the goal was to be able to predict how the concentration gradient in the experimental setups described in section 3.1.2 would develop over time. The discussion in section 4.2 will, moreover, reveal that such simulations were not only used as references for the experimental measurements. Instead, the COMSOL Multiphysics® software was used repeatedly during the entire development process, as was detailed in section 3.1.

The simulations of the experiments, described in sections 3.1.1 and 3.1.2, were, more precisely, performed by implementing the "Transport of Diluted Species" module for specific geometries. In the next sections, the COMSOL Multiphysics® graphical interface will be introduced in relatively general terms. It shall be noted that of the physical interfaces, which each belong to specific predefined module, have all been developed for tackling a certain type of problem. Though this means that the corresponding modelling environments differ in many respects, it is neither practically feasible nor appropriate to present all of them here. Still, it is worth mentioning that extensive documentation, including introductions to each of the above mentioned modules as well as complete descriptions of all available features, is available [27, 28].

The graphical interface.

According to the user manual for the "Chemical Engineering" module, the "Transport of Diluted Species" interface, which is classified under the "Chemical Species Transport" branch, "has the equations, boundary conditions, and rate expression terms for modelling mass transport of diluted species in mixtures, solutions and solids, solving for the species concentrations" [10]. Hence, the software can use the built-in routines to calculate the individual concentrations of multiple chemical species as a function of space and time in a geom-

etry of arbitrary dimensionality, provided that certain physical parameters have been specified. The requirement that the solution should be dilute, in practice means that the concentration variables, solved for, must be at least an order of magnitude lower than that of the solvent. As was explained already in section 2.1, three distinctive types of transport mechanisms, namely diffusion, convection and migration, can be simultaneously simulated within the framework of this model. Mathematically, the first of these phenomena is described by Fick's first, (2.1.1.1), and second, (2.1.1.3), laws, which are discussed in section 2.1. The contributions from the latter two, meanwhile, are taken into account through the inclusion of the third and fourth terms on the left hand side of equation 2.1.1.4 respectively. Furthermore, the mass balance equation must be formulated so as to take into account that the transported species may take part in different types of chemical reactions. The corresponding conversion rates are, therefore, included among the many different input arguments, which must be specified in order for the program to be able to solve transport problems of this type.

One of the key features of the 4.2 version of the COMSOL Multiphyisics® software, is the reworked desktop. In the general user manual, it is, specifically, stated that the main idea is that the user should be able to control all aspects of the simulation with help of a limited number of different windows [27]. As is suggested by the screen shot in figure 3.11, the "Model Builder" tree is the most central part of the graphical interface since it allows access to a number of distinctive nodes, each of which concerns a specific aspect of the computer model. By left-clicking on one of the points in this list the "Settings" window is activated and brings up a number of different options that are associated with the chosen item. In this part of the desktop, the user can both specify the required input arguments and to choose if the available optional features should be activated or not. If the same node is right-clicked, instead, the so called "context menu" appears, from which a number of distinctive actions can be selected. Though these menus represent, perhaps, the most important part of the graphical interface, it shall also be noted that each is unique and may even change depending on the nature of the model environment. The entire modelling process is, in fact, controlled by choosing which of the features, listed in the "context menus", that the program shall implement during the corresponding part of the simulation.

For the sake of clarity only a handful of the available options associated with the different nodes in the "Model Tree" are going to be discussed in this section. For the example at hand at least, the default settings can, therefore, be left unchanged in all fields in the "Settings" windows that are not specifically mentioned.

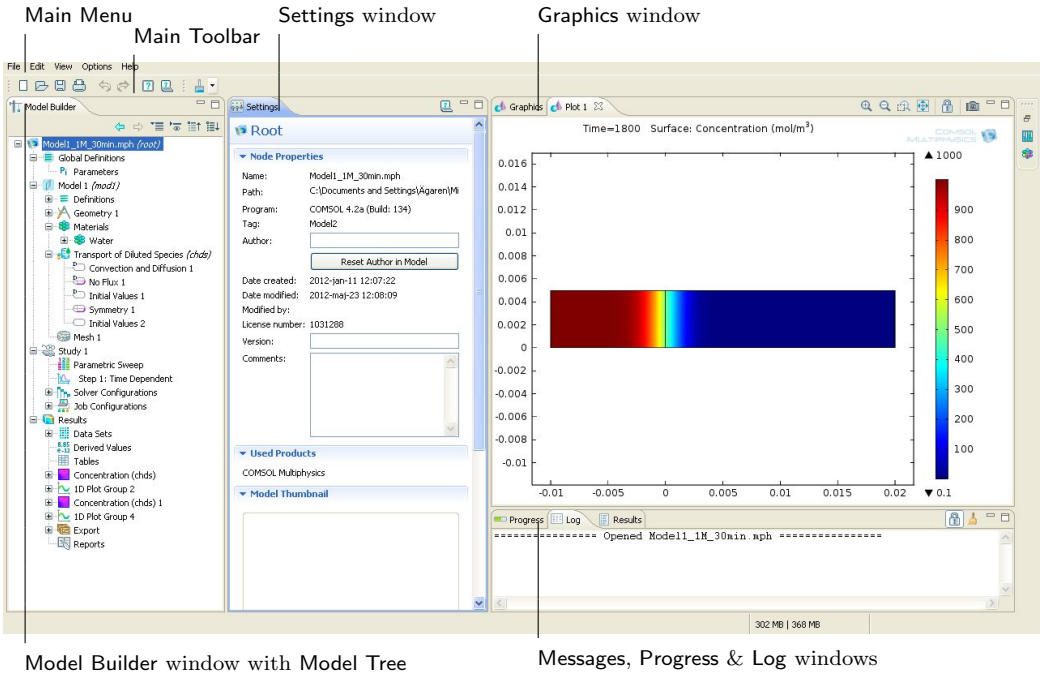

Figure 3.11: Screen shot of the COMSOL Multiphyisics® desktop, from which some of the key windows and menus can be distinguished.

Chapter 4

Results & Conclusions

In this chapter, the results of the experimental procedures and computer simulations described in chapter 3 will be both presented, compared and discussed. For convenience this discussion will be divided into two parts, which focus on the experimental setups developed for the purpose of achieving one-dimensional and radially symmetric particle gradients respectively. In particular, the former case will the subject of the first subsection while the second deals with the latter.

4.1 Measured and simulated 1D gradient

Here, the predicted and measured particle coverage, related to the experimental procedure described in section 3.1.1, will be presented. The former, calculated, results are, specifically, based on both the analytical solution to the 1D diffusion problem and the COMSOL Multiphysics® simulations, which are detailed in sections 2.2 and 3.2 respectively. In order to determine the accuracy of these estimates, they will be compared with experimental data, in the form of some of the measurements presented by Lundgren in his PhD thesis [5]. As should be apparent from section 2.2, a number of key parameters exist, which can be used to characterise any given model system. In terms of these, the experimental procedure at hand can be described as follows:

1. A silicon substrate, which has been covered, on one side, first with a thin gold film followed by an octanedithiol SAM, is lowered into a cuvette.

2. The vessel is filled with a $c_\infty = 50\,\mu$M and pH of 4 citrate solution, in which 10 nm gold nanoparticles had been suspended.

3. A $c_0 = 1$ M buffer, with the same pH, is injected at the bottom of the cuvette, up to a height $l_h = 1$ cm.

4. The citrate is allowed to diffuse, from concentrated to the dilute region, during $t = 90$ min.

The diagram in figure 4.1 shows the two different analytical solutions to the one-dimensional diffusion problem, which corresponds to the experimental procedure described in section 3.1.1, derived in the sections 2.2.1 and 2.2.2. Specifically, the red dashed curve represents the simpler of the two models, (2.2.1.34), while the black solid graph corresponds to the more complex case, (2.2.2.16). The results from the computer simulation of the same system, meanwhile, is displayed by the blue dot-dash line. As can be seen from this diagram, there is a relatively good correspondence between all three predictions. At the lower half of the interval, $-11\,\text{cm} \leq x \leq 0\,\text{cm}$, the solid black and blue dot-dash curves are almost indistinguishable thanks to the fact the same boundary condition,

$$\frac{\partial}{\partial x} c_{\text{Ci}}(x,t)\big|_{x=-l_h=-1\,\text{cm}} = 0,$$

is implemented in both cases. Concomitantly, it can be concluded, from a comparison with the red dashed curve, that the less complex analytically solvable problem yield almost the same result, for $x < 0$, even though it is assumed that $c_{\text{Ci}}(x,t) \xrightarrow[x\to-+\infty]{} c_0$ in this case. Yet, it is in the most relevant part of the interval, $0\,\text{cm} < x < 1\,\text{cm}$, where x is the distance from the interface between the concentrated and more dilute buffer solution, that the largest differences can be found.

Diagram 4.1 (b), which gives a more detailed view of the subinterval $0.4\,\text{cm} < x < 0.7\,\text{cm}$, reveals that the calculations based on the, relatively, simple analytical solution shows a stronger deviation from the predictions of the more accurate models as x increases. This should be expected, however, since the main difference between the three distinctive models is the boundary condition for large values on x. Specifically, the simplest model relies on the assumption that $c_{\text{Ci}}(x,t) \xrightarrow[x\to+\infty]{} 0$, while setting $c_{\text{Ci}}(x,t) \xrightarrow[x\to+\infty]{} c_\infty$ yields the more complex expression. The COMSOL Multiphysics® calculations, on the other hand, is based on a physically sounder condition, namely that there is no flux of citrate ions at the upper surface of the suspension, 1 cm above the

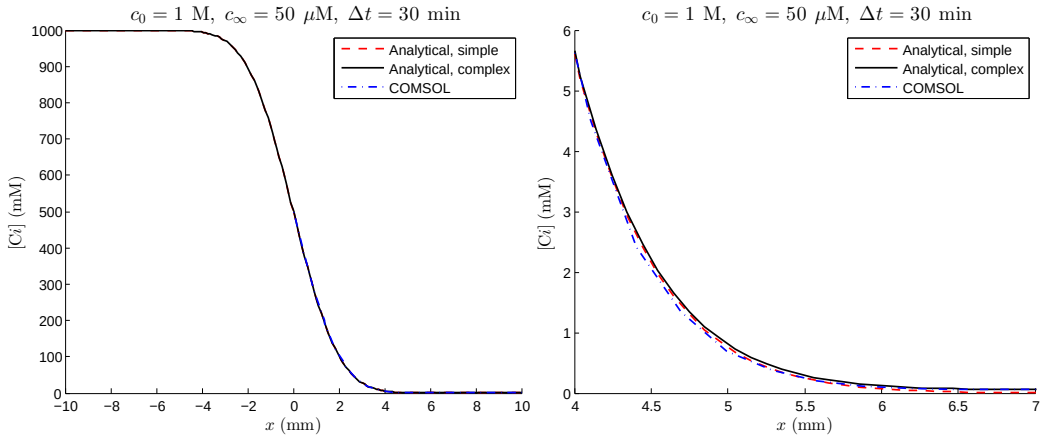

Figure 4.1: Diagrams that display the theoretical predictions of the citrate concentration, which can be achieved with the experimental setup described in section 3.1.1. Specifically, the red dashed and black solid curves respectively represent the analytical solutions to simpler and more complex of two mathematical models presented in section 2.2. The blue dot-dash line, on the other hand, shows the result of the simulations with the COMSOL Multiphysics® software. Physically, these graphs represents the particle coverage after 90 min given that the initial citrate concentrations equalled 1 M and 50 μM in the lower concentrated buffer and the upper dilute suspension respectively. Part (a), in particular, shows the predicted number of adsorbed nanoparticles per unit area, for $-1\,\text{cm} \leq x \leq 1\,\text{cm}$, where x is the distance from the liquid-liquid interface. As can be seen from diagram (b) the discrepancy between the blue dot-dashed and black solid curves is the largest in the intermediate region $0.4\,\text{cm} \leq x \leq 0.7\,\text{cm}$.

interface,

$$\frac{\partial}{\partial x} c_{\text{Ci}}(x,t)\big|_{x=1\,\text{cm}} = 0.$$

Therefore, the predictions will deviate the most from one another for intermediate values on x. As can be seen form part (b) of figure 4.1, the discrepancy is, indeed, the largest for $0.4\,\text{cm} \leq x \leq 0.7\,\text{cm}$. Finally, it shall be noted that the initial condition are more or less similar for all three models, namely that the concentration profile, at $t = 0$, is given by a step function,

$$c_{\text{Ci}}(x,0) = \begin{cases} c_0, & x \leq 0 \\ c_\infty, & x > 0 \end{cases},$$

though with $c_\infty = 0$ for the simplest case.

The accuracy of the predictions, presented earlier, can only be assessed by comparing them with experimental data, here in the form of the measurements provided by the supervisor for this project. These have, more precisely,

been conducted in accordance with the procedure described in section 3.1.1, as part of a study by Lundgren and colleges [20]. If plotted together with the coverage profiles that correspond to the concentration gradients displayed in figure 4.1, the diagram in figure 4.2 results. Though the predicted curves deviate from the measurements, which have been marked by asterisks, the discrepancy is generally relatively small. This indicates that the solutions, obtained by solving the, more complex, problem analytically and with help of the COMSOL Multiphysics simulations respectively, capture the most essential physics that are involved in this process. It is particularly encouraging that the slopes of the corresponding curves, which give a measure of the sharpness of the gradient, are almost the same, especially for $x \gtrsim 0.5\,\text{cm}$.

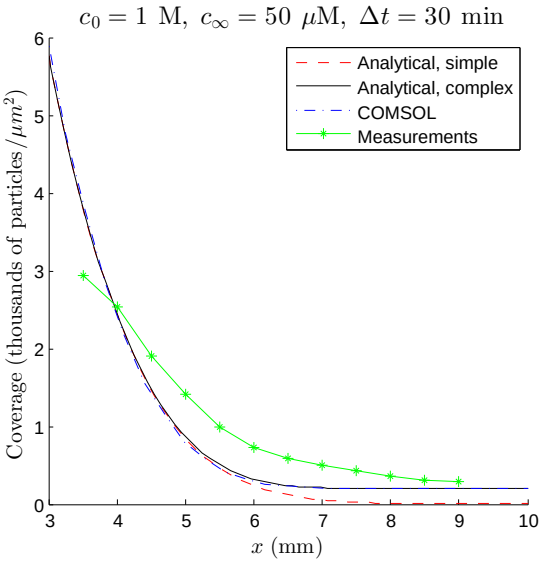

Figure 4.2: Diagram that displays the nanoparticle coverage, as a function of the distance, x, from the liquid-liquid interface, which should be obtained with the, one-dimensional, experimental setup described in section 3.1.1. Specifically, the red dashed and black solid curve respectively represent the analytical solutions to simpler and more complex of two mathematical models described in section 2.2. The blue dot-dash line, on the other hand, shows the result of the simulations with the COMSOL Multiphysics® software. Comparable experimental data, which is represented by the green asterisks, have also been included. Specifically, these results give the particle coverage after 30 min given that the citrate concentration initially equalled 1 M and 50 μM in the lower concentrated buffer and the upper dilute suspension respectively.

As can be seen from figure (4.2), experimental data is only available for $x \gtrsim 0.3\,\text{cm}$, mainly because the measurements becomes less accurate as the distance from the interface decreases. This unreliability can, in turn, be traced back to the fact that salt concentration is relatively large close to the

concentrated buffer.Since the chance for coagulation increases with the ionic strength of the electrolyte, aggregates are more likely to form and become deposited on the target surface in regions where the citrate concentration is higher. Since these congregations, of nanoparticles, are more strongly affected by the gravitational field, their formation can lead to sedimentation, which, due to drag, gives rise to convective currents. Because the resulting bulk fluid motion will carry with citrate ions with it, the transport of these species will no longer be diffusion-governed close to $x = 0$, as the theoretical models assume. On relatively short time-scales, however, such effects should be limited to a relatively small region around $x = 0$, as figure 4.3 implies. According to this diagram, which was obtained by evaluating (2.2.2.16) for $c_0 = 1\,\mathrm{M}$ and $c_\infty = 50\,\mu\mathrm{M}$ at various points in time, the coverage profile should remain very sharp several hours after the diffusion process was initiated.

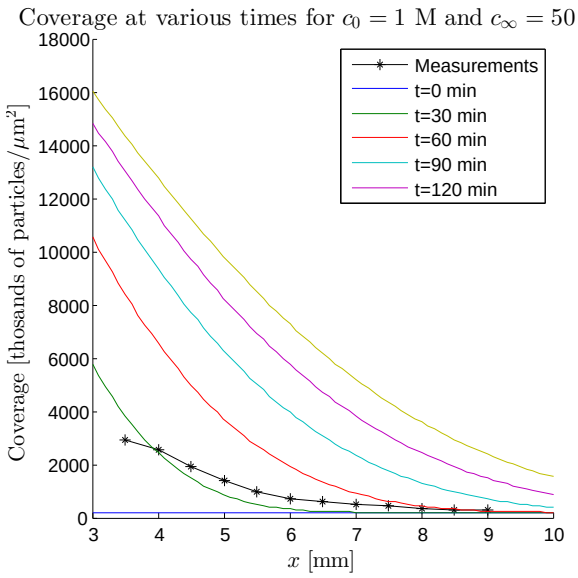

Figure 4.3: Diagram that shows the nanopartcle coverage predicted by the mathematical model of the one-dimensional diffusion problem described in section (2.2.2). Specifically, the graphs have been obtained by plotting the solution (2.2.2.16), as a function of the distance x from the bottom of the substrate, at certain times $0\,\mathrm{min} \leq t \leq 150\,\mathrm{min}]$ min after the concentrated buffer solution was introduced into the system. When evaluating this expression it has, furthermore, been assumed that the initial concentrations of citrate ions in the lower concentrated and the upper dilute phases were 1 M and 50 μM respectively. Additionally, the asterisks correspond to the measured coverage after 30 min given that the citrate concentration initially equalled 1 M and 50 μM in the lower concentrated buffer and the upper dilute suspension respectively.

Though the theoretical calculations agrees relatively well with the experimental data, there still exists much room for improvements, as can be seen from figure 4.2. In particular, it may, depending on the specific model used, be possible to obtain a better fit by tuning certain parameters. While it is difficult to find convincing arguments for changing the diffusion coefficient, for the citrate ions, from the value $D_{\mathrm{Ci}} = 6.904 \cdot 10^{-6}\,\mathrm{cm}^2/\mathrm{s}$, found in literature [29]. Yet, it shall be noted that this numerical value is, strictly, only applicable at infinite dilution, which is clearly not a good approximation across the entirety of the relevant interval $-1\,\mathrm{cm} \leq x \leq 1\,\mathrm{cm}$ [29]. Altering the citrate concentration in the Au NP suspension is less controversial, however, since this entity was not accurately measured during the experiments. Yet, the results only depends relatively weakly on this parameter. As can be seen from figure 4.4, changing the value on c_∞ from $10\,\mu\mathrm{M}$ to $110\,\mu\mathrm{M}$ only has a noticeable effect on the predictions in the region farthest from the interface. According to figure 4.5, one can, however, significantly shift the coverage profile without altering the slope, by varying the strength of the concentrated buffer. Even if it should not be regarded as a fitting parameter, it is interesting to study the dependence of the coverage on this concentration for the purpose of discerning how the experiment should be set up in order to achieve a particular result. Still, it is not advisable to change the buffer concentration arbitrarily, since the likelihood of aggregation increases with the ionic strength, as was mentioned earlier.

From the above discussion, is apparent that the predictions of the most accurate, and analytically solvable, formulation of the one-dimensional diffusion problem agrees remarkably well with the COMSOL Multiphysics® simulations. For this reason, it might seem unnecessarily complicated to implement the latter program for modelling the physical situation at hand. It should, in particular, be simpler to use the analytical solution, (2.2.2.15), to determine how the values on the process parameters should be chosen in order to obtain a specific coverage profile. Furthermore, this approach is advantageous since the named formula can be evaluated relatively easily, even without the aid of a computer. Specifically, the right hand side of equation (2.2.2.15) is nothing but a weighted sum of error functions, which are tabulated, for a range of different arguments, in most mathematical handbooks, such as the one written by Råde and Westergren [13].

As will be further discussed in section 4.5, there are reasons to believe that it should be beneficial to increase the level of complexity of the physical model, on which the predictions presented above have been based. In particular, the problem is, in reality, not confined to the transport of a single type of, neutral, solute molecules within an infinitely dilute solution. Rather, one should

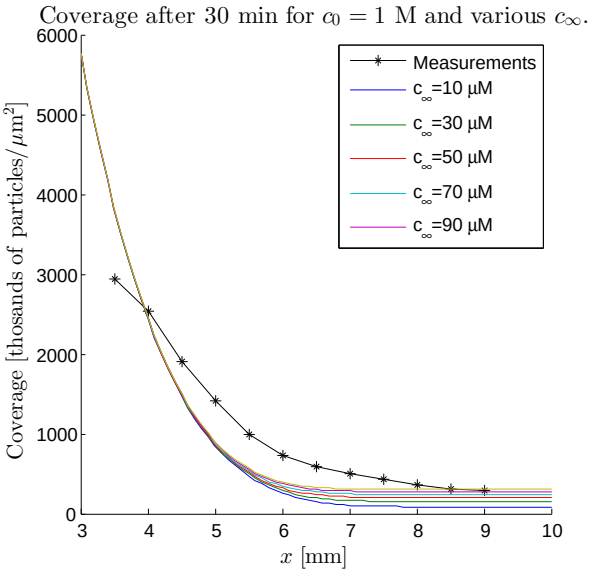

Figure 4.4: Diagram showing the nanoparticle coverage predicted by the mathematical model of the one-dimensional diffusion problem described in section (2.2.2). Specifically, the graphs have been obtained by plotting the solution (2.2.2.16), as a function of the distance x from the bottom of the substrate, 30 min after the concentrated buffer solution was introduced into the system. When evaluating this expression it has, furthermore, been assumed that $c_{\mathrm{Ci}}(x,0) = c_0 = 1\,\mathrm{M}$ for $x < 0$, while the initial buffer concentration in the region $x > 0$ was allowed to vary from $10\,\mu$M to $110\,\mu$M. These results should be compared with the measured coverage after 30 min for an initial citrate concentration of 1 M and $50\,\mu$M in the lower concentrated buffer and the upper dilute suspension respectively, which corresponds to the data points marked by asterisks.

take into account that the system contains a relatively complex mixture of different ions, which are interconverted via multiple equilibrium reactions. As is further explained in section (4.5.2), the situation is further complicated by the fact that the molecular transport is affected by the electrostatic interactions between the charged species. If the effects of such phenomena are taken into account, it is no longer possible to solve the problem analytically, however, and therefore numerical methods would have to be implemented. In other words, it might, initially, seem advantageous to make use of the COMSOL Multiphysics® software. As is further explained in section 4.5.2, there, specifically, exists several different modules, which are supposedly especially well suited for simulating systems of the type considered here. The implementation, unfortunately, proved to be more difficult than had been anticipated due a number of complicating factors, which are discussed in section 4.4.2.

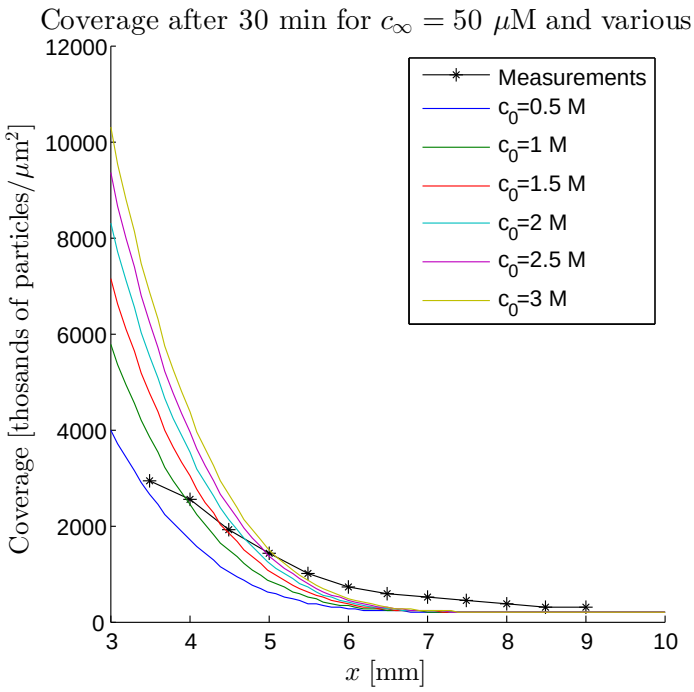

Figure 4.5: Diagram that shows the nanopartcle coverage predicted by the mathematical model of the one-dimensional diffusion problem described in section (2.2.2). Specifically, the graphs have been obtained by plotting the solution (2.2.2.16), as a function of the distance x from the bottom of the substrate, 30 min after the concentrated buffer solution was introduced into the system. When evaluating this expression it has, furthermore, been assumed that $c_{\mathrm{Ci}}(x,0) = c_0 = 1\,\mathrm{M}$ in the region $x > 0$, while the initial buffer concentration, for $x < 0$, was allowed to take on a range of different values, in the interval $0.5\,\mathrm{M} \leq c_0 \leq 3.0\,\mathrm{M}$. The asterisks, meanwhile, correspond to the measured coverage after 30 min given that the citrate concentration initially equalled 1 M and 50 μM in the lower concentrated buffer and the upper dilute suspension respectively.

4.2 Measured and simulated radially symmetric gradients.

Due to the relative success of the attempts to model the one-dimensional diffusion process, the natural continuation of this study was to consider a more complex geometry. As was explained in section 1, the aim was, specifically, to develop an experimental setup, with which a radially symmetric nanoparticle gradient could be deposited on a flat substrate. From a modelling point of view, this problem is, thus, effectively two-dimensional in nature. The relative complexity of the geometries that were considered as part of this design process, which is detailed in section 3.1.2, means that it not possible

to solve these problems analytically. Instead, COMSOL Multiphysics® was used to simulate the diffusion within these systems and was repeatedly implemented during the development process. In particular, these numerical calculations made it possible to continuously assess how specific changes to the setup would affect the outcome of the deposition process. In this subsection, the results of these computations will be presented along with the conclusions that can be drawn from them as well as how they affected the choices made during the design process. Note, however, that this discussion, which is found in the first subsection, will not be as detailed as the one in section 3.1.2. In fact, the second part of this section is exclusively devoted to the predicted and measured coverage profiles that are related to the is final experimental setup, which is schematically depicted in figure 3.5. Finally, it shall be noted that for the calculations, presented below, are based on the assumption that $D_{\mathrm{Ci}} = 0.623 \cdot 10^{-5}\,\mathrm{cm}^2/\mathrm{s}$, which, according to the "CRC Handbook of Chemistry and Physics", is the diffusion coefficient for citrate ions in a pure and dilute aqueous solution [30].

Simulations Performed During the Design Process.

While no efforts were made to simulate the original design, which is schematically depicted in figure 3.3, the is not true for the second geometry, found in part (a) of figure 3.4. Rather, a computer model for this system was defined and simulated with help of the COMSOL Multiphysics® software. Since the primary aim with these calculations was to assess whether the specific geometry was suitable for achieving radially symmetric nanoparticle gradients, it was imperative that the design parameters were chosen within reasonable limits. Due to the fact that changing the initial citrate concentration, in the Au NP suspension, had little effect on the final gradient, as the results presented in section 4.1 showed, c_∞ was set equal to the $50\,\mu$M. The supervisor, moreover, maintained that the concentration of the buffer solution should not exceed 3 M. This is, more precisely, due to the fact that a, too, high ionic strength adversely affect the stability of the suspension, as is mentioned in section 4.1. He, furthermore, advised against letting adsorption process proceed for more than three hours, for the sake of avoiding disturbances related to the aggregates that will, inevitably, form.

When designing the experimental setup for achieving radially symmetric nanoparticle gradients, one more process parameter have to be consider compared to the one-dimensional case. Specifically, the distance, Δz, between the liquid-liquid interface and the gold surface. Due to the strong distance

dependence of the coverage, which is implied by both the predicted and measured coverage profiles displayed in figure 4.2. Still, for the geometries that are currently being considered, this parameter can not be regarded as being tunable. In fact, the position of the substrate will be decided solely by the relation between its size and the radius of the funnel.

As was already mentioned in section 3.1.2, the second version of the experimental setup, depicted in figure 3.4 (a), was never realised since it was proven inadequate by the computer simulations. This is apparent from figure 4.6, which displays the predicted coverage as a function of the radial distance r for $2\,\text{days} \leq t \leq 12\,\text{days}$, $c_0 \leq 3\,\text{M}$ and $c_\infty \leq 3\,\text{M}$ under the assumption that the substrate is placed at the bottom of the funnel. Specifically, the diagram shows that distance from gold surface to the interface between the concentrated buffer and the suspension, $\Delta z \approx 80.4\,\text{mm}$, is to large for a high enough particle coverage to be obtained within a reasonable time frame. According to the supervisor for this project, the patterned substrates are, in fact, only of practical use if the coverage profiles are of the same order of magnitude as in the one-dimensional case. Given the experimental data presented in figure 4.2, it can, thus, be concluded that only setups, for which the coverage is on the order of $1000\,\text{particles}/\mu\text{m}^2$, can be regarded as potential candidates. Clearly, this demand is not satisfied by the design that is currently being considered. Because the available substrates were, moreover, smaller than the diameter of the funnel, at its narrowest point, this component was not included in the next version of the setup.

Due to geometrical constraints, the separation between the concentrated buffer source and the substrate could not be chosen arbitrarily, even in the absence of the funnel. Instead, the latter was assumed to be positioned just above the opening that leads to the stop cock, so that $\Delta z \approx 10.4\,\text{mm}$. The corresponding COMSOL simulations, meanwhile, resulted in two data sets, $(r,\theta(r))$, which are plotted in figures 4.7 (a) and (b). The latter, in particular, shows the predicted coverage after 3 h for a range of different buffer concentrations, while the former displays the same type of profile after different time periods, given that $c_0 = 3\,\text{M}$. Based on the earlier discussion, both these diagrams seem to suggest that the best experimental results should be obtained by using the limiting values on these two parameters.

Before ordering the specific parts, from the experimental setup could be assembled, it was deemed necessary to perform one final set of simulations, of the diffusion process. Specifically, these were performed for a range of different values on Δz, while c_∞, c_0 and t were kept constant and equal to 50 mM, 3 M and 3 h respectively. The specific aim of these calculations was

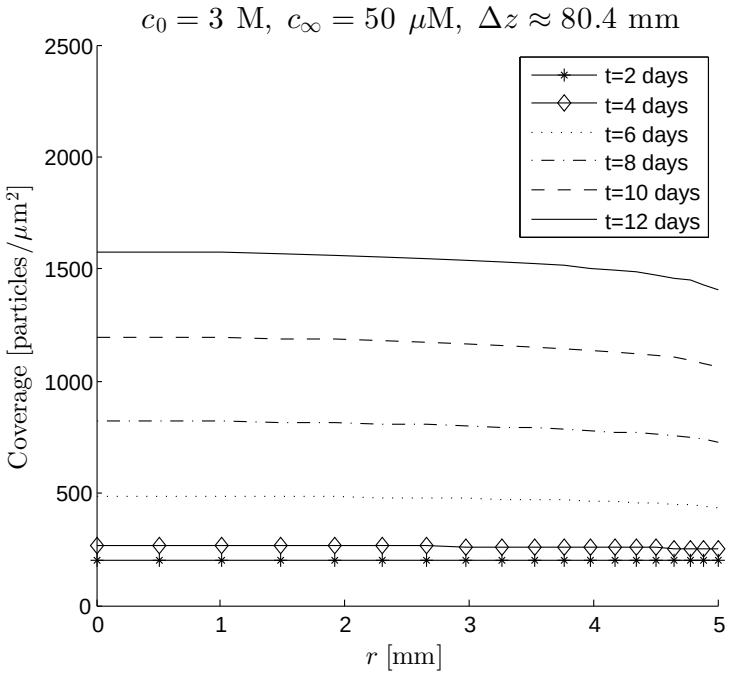

Figure 4.6: Diagram that shows the nanopartcle coverage predicted by the COMSOL Multiphysics® model of the radially symmetric diffusion problem that represents the experimental setup depicted in figure 3.4. This solution, specifically, applies to the case when a substrate was placed at bottom of the funnel, at a distance $\sim 80.4\,\text{mm}$ from the interface between the suspension and the concentrated buffer. Additionally, the initial citrate concentration was assumed to equal $50\,\mu\text{M}$ and $3\,\text{M}$ in the former and latter solution, respectively. Each of the graph, moreover, corresponds to a different time in the interval $2\,\text{days} \leq t \leq 12\,\text{days}$.

to assess if it would be practical to tune the coverage profile, and thereby optimize the final result, by changing the location of the gold surface. As the corresponding graphs, which are found in figure 4.8, reveals, this should indeed be possible, provided that a suitable method for positioning the substrate could be developed. It shall, furthermore, be noted that this diagram, in agreement with figure 4.2, indicate that the coverage varies very strongly with the separation. It should, therefore, be highly desirable to choose a design , for which this parameter can be changed with relative ease and good accuracy. As the discussion in section 4.4 will reveal, however, developing such a setup is not unproblematic.

As was indicated by the presentation in section 3.1.2, the designs described so far do not correspond to the final versions, which are schematically depicted in figure 3.5. Moreover, all of the nanoparticle covered substrates studied in this project were, in fact, prepared with help of either of these two setups.

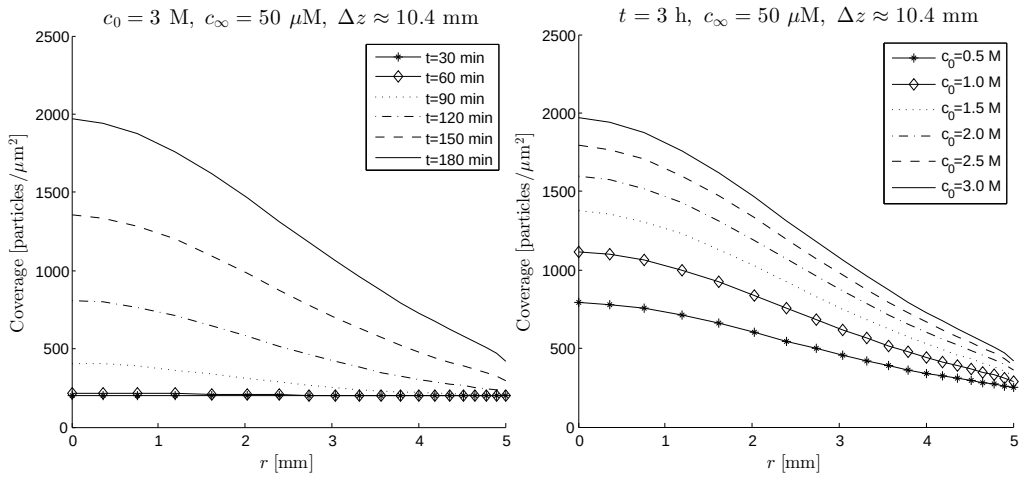

Figure 4.7: Diagram that shows the nanopartcle coverage predicted by the COMSOL Multiphysics® model of the radially symmetric diffusion problem that represents the experimental setup depicted in figure 3.4. Specifically, the graphs in part (a) and (b) have been obtained by plotting the solution as a function of the radial distance r. It has, moreover, been assumed, in both cases, that the interface-to-substrate distance equalled $\sim 10.4\,\mathrm{mm}$ and the initial citrate concentration in the nanoparticle suspension was $50\,\mu\mathrm{M}$. Furthermore, each of the curves in (a) depicts the coverage profile different times $0\,\mathrm{h} \leq t \leq 3\,\mathrm{h}$, provided that $c_{\mathrm{Ci}}(r,z,0) = c_0 = 3\,\mathrm{M}$ in the concentrated buffer solution after the liquid-liquid interface between the concentrated buffer and the Au NP suspension was formed. Diagram (b), however, has been obtained by plotting the predicted coverage for various values on the latter parameter, in the interval $0.5\,\mathrm{M} \leq c_0 \leq 3\,\mathrm{M}$, after $t = 3\,\mathrm{h}$.

Yet, prior to the fabrication, a set of simulations were performed in order to decide how long the adsorption process should be allowed to continue, given the distance between the substrate and the interface. The diagrams in figure 4.9, specifically, show the predicted coverage for various values on Δz and t provided that $c_0 = 3\,\mathrm{M}$ and $c_\infty = 50\,\mu\mathrm{M}$. If these diagrams are compared with the one-dimensional profile depicted in figure 4.2, it can be concluded that a reasonable coverage should result if the tube is positioned 3 mm from the gold surface and the deposition is interrupted after 15 minutes. In figure 4.10 comparable results are presented for an alternative version of the design, for which the hole was wider, 2 mm, and the interface-to-substrate distance larger, 7.5 mm. As should be expected, a longer time period, namely 60 min, would be required in order for a comparable number of particles to be adsorbed per unit area.

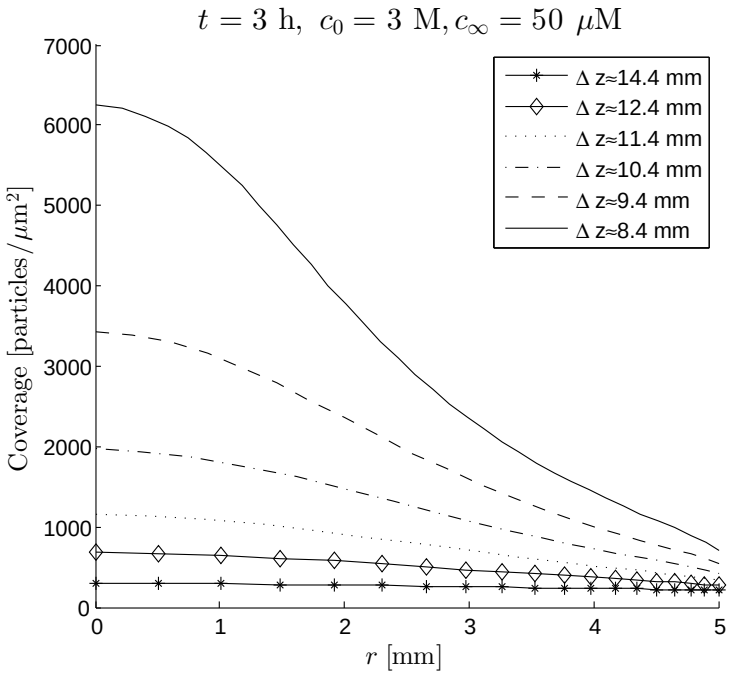

Figure 4.8: Diagram that shows the nanoparticles per square micrometer as a function of the radial distance r, predicted by the COMSOL Multiphysics® model of the radially symmetric experimental setup sketched in figure 3.4. The different curves, specifically, depicts the coverage profile after $t = 3\,\mathrm{h}$, given that the substrate was placed at various distances $8.4\,\mathrm{mm} \lesssim \Delta z \lesssim 14.4\,\mathrm{mm}$ from the interface between the suspension and the concentrated buffer. Additionally, the initial citrate concentration was assumed to equal $50\,\mu\mathrm{M}$ and $3\,\mathrm{M}$ in the former and latter solution, respectively.

Results Related to the Final Experimental Setup.

Before any measurements could be performed, a number of Au NP covered substrates had to prepared, by following the procedure described at the end of section 3.1.2. This process, specifically, yielded two suitable samples. The experimental conditions were, moreover, chosen based on the calculations described earlier. In particular, the two fabrication processes, which correspond to the setups depicted in part (a) and (b) of figure 3.5, were based on the parameter sets

$$\{t = 15\,\mathrm{min},\, c_0 = 3\,\mathrm{M},\, c_\infty = 50\,\mu\mathrm{M},\, a_{\mathrm{tube}} = 1\,\mathrm{mm},\, \Delta z = 3\,\mathrm{mm}\}\,, \quad (4.2.0.1)$$

and

$$\{t = 60\,\mathrm{min},\, c_0 = 3\,\mathrm{M},\, c_\infty = 50\,\mu\mathrm{M},\, a_{\mathrm{tube}} = 2\,\mathrm{mm},\, \Delta z = 7.5\,\mathrm{mm}\}\,, \quad (4.2.0.2)$$

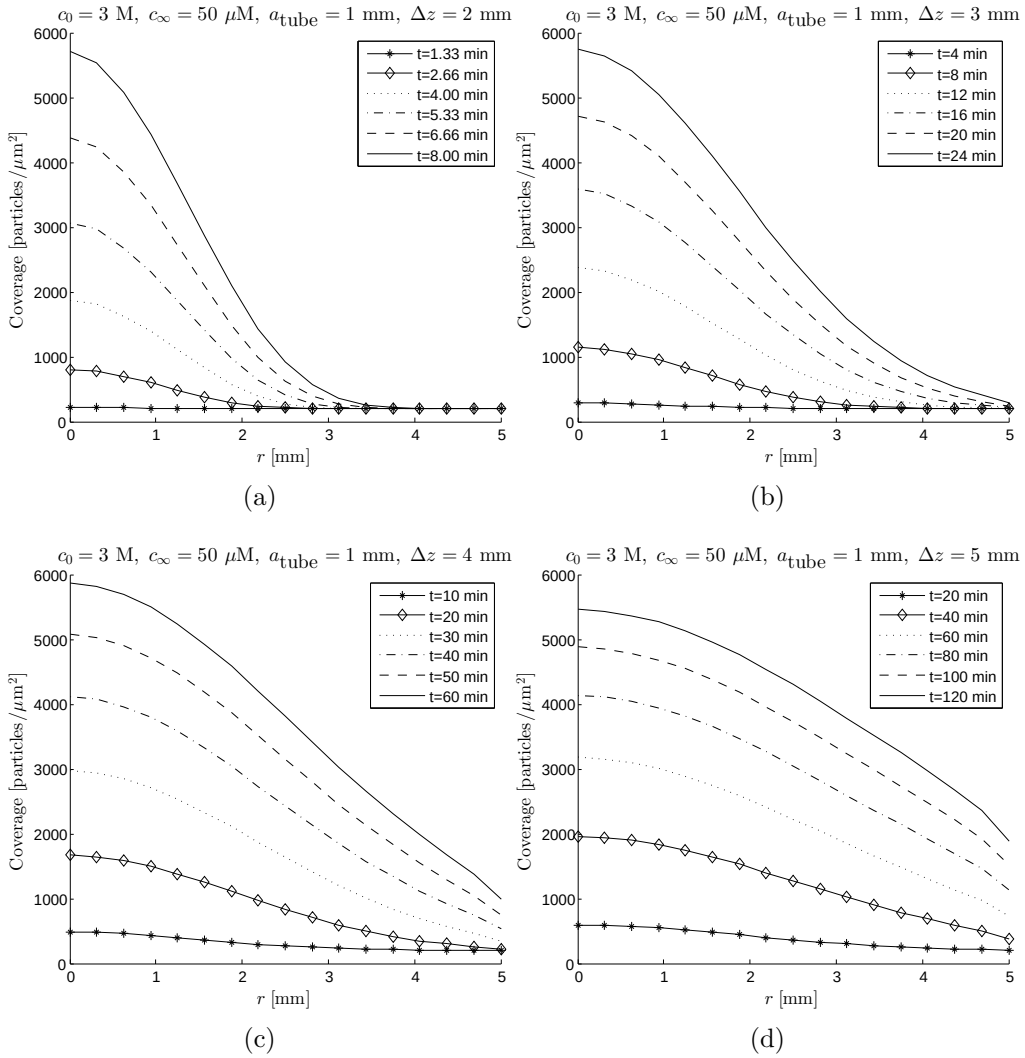

Figure 4.9: Diagram that shows the nanoparticles per square micrometer as a function of the radial distance r, predicted by the COMSOL Multiphysics® model of the radially symmetric experimental setup sketched in figure 3.5 (a). The different diagrams, specifically, shows the coverage profile after various times t, given that the substrate was placed at a distance of, (a), 2 mm, (b), 3 mm, (c), 4 mm and, (d), 5 mm from the interface between the suspension and the concentrated buffer. Additionally, the initial citrate concentration was assumed to equal 50 μM and 3 M in the former and latter solution, respectively.

respectively. Additionally, the gold surfaces were covered by a monolayer of dithiols in the former case and a cysteamine SAM in the latter. The same holds true for the pair of references, which were, concomitantly, fabricated by immersing a gold covered piece of silicon in 10 mM citrate buffers, in which certain amounts of Au NPs had been suspended.

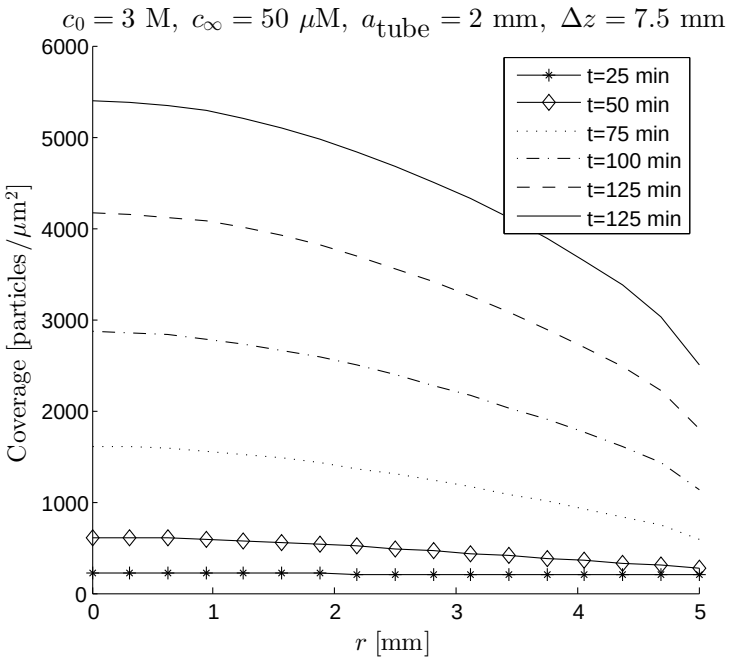

Figure 4.10: Diagram that shows the nanoparticles per square micrometer as a function of the radial distance r, predicted by the COMSOL Multiphysics® model of the radially symmetric experimental setup sketched in figure 3.5 (b). The different curves, specifically, depicts the coverage profile after various times $25\,\text{min} \leq t \leq 150\,\text{min}$, given that the substrate was placed at distance of 7.5 mm from the interface between the suspension and the concentrated buffer. Additionally, the initial citrate concentration was assumed to equal $50\,\mu$M and 3 M in the former and latter solution, respectively.

Once prepared, all of the samples were studied with help of a scanning electron microscope, as was discussed in section 3.2. Since the references ought to be uniformly covered by nanoparticles, it was deemed sufficient to image them at a single location only. The photograph, shown in figure 3.7, in particular, depicts a reference surface that had, previously, been functionalised with cysteamine molecules. As can be seen from this figure, the Au NPs seem to have been deposited fairly evenly on the substrate and seldom as part of larger aggregates. Consequently, the interparticle distances should be a relatively narrowly distributed, around some average value. What is more, these images suggest that the same holds true for the sizes of the individual colloids.

With help of the ImageJ® software, it is possible to determine the particle coverage from photographs of the patterned surfaces. For the case of the references, both of the alternative methods described in section 3.2.1, were, in fact, implemented for this purpose. The result of this analysis is sum-

marised in table(4.2.0.3). Though the exact value on θ_p is not particularly important, for these samples at least, it is worth noting that the two distinctive approaches, for calculating the number of particles, yield very similar results. For this reason, only the more straightforward of the two, which involved converting the photo into an black and white image and then counting the number of dark spots, was used to analyse the other samples. It can, moreover, be interesting to compare these measurements with coverage predicted by the RSA model. In section 3.2.2, it was, specifically, shown that the dimensionless number $\theta_p^{\text{jam}} = 0.547$, which gives the maximum percentage of the surface that can be covered by hard sphere particles, corresponds to a particle coverage of $\underline{N}_p^{\text{jam}} \approx 6964.620\,\text{particles}/\mu\text{m}^2$. According to the same section, the effect of the double layer interaction can be taken into account with help of the approximate relation, 3.2.2.1, between the coverage $\underline{N}_p$ and the citrate concentration c_{Ci}. Since $c_{\text{Ci}} = 10\,\text{mM} = 10^{-2}\,\text{M}$ during the preparation of the references, the maximal coverage should, based on this expression, be given by

$$\begin{aligned} \{(3.2.2.1)\} &\Rightarrow \underline{N}_p^{\text{ref}} \approx 37815 \cdot c_{\text{Ci}}^{0.5291} \\ \left\{c_{\text{Ci}} = 10^{-2}\,\text{M}\right\} &\Rightarrow \underline{N}_p \approx 37815 \cdot (10^{-2})^{0.5291} \\ &\Rightarrow \underline{N}_p^{\text{ref}} \approx 3307.23\,\text{particles}/\mu\text{m}^2 \end{aligned}$$

If the ImageJ® is used to estimate particle coverage from the SEM image in figure 3.7, with help of the methods described in section 3.2.1, the results are

$$\underline{N}_p^{\text{ref}} \approx \begin{cases} 1306.06\,\text{particles}/\mu\text{m}^2, & \text{with } \texttt{Analyze Particles} \\ 1466.81\,\text{particles}/\mu\text{m}^2, & \text{with } \texttt{Find Maxima} \end{cases} \tag{4.2.0.3}$$

In order to assess the effectiveness of the final version of the experimental procedure, the substrates, thus prepared, had to be studied more carefully than the references. It was, hence, deemed appropriate to image each of the surfaces at several different positions. These points were, more precisely, chosen so that they trace out a pair of straight lines, which joined the midpoints of the opposite sides of the, rectangular, substrates. The cysteamine functionalised substrate, schematically depicted in diagram 4.11 (a), was photographed, roughly, along the straight lines L_{1234} and L_{2341}, which join the opposite sides of the substrates. For the surface covered with a dithiol SAM, images were only recorded along a line parallel to the former, as can be seen from part (b) of the same figure. Given the coordinates for the corners of the substrates, which, as can be seen from figure 4.11, have been labelled from 1 to 4, it was possible to determine the exact locations that had been

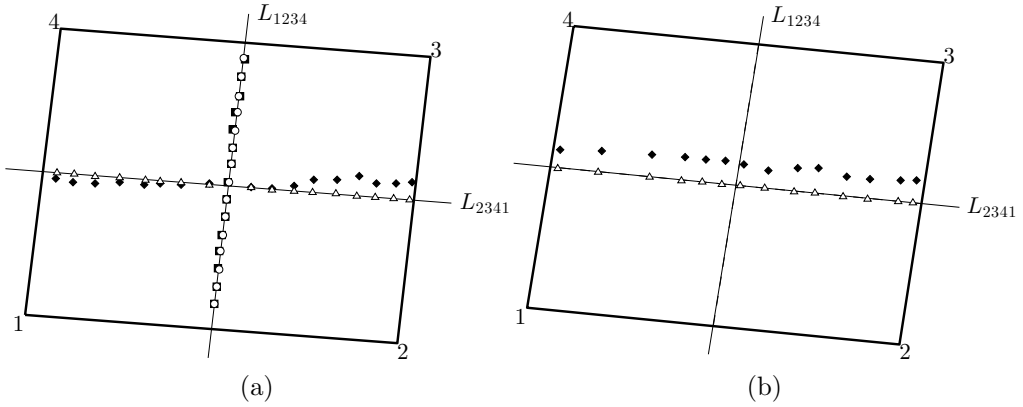

Figure 4.11: Diagrams showing the positions on the, (a), cysteamine and, (b), dithiol covered surfaces that were imaged with an SEM. Specifically, the locations that lie close to the lines L_{1234} and L_{2341} correspond to the solid squares and diamonds, respectively. The projections of these points, meanwhile, have been marked with to circles, in the former case, and triangles, in the latter.

photographed. Specifically, the points distributed along the lengths of L_{1234} and L_{2341} have been marked with solid squares and diamonds, respectively.

In order to be able to draw conclusions about the agreement between the predictions and the experimental data, the measured coverage, at each point, had to be associated with a specific distance. Moreover, this separation had to be comparable with the radial coordinate associated with the calculated value on $\underline{N}_p$. For this reason, the projections of the positions of the images on the lines L_{1234} and L_{2341} were determined. Specifically, these are represented by the white-filled circles and triangles in figure 4.11, respectively. Thereafter, the measured NP coverage, $\underline{N}_p^{\text{meas}}$, was plotted as a function of the distance d_I^{proj} between these projections and the midpoint. The reason for this procedure is that the experimental setups are radially symmetric, which means that the nanoparticle gradients should not only have a similar symmetry but also be centred around the middle of the substrates. The corresponding graphs can be found in the two diagrams in figure 4.12, together with the results of the COMSOL Multiphyisics® simulations. In particular, the curves shown in diagrams (a) and (b) represent the coverage profiles on the cysteamine and dithiol coated substrates respectively.

The most immediate conclusion that can be drawn from the figures 4.12 (a) and 4.12 (b) is that the predictions and the measurements differ quite substantially. Even so, the discrepancy is less significant in the former of

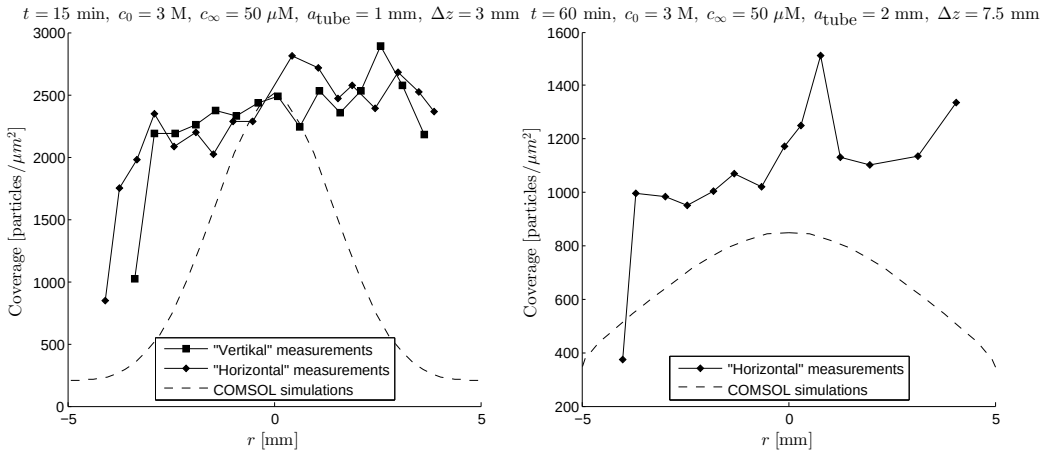

Figure 4.12: Diagram showing the nanoparticles per square micrometer as a function of the radial distance r. Specifically, the dashed curves, in parts (a) and (b), depicts the profiles predicted by the COMSOL Multiphysics® models of the radially symmetric experimental setups sketched in the figures 3.5 (a) and 3.5 (b), respectively. Comparable experimental data, in the form of ImageJ® estimates of the particle coverage within the imaged areas of the sample surfaces, have also been included. In particular, the solid squares and diamonds correspond to measurements at the locations, marked with the same symbols, displayed in figure 4.11. Note that each such point can, explicitly, be written as $(d_I^{\text{proj}}, \underline{N}_p^{\text{meas}})$. Here, d_I^{proj} is the distance between the projection of the position of the image and the midpoint on the substrate, while $\underline{N}_p^{\text{meas}}$ is the coverage estimated from that photograph.

the two cases. Though this may be a matter of coincidence, it can also be due to the fact that the two samples were covered by different types of SAMs. In particular, these were some issues related to the functionalisation of these surfaces, which might have affected the outcome of the experiments. These problems will be further discussed in section 4.4.3, together with other challenges associated with the preparation and measurement procedures.

In spite of the inconsistencies mentioned above, the measured coverage does seems to indicate that some kind of radial particle distribution has developed on the substrates. It is especially encouraging that the nanoparticles have, most prominently, been adsorbed close to the middle of the substrate. Still, the maximum appears to be shifted from the exact centre. Concomitantly, a number of different sources for the relatively large fluctuations, in the measured number of particles per square micrometer, can be identified. One possible explanation could be the inexact nature of the image analysis. Specifically, it is generally true that the best estimate of the coverage is obtained by counting all the particles by hand rather than, as in this project,

relying on approximate schemes, such as the one detailed in section 3.2.1. There are reasons to believe that the resulting error was relatively small in this case. As the results in (4.2.0.3), for instance, show, the more intricate analysis technique, described in the same section, yielded almost the same result as the less involved method, when applied to the image of the reference sample depicted in figure 3.7.

The non-uniform nature of the nanoparticle coating, could also have influenced the measurements. Once again, the most probable cause is that the quality of the SAMs, covering the gold surfaces, was not of sufficiently high quality. As was mentioned earlier, this issue will be addressed in section 4.4.3. A third type of effect that might, at least partially, explain the lack of agreement between the computer simulations and the experimentally obtained data is the occurrence of additional transport mechanisms, which may have influenced the diffusion process. Examples of such phenomena, which have not been included in the current theoretical model, shall be discussed in the sections 4.4.1 and 4.5. Concomitantly, suggestions will be given with regards to how these aspects can be taken into account.

4.3 General Conclusions

Based on the results presented in the sections 4.1 and 4.2, compared with the goals outlined in section 1, it is clear that the main aims of this project has been achieved. To be specific, the diagram in figure 4.2 indicates that the mathematical models of the one-dimensional molecular diffusion problem, indeed, capture the basic features of the physical situation, described in section 3.1.1. It should, therefore, be correct to assume that the main driving force for the transport of the citrate is the difference in concentration between the concentrated and dilute phases. The same result, furthermore, suggests that the net motion of these ions is not significantly affected either by the presence of the other electrolytes, which are also diffusing, or the equilibrium reactions that these participate in. It, thus, appears as if the diffusion coefficient for this species, found in literature, to some extent take the presence of these complicating factors into account. In other words, the approximation $D_{\mathrm{Ci}} \approx 6.904 \cdot 10^{-5}\,\mathrm{cm}^2/\mathrm{s}$, which is strictly only applicable at infinite dilution, can be regarded as an effective value on this, material, parameter. Additionally, the relatively good agreement, between the calculations and the measurements, implies that the RSA model is sufficient for explaining the adsorption processes considered in this project. In particular, by using the DLVO theory to calculate an effective particle radius, relatively accurate predictions of the coverage that results from the deposition of, bare, gold nanoparticles on samples coated with cysteamine or dithiol SAMs, can be obtained.

As was explained in sections 3.1.2 and 4.2, the chosen physical model was successfully applied to develop an experimental setup, which was intended to be used for covering the gold coated face of a single silicon substrates with a radially symmetric Au NP gradient. In accordance with the original plan, the COMSOL Multiphysics® proved to be an important tool for deciding the dimensions of the geometry. These computer simulations, more precisely, allowed the design parameters to be chosen, so that a significant coverage would be obtained within a convenient time frame without having to use an unreasonably high buffer concentration. Yet, this part of the project took longer time to complete than had initially been expected, partially due to the various problems that were encountered, which are detailed in section 4.4.3. As a result, the experimental studies were delayed, which together with the issues involving the substrate fabrication meant that only a limited the number of experiments could be performed.

While the correspondence between the predicted and measured coverage was

far from perfect, as figure 4.12 clearly shows, it is also apparent, from the same diagrams, that the obtained coverage profiles have at least some radial dependence. This result is, in fact, sufficiently good to be regarded as a proof of concept. It should, in other words, be possible to obtain substrates coated with radially symmetric nanoparticle gradient using an experimental setup similar to the one sketched in figure 3.5. Still, many aspects of this study could have been improved, as the discussions in sections 4.4 and 4.5 show. Several of these issues should and can, however, be resolved by continuing the research initiated in this project.

4.4 Model-, Simulation- and Experiment-Related Challenges

In this section, the key challenges related to the mathematical modelling, the simulations and the experiments, that were encountered during the course of the project, will be discussed. For the sake of convenience, the issues specific to each of the distinctive parts of this study will be presented separately, namely in the subsections 4.4.1, 4.4.2 and 4.4.3 respectively. As will become apparent, the possible solutions to these problems, which have not been tested during this project, will only be briefly mentioned. In some cases, however, a more detailed description have been included in section 4.5, which specifically details how the present study could be improved or extended through future research.

4.4.1 Challenges during Model Development

The development of the mathematical models, which represent the physical situations studied in this project, was, in general, relatively straightforward. As was discussed in section 2.1, the diffusions of the citrate ions, which were treated as a single uncharged species, was assumed to be the only transport phenomena that had to be taken into account. Though this conjecture greatly simplifies the modelling process, to the extent that analytical solutions can be derived for the 1D case, it also limits the accuracy of the corresponding predictions. Indeed, this is apparent from the discrepancy between the computed and experimentally determined surface coverage, indicated by the figure 4.2. Even though it is relatively easy to distinguish possible causes for this lack of agreement, the continued discussion will reveals that it is more challenging to compensate for them.

From the very beginning, it shall be noted that the assumption that the entire transport process can be reduced to the diffusion of single molecular species is flawed, in several respects. Firstly, all of the ions that make up the electrolyte, namely H_3Ci, H_2Ci^-, HCi^{2-}, Ci^{3-} as well as H^+ and Na^+, will, in reality, simultaneously diffuse through the system. Since each of the ions will do so at different rated, determined by the corresponding diffusion coefficient, a charge separation should, theoretically, result. This will, in turn, give rise to electric fields, directed so as to restore the, electrically neutral, equilibrium state. Since any charged particle, under the influence of a finite potential gradient, will tend to migrate so as to minimise their free energy, the motions

of the distinctive ions will become coupled. In order to take such phenomena into account, one, usually, applies the so called Nernst-Plancks equations, which will be further discussed in section 4.5.2. Another type of phenomena, which may link the concentrations of the distinctive species in a buffer, are different chemical reactions. Specifically, all solutes, except for the sodium ions, are, in this case, being continuously interconverted through different protonation reactions. Even though this coupling mechanism, together with the one mentioned earlier, severely complicates the mathematical modelling, there exist ways to take them both into account, as the discussion in section 4.5.2 will reveal.

Even in the absence of a bulk flow, across the exterior boundaries, convective currents may still be present within the system. As was mentioned already in section 3.1.2, the density of, on one hand, the concentrated citrate buffer and, on the other, the nanoparticle suspension differ quite substantial. Due to the fact that such gradients represent some of the principle driving forces for bulk fluid motion, a net flow of liquid should, from a theoretical point of view, arise immediately after the two phases come into contact. As was discovered during the experiments, and further discussed in sections 3.1.2 and 4.4.3, it is therefore not practical to supply the concentrated citrate solution from above. Consequently, the buffer was supplied from underneath the, less dense, nanoparticle suspension in all but one of the experimental setups described in section 3.1.2.

Another possible source for convective currents is the drag force associated with the movements of individual gold nanoparticles. Provided the particle distribution remains relatively uniform this motion is of Brownian origin, no net effect on the molecular transport should be expected. In the systems at hand, however, there ought to be a tendency for the particles to sink into the, initially, pure buffer, not only due to gravity but also because of the substantial concentration difference. Moreover, the former driving force should become more significant as a result of aggregate formation. Since the coagulation is most severe close to the buffer-suspension interface, this could potentially gives rise to mixing effects that are likely to disturb the diffusion process. In other words, the spatial gradients could, partially, be evened out so that the resulting concentration profile may not be as sharp as the theory predicts. This is one of the reasons why the coverage measurements, for the surfaces patterned with one-dimensional particle gradients, begin a few millimetres above the bottom edge of the substrate, as figure 4.2 indicates. No measurements are required in order to prove the existence of this phenomena, however, since it can be directly observed during the preparation procedure. Specifically, its presence is indicated by the swirling blue and veil-like aggre-

gate rich regions that appear in close vicinity to the liquid-liquid interface, which are clearly visible in the photograph in figure 3.2.

The presence of the Au NPs is likely to affect all solute and solvent molecules in their immediate vicinity. The concentrations of the individual ions should, in particular, be highly non-uniform, at least locally, due to the formation of electrical double layers. Additionally, a range of different confinement effects may become important if the particle content is high enough that the average distance between them is reduced to molecular dimensions. Finding suitable models for the individual interactions, mentioned above, is not an easy task, however. What is more, these mechanisms are, for the case at hand, coupled to both the migration of the ions as well as the reactions that these species participate in. In addition to influencing the molecular transport, these, highly intertwined, phenomena should also affect both the interparticle and the particle-surface interactions. Another reason for doubting the accuracy of the predictions obtained by combining of the DLVO theory and the RSA model, is that these are based on several relatively crude approximations. Even so, no attempts have been made to account for the presence of the Au NPs, when simulating the diffusion processes, or to find a more accurate relation, than the interpolant (3.2.2.1), between the surface coverage and the citrate concentration.

4.4.2 Computational Challenges

Since several issues were encountered during the development of the theoretical models, it is, perhaps, not surprising that the implementation was somewhat problematic. First and foremost, learning how to use any computer software, in this case COMSOL Multiphysics®, is very seldom a straightforward process. One of the disadvantages, compared to writing a specific program for solving a specific problem, is that COMSOL, due to its wide range of applicability, is not as easy to overview. It is, for example, relatively difficulty to distinguish what mistakes have been made, if any, when a solution can not be found. Still, simple simulations can most often be performed without much effort, once one have been familiarised with graphical interface. This is especially true if the problem only involves one type of physics. Improving the accuracy of the calculations, by taking additional phenomena into account, is more difficult, however, in spite of the fact that the program has, supposedly, been developed for the purpose of tackling multi-physical problems. As was discovered during the course of the project, the distinctive interfaces are, in fact, not always fully compatible, and even if they are,

it may not be self-evident how to combine them. Difficulties were, specifically, encountered in the attempts account for the electrostatic interactions between the ions as well as the chemical reactions that these participate in. As was mentioned in section 4.4.1, the corresponding physical model will be discussed in more detail in section 4.5.2.

As will become evident from the presentation in section 4.5.2 it might, in hindsight, have been more prudent to design a specific computer program for simulating the physical processes instead of relying upon the COMSOL Multiphysics® software. If the program code had, for instance, been written in an MATLAB® `.m`-file, the finite elemental method could have been implemented with help of certain predefined functions. Furthermore, the alternative solving procedure, suggested by , which is also detailed in section 4.5.2, could more easily have been implemented. Because the above mentioned shortcomings, of the current version of COMSOL Multiphysics®, were discovered at a relatively late stage, there was not enough time available to realise these plans. Even so, developing a computer program, for the purpose solving problems with this level of intricacy, ought to be relatively time-consuming. This explains why it was deemed preferable to make use of a commercial software package.

4.4.3 Experimental Challenges

As the presentation of the setup development process in section 3.1.2 showed, several distinctive designs were tested before arriving at the final two versions, which are schematically depicted in figure 3.5. Unsurprisingly, the original setup, shown in figure 3.3, had to be redesigned, so as to be compatible with the available components. The later versions, meanwhile, were successively rejected following the discovery of one, or more, distinctive shortcomings of each design, as will be further discussed below. In order for the simulations of the diffusion process to be reliable, it is crucial that good enough estimates of suitable dimensions for the geometry are available. The scale must, in particular, be chosen so that a sufficiently high coverage can be achieved in spite of the limitations on the required time and buffer concentration. The dimensions of the relevant components were not readily available, however, neither from the homepage nor the product catalogue of the suppliers. Fortunately, the manufacturers were willing to provide this information, without any reservations.

Given the sizes of the individual parts, the diffusion process could be simulated within a geometry that represents the version of the experimental

setup shown in figure 3.4. As was already mentioned in sections 3.1.2 and 4.2, this lead to the discovery that the separation between the substrate and the liquid-liquid interface was to large. Specifically, the time period required for achieving a reasonable coverage, without using an extremely concentrated citrate buffer, was deemed to long for the deposition process to be reliable. This lead to the development of an alternative design, which only differed from the versions shown in figure 3.4 in that the funnel had been removed. Even though the calculations, presented in figure 4.6, showed that the long distance between the source and the target surface remained an issue, an order was placed for the required components. The long delivery time, which amounted to approximately 5 weeks, meant, however, that the first experiments could not be performed as scheduled.

Immediately after the experimental setup had been constructed, from the purchased glassware, a simple test was performed to make sure that all of the components, as well as the connections between them, functioned properly. This was, more precisely, achieved by first adding the concentrated buffer followed by the nanoparticle solution, but only once the valve had been sealed and the section above it had been rinsed clean. Next, stop cock was reopened so that a, relatively, sharp interface was formed between the two liquids. Unfortunately, it soon became apparent that the setup suffered from severe leakage problems, which had the added effect that the valve became locked in an open position. Though attempts were made to release the latter, it deemed necessary to come up with a new design.

In the type of setup considered next, a substrate was, as was explained in section 3.1.2, first placed in a small dish filled with an Au NP suspension. The deposition process was, thereafter, initiated by lowering a piece of tubing, which other end was attached to a syringe filled with concentrated buffer, into the liquid. The idea was, specifically, that the citrate would be diffuse into the underlying dilute region, which, as in the earlier cases, should result in the deposition of a radially symmetric particle gradient on the substrate. Still, it became evident, already from the first experiment, that the large difference in density between the two phase gave rise to such strong convective currents that the design was rendered inadequate. In particular, the much lighter gold nanoparticle suspension was relatively quickly transported up the tube once the liquid-liquid interface had formed. It was, thus, apparent that it would be entirely flawed to assume that the flow of the citrate buffer from the bottom end of the tube could be modelled as a diffusive phenomena. In other words, it seems very unlikely that a spherically symmetric concentration gradient, which is required in order to obtain the sought type of coverage profile, would form.

In the final versions of the experimental setup, which are depicted in figure 3.5, the lateral ordering of the phases was reversed compared to the previously considered case. The analysis of the substrates, thus prepared, revealed that the obtained coverage showed at least some degree of radial variation, as can be seen from figure 4.12. This can be seen as proof that this is indeed an appropriate concept for preparing gold coated surfaces covered by radially symmetric Au NP gradients. Even though the latest designs were far from perfect, it was not deemed necessary to develop them further. Still, a number of specific changes, which could possibly have improved the results, will be proposed as part of the discussion in section 4.5.1. Specifically, one of the most crucial parameters is the separation between the buffer source and the gold surface, mainly due to the strong distance dependence of the concentration gradient. In other words, developing a practical strategy for controlling this parameter is perhaps the most important design challenge that has yet to be overcome.

4.5 Future prospects

The main purpose of this section is to provide some proposals of how the research conducted as part of this project could be continued so as to either extend the range or improve the accuracy of the results presented in this report. For the sake of clarity this discussion will be divided into three distinctive parts. Firstly, some general remarks will be made with regards to how the modelling, computer simulations, experimental setups as well as the data gathering and analysis could be further developed in future studies. This will be followed by a more detailed discussion on how the Nernst-Planck equations can be used to better the mathematical model of the physical situations considered in this project. In the final subsection, the possibilities to extend the study to true three-dimensional problems shall be presented. This discussion will specifically focus on the prospects for depositing gold nanoparticles inside gels, with regards to both the modelling of the problem as well as practical aspects such as what material parameters should be considered when choosing a suitable polymer.

4.5.1 General Remarks.

As with any project, it is always possible to, with the benefit of hindsight, distinguish choices that would have been made differently if the outcome had been known in advance. In what follows, some remarks of this sort will be made, with the hope of providing some guidelines on how to avoid some of the challenges that were encountered as part of this project. In addition, some suggestions will be made on in what ways future research can build on the results that were presented in this report. It shall also be noted that a more detailed discussion on how the so called Nernst-Planck equations can be implemented with help of the COMSOL Multiphysics® software in order to yield more accurate results can be found in the next subsection. Thus only a few general comments will be made with regards to how the mathematical models as well as the simulations could have been improved.

Beginning with the mathematical modelling, it is essential to stress that the model used to represent the physics related both to the transport of ions within the buffer as well as the deposition of the particles are both relatively rudimentary as can be gathered from the discussions in the first two chapters of this report. The natural way to improve these predictions is, as was explained in some detail in section 4.4.1, to take more of the physics into account. Yet, doing so generally has the disadvantage that it complicates

the physical models, which in turn makes the numerical simulations more involved and concomitantly less reliable. Another disadvantage is that any such efforts are almost always associated with the introduction of additional parameters. This furthermore leaves more room for uncertainties, since it is not always clear how these values shall be chosen in order to best reflect the physical situation. Without proper estimates of these input arguments, there is little point in taking more complex physics into account. At the same time, it should be clear that while relatively much effort has been put into researching how the molecular transport could be better represented, hardly any efforts have been made to inquire if and how it would be possible improve the model for the adsorption process. Specifically, the equation (3.2.2.1) has exclusevily been used to correlate the predicted citrate concentration with a particular surface coverage. As was explained in section 3.2.2, this power law was obtained by interpolating the predictions of the set of equations in (3.2.2.2), which in turn were obtained by combining the DLVO theory with the RSA model. It should be evident from the presentations of the latter, which are found in the sections 2.3.1 and 2.3.2 respectively, that these only take the most basic physical phenomena related to the interparticle interactions and the adsorption process into account. Hence, there exist much room for improvements. Better predictions should, for instance, be achieved if surface forces other than the van der Waals and electrostatic double-layer interactions were considered and if the adsorbing particles were allowed to move laterally across the surface. While there exists alternative approaches that include the effects of such, additional, mechanisms it was deemed appropriate to apply the same method as Lundgren in this study. Additionally, the parameter values that were used in the calculations presented in this project are the same as those suggested by the author in his PhD thesis [5]. In this context it is especially worthwhile to mention the surface potential ψ and the dimensionless constant λ. In particular, it should be clear from the discussion in section 2.3.1 that $\psi = 50\,\mathrm{mV}$ and $\lambda = (e-1)/2$ are not the only possible choices, but rather represents estimates that according to Lundgren seems reasonable based on earlier research. It should be said, however, that the applicability of these values have, for the sake of convenience, not been scrutinised during the course of this study Thus, it is entirely possible that more accurate results could be obtained, in future studies, simply by using an alternative estimates, which better represent the physical situation.

With regards to the computer calculations it shall, firstly, be said that no great efforts were made to research how the numerical solving routines could have been changed in order to improve the predictions. In particular, it should be evident from the presentation in section 3.2.3 that the default set-

tings were almost exclusively left unaltered during the computations, while the more advanced options were never even considered. Still, due to the fact that each of the physical interfaces have been specifically developed for solving certain types of problems, it should generally not be necessary to alter the predefined input arguments. This should be especially true for those parameters that are only related to the numerical solving routine. Another aspect of the numerical calculations that has not been thoroughly researched, is the possibility that there may exist alternative physical interfaces that could be used to simulate the transport problems of interest for this study. In fact, only the basic tools that the COMSOL Multiphysics® software provides, have so far been considered. Had the project been prolonged, it would perhaps have been a good idea to overview the programs more advanced features and to make some further inquiries into what physical models, other than "Transport of Diluted Species", that are available. Moreover, it is important to at least mention that COMSOL Multiphysics® is not the only commercial software for solving the type of problem considered as part of this project. For future research it might be advantageous to explore what other programs are available and if any of them are even more suitable for simulating the physical situations at hand.

As is suggested by the sketch in figure 3.5, together with the discussion in section 4.4.3, the final version for the experimental setup must be considered to be rudimentary, at best. In other words, there exists much room for improvements. Even so, the relative success of the obtained results, which were presented in section 4.2, suggest that the fundamentals of this concept are sound. A complete overhaul of the most recent design should therefore not be necessary. In what follows, a few general guidelines of how the setup could be changed in order to further improve the quality of the results will be presented. As was already mentioned in section 4.2, the strong distance dependence of the coverage means that it is crucial to be able to control the separation between the surface and the concentrated buffer solution. This means that it not only important to be able to fixate both the position and the inclination of the substrate relatively precisely but also to have a sharp liquid-liquid interface. These represent perhaps the two areas where the most significant improvements can be made, since the design concept offered very little control over these parameters. One possible way to achieve the latter goal is to separate the two phases by a semi-permeable membrane, since this would minimise the intermixing between them. While doing so would hinder the Au NPs from sinking into the concentrated buffer, which is advantageous, it would at the same time mean that the nanoparticles and the aggregates that they form will begin to pile up on top of the membrane.

For the case of a prolonged adsorption process it is therefore possible that the inflow of buffer will become hindered with time. With regards to the distance control there are exists, essentially, three distinctive concepts. In particular, either the position of the substrate, the liquid-liquid interface or both may be tunable. While there is no reason why the second variant should be superior, or inferior, to the other two, it was, for the sake of convenience, implemented in the final version of the experimental setup. Regardless, it is important to choose a design that allows one to firmly fixate both the solid surface and the boundary between the two solutions, but that still leaves the distance tunable. Finally, it should be said that it is also crucial to be able to interrupt the deposition process quickly without causing any unecessary mechanical motion. In particular, one must avoid, at all costs, that the substrate, even briefly, comes into contact with regions of high citrate concentration, since this could potentially ruin the adsorbed pattern. Letting both liquids pour out from below the substrate is perhaps the easiest and most effective way to achieve this, which explains why this methodology was implemented both in this project as well as the in the studies performed by Lundgren [5].

The final part of this discussion will concern to the data gathering and analysis, which were performed with an SEM and the ImageJ® software respectively, in accordance with the presentation in section 3.2. This pair of methods is only one example of possible approaches for determining the coverage on the Au NP patterned gold surfaces. Lundgren, for example, mentions that similar measurements can be obtained by imaging the substrates with a transmission, rather than scanning, electron microscope [5]. Another possibility is to use imaging surface plasmon resonance, iSPR, which, supposedly, allows the gradients to be directly visualised, since the SPR response is directly proportional to the particle density. As Lundgren, and colleges, mention in their, as of yet, unpublished article, this technique is especially useful in biological applications where the patterned substrates have been coated with biomolecules, such as proteins. The main reason for this is that the added layer alters the dielectric constant next to the surfaces of the adsorbed nanoparticles which in turn changes the resonance frequencies associated with the local surface plasmons. Moving on to the image analysis, there exists, as was mentioned in section 3.2.1, an alternative technique for determining the number of particles in each SEM photograph. It was initially believed that a better result would have been obtained with this method compared to the approached that was primarily used in this study, due to its relative simplicity. The comparison between the two techniques that was presented in section 3.2.1 revealed, however, that there was no significant difference between the estimated particle counts for the same image. Yet, one should

not forget to mention that the most accurate way to determine the number of particles is to count them by hand, wherefore any result obtained with computer controlled analysis methods will be inaccurate, at least to some degree. While there are likely to exist other, and more sophisticated approaches for obtaining comparable estimates, it seems unlikely that the counting of the particles is the most significant source of errors.

4.5.2 Implementing the Nernst-Planck Equations.

Within the COMSOL Multiphysics® environment there exist several, predefined, physical interfaces that are supposedly well suited to solve the type of problem considered in this project. One of these, which forms part of the "Chemical Engineering" module, is labelled "The Nernst-Plancks Equations". As the name suggests, this modelling environment is based on the Nernst-Planck equations, which purpose is to describe the transport of ions in liquid media. In the 4.3 version of the program, which has just been released, a "Nernst-Plancks Equations" interface has been added, as part of the new "Corrosion" module, that essentially describes the same kind of physical situation, but which is especially well suited for the simulating the ionic transport related to corrosion phenomena.

Within both these frameworks it is possible to take chemical reactions, of any type, into account through explicit inclusion of expression for the corresponding reaction rates. Yet, this is not a convenient approach for the case at hand, since both the protonation and deprotonation processes occur so fast that kinetic data is not readily accessible. A better choice would be to assume that these reactions occurs so rapidly, compared to the other transport phenomena, that the involved species are in local, chemical, equilibrium. For this purpose it initially seems suitable to use the "Reaction Engineering" interface, which is also defined within the framework of the "Chemical Engineering" module. The reason is that it provides a modelling environment that has been developed for the purpose of simulating coupled "irreversibel", "reversible" as well as "equilibrium" reactions. While it is always necessary to define all the chemical species involved, the rate constants only have to be specified for the two first mentioned types, while it suffices to state the equilibrium constants in the third case. Specifically, it is the acidity constants, which are almost equivalent to the latter parameter, that are known for each of the acid-base reactions involving the species of interest. Unfortunately, this interface has not been defined to take the spatial dependence of

the concentrations into account.[1] This issue can be resolved, however, with help of a specific so called "Synchronisation" node, which is available in the "Synchronisation" context menu. While the specific purpose of this feature is to introduce a spatial dependence into the model for the reactions that occurs within the system, this feature is not available if these are of the "equilibrium" type. Hence, this function does not help solve the problem at hand. More precisely, even if it would be possible to couple the "Reaction Engineering" and "Nernst-Planck Equations" interfaces, this would again require that a pair of, unknown, rate constants are defined for each of the "Reversible" reactions.

There exists another plausible way to resolve the said issue, that can in fact be implemented in COMSOL. This approach involves using either one of the environments for solving the Nernst-Plancks equations, but not necessarily together with the "Reaction Engineering" interface, with the rate constants set equal to sufficiently large values. In particular, these should be sufficiently high that the reactions, within the framework of this model, occurs on a much faster time scale than the diffusion and the migration. In this case, equilibrium will, for all practical purposes, be reached almost instantaneously. The first attempts to implement such a concept was unsuccessful, however, because the forward rate constants could not be set higher than, approximately, $10^4\,\mathrm{mol/dm^3 \cdot s}$ since doing so caused the simulations to fail. While this problem might have, at least partially, been avoided by defining the geometry as "1D", rather than a "2D" there is no guarantee that this would have allowed the rates to be chosen high enough that good predictions would have been obtained. One of the reasons why this approach was not pursued further was that the a predefined solution, of this very type, for a problem very similar to the one considered in this project was supposed to be included in the 4.3 versions of the COMSOL Multiphysics® software. Though the hope was that this model could have been altered in such a way that it would correspond to the system described in section 3.1.1, rather than the one considered in the original corrosion problem, this was not possible due to time shortages. Specifically, it should be said that a trial version of the named program was first released at a very late stage in the project, which explains why there was not sufficient time to pursue this plan.

Another approach to deal with a problem, similar to the one at hand, was originally suggested by Swietach et al [31]. Specifically, one of the systems

[1]Rather than providing the program with specific geometry, the user instead states which type of process, and vessel, that is being considered. This, specifically, includes "batch", "semi-batch", "plug-flow" and "" types of reactors. The total volume of the system is another of the input arguments, which together provides the, almost, the same information as a specific geometry, which is otherwise requested.

they considered in their study of the transport of H^+ ions inside cells, was composed of a solution that contained protons together with a pair of buffers. In the mechanistic model of this physical situation that was presented in the final article, all of the species were, moreover, "allowed to diffuse and react". Moreover, the authors state that"In FEM, the diffusion equation is solved in a stepwise fashion (time-step 1 ms), alternating with a minimisation function that returns solutes to equilibrium (to maintain buffers at equilibrium with protons after redistribution due to diffusion)". By using such a procedure it is inexplicitly assumed that the buffering effect is instantaneous, wherefore it is not necessary to know the rate constants for the associated reactions. One possible way of implementing this procedure is, as was mentioned in section 4.4.3, to write a dedicated MATLAB program, which sole purpose is to solve the corresponding initial and boundary value problem. Compared to using a more generic coding environment, such as Fortran, the named software package has the advantage that it provides predefined functions, with the help of which FEM can be implemented. Another approach would be to use a certain COMSOL Multiphysics® module, named Live-link with MATLAB, which allows the former program to be controlled using the MATLAB desktop. Specifically, it should be possible to first simulate the diffusion of all the buffer species, as well as the protons, with help of "Nernst-Plancks Equations" interface, for a sufficiently short time-period. In other words, COMSOL will solve the Nernst-Planck equation, with terms representing the reaction rates set equal to zero. Next, the equilibrium the concentrations of all these compounds are calculated, given the pH and the total citrate concentration at each point. These values are then used as the initial values, which are provided as input to the COMSOL Multiphysics® when simulating the redistribution that occurs during the next time step. As of yet, however, no efforts have been made to pursue either of these alternative methods. Since, very few inquires have been made with regards to if and how these procedures can implemented in practice, it is not certain that either of them are suitable for solving the problems at hand.

4.5.3 The Adsorption of Au NPs in Gels.

According to the original plan for this project, the aim was to apply the physical model, which was used to predict the coverage profiles resulting from one-dimensional and radially symmetric diffusion processes, to simulate the deposition of nanoparticles inside a gelatinous material. At an even earlier stage, it was suggested that the procedure should involve the synthesis of the gel system followed by the injection of first an Au NP suspension

and then a concentrated citrate buffer. After having studied the existing theoretical models for such systems it was decided that these ideas had to be abandoned, however. Specifically, it quickly became apparent that choosing a gel with the proper material characteristics is not only crucial but also far from straightforward. Another problem is that there seems to be no simple way of halting the diffusion of the concentrated buffer, once it has been introduced into the system. In other words, it is not clear how one can exert control over the deposition process.

Bibliography

[1] Lundgren A, et al. Self-Arrangement Among Charge-Stabilized Gold Nanoparticles on a Dithiothreitol Reactivated Octanedithiol Monolayer. Nano Letters. 2008;8(11):3989–3992.

[2] Willner I, Willner B. Biomolecule-Based Nanomaterials and Nanostructures. Nano Letters. 2010;10:3805–3815.

[3] Lundgren A, et al. Self-Assembled Arrays of Dendrimer-Gold-Nanoparticle Hybrids for Functional Cell Studies. Angewandte Chemie International Edition. 2011;50:3450–3453.

[4] Lundgren A, et al. Nanoparticle Gradients for Investigation of Cell-Surface Interactions. European Cells and Materials. 2011;21(1):22–22.

[5] Lundgren A. Self-Orginization of Nanoparticles: Implications for Interface Biology. Department of Chemistry and Molecular Biology, Interface Biophysics, University of Gothenburg; 2012.

[6] Cu Y, Saltzman M. Mathematical modeling of molecular diffusion through mucus. Advanced Drug Delivery Reviews. 2009;61:101–114.

[7] Cai L, Panyukov S, Rubinstein M. Mobility of Nonsticky Nanoparticles in Polymer Liquids. Macromolecules. 2011;44:7853–7863.

[8] Phillips R, Kondev J, Theriot J. Physical Biology of the Cell. Garland Science, Taylor & Francis Group, LLC; 2009.

[9] Hu X, Do DD, Zu Q. Effects of supporting and buffer electrolytes (NaCl, CH_3COOH and NH_4OH) on the diffusion of BSA in porous media. Chemical Engineering Science. 1992;47(1):151–164.

[10] Chemical Reaction Engineering Module User's Guide; 2012.

[11] van Soestbergen M, Biesheuvel PM, Rongen RTH, Ernst LJ, Zhang GQ. Modified Poisson-Nernst-Planck theory for ion transport in polymeric electrolytes. Journal of Electrostatics. 2008;66:567–573.

[12] Folland GB. Fourier analysis and its applications. Brooks/Cole Publishing Company; 1992.

[13] Råde L, Westergren B. Mathematics Handbook for Science and Engineering. Studentlitteratur; 2004.

[14] Higashitani K. Control of interactions between particles in liquids. In: Hosokawa M, Nogi K, Naito M, Yokoyama T, editors. Nanoparticle Technology Handbook. 2nd ed. Elsevier B.V; 2007. p. 139–146. `http://www.knovel.com.proxy.lib.chalmers.se/web/portal/browse/display?_EXT_KNOVEL_DISPLAY_bookid=4381` (accessed 15 June 2012).

[15] Guozhong C. Nanostructures and Nanomaterials: Synthesis, Properties and Applications. Imperial College Press; 2004.

[16] Adamczyk Z, et al. Irreversible adsorption of particles on heterogeneous surfaces. Advances in Colloid and Interface Science. 2005;118:25–42.

[17] Adamczyk Z, Warszyhski P. Role of electrostatic interactions in particle adsorption. Advances in Colloid and Interface Science. 1996;63:41–149.

[18] Semmler M, et al. Diffusional Deposition of Charged Latex Particles on Water-Solid Interfaces at Low Ionic Strength. Langmuir. 1998;14:5127–5132.

[19] Semmler M, Rička J, Borkovec M. Diffusional deposition of colloidal particles: electrostatic interaction and size polydispersity effects. Colloids and Surfaces A: Physicochemical and Engineering Aspects. 2000;165:79–93.

[20] Lundgren AO, et al. Tuning molecular compartmentalization via nanoparticle self assembly, implications for classical cell adhesion experiments;. In manuscript.

[21] Fisher Scientific: Laboratoriekatalogen 2011/12; 2011.

[22] Laboratory Glassware Catalogue; 2011.

[23] Petty MC. Molecular Electronics: From Principles to Practice. John Wiley & Sons, Ltd.; 2008.

[24] Zangwill A. Physics at surfaces. Cambridge University Press; 1988.

[25] Ohring M. Materials Science of Thin Films: Deposition and Structure. 2nd ed. Academic Press; 2002.

[26] Ferreira T, Rasband W. ImageJ User Guide. Bethesda, USA; 2012. `http://imagej.nih.gov/ij/docs/guide/user-guide.pdf`.

[27] COMSOL Multiphysics® User's Guide; 2012.

[28] COMSOL Multiphysics® Reference Guide; 2011.

[29] Yaws CL. Yaws' Handbook of Thermodynamic and Physical Properties of Chemical Compounds. Knovel; 2003.

[30] Vanýsek P. Ionic Conductivity and Diffusion at Infinite Dilution. In: CRC Handbook of Chemistry and Physics;. .

[31] Swietach P, et al. Modelling intracellular H^+ ion diffusion. Progress in Biophysics & Molecular Biology. 2003;83:69–100.

[32] Nordling C, Österman J. Physics Handbook for Science and Engineering. Studentlitteratur; 2006.

Appendix A

Nomenclature – Acronyms & Symbols

This chapter provides a summary of the key acronyms and symbols, which are used in the report. Though the former list, which is found in the first of the two sections, is complete the latter is not. Proper definitions of all combinations of indices and symbols, which represent specific physical variables or constants, can be found in the relevant part of the text, however.

A.1 List of Acronyms

Common acronyms

DLVO	Derjaguin, Landau, Vervwey and Overbeek
FEM	finite element method
iSPR	imaging surface plasmon resonance
NP	nanoparticle
NPBC	Nano Particle Binary Chemistry
ODE	ordinary differential equation
PDE	partial differential equation
RSA	random sequential adsorption
SAM	self-assembled monolayer
SEM	scanning electron microscope
SPR	surface plasmon resonance

A.2 List of Symbols

Latin symbols

A	area
a	radius
C	general constant
c	concentration
D	diffusion constant
d	surface-to-surface separation, separation
f	general function
I	ionic strength
$\boldsymbol{J}$	flux
l	length
N	total number
Q	charge
$\boldsymbol{r}$	coordinate vector
R	reaction rate
r	center-to-center distance, radial coordinate
T	temperature
t	time
u	interaction potential
V	electric potential
$\boldsymbol{v}$	velocity
x	general coordinate, x-coordinate
Z	valency
z	vertical distance, z-coordinate

Greek symbols

Δ	change, difference
ε	dielectric permittivity
η	viscosity
θ	fractional particle coverage
ϑ	step function
κ	inverse of the Debye screening length
Λ	inverse, effective threshold potential
μ	mobility
υ	general exponent
ψ	electrical potential
ω	Laplace transform of the time variable t

Miscellaneous symbols, indices and superscripts

$\mathscr{L}$	Laplace transform
∇	gradient
$\{\}_0$	initial
$\{\}_\infty$, $\{\}^\infty$	bulk
$\{\}_{\mathrm{Ci}}$	citrate
$\{\}_i$	chemical species i, general index
$\{\}_p$, $\{\}^p$	particle
$\{\}_s$, $\{\}^s$	surface
$\{\}_{\text{“something”}}$, $\{\}^{\text{“something”}}$	something[1]
$\tilde{\{\}}$	Laplace transform
$\underline{\{\}}$	per area

Universal constants

Symbol	Name	Value [32]
e	elementary charge	$1.60217646 \cdot 10^{-19}\,\mathrm{C}$
F_0	Faraday constant	eN_A
k_B	Boltzmann constant	$1.380650 \cdot 10^{-23}\,\mathrm{J/K}$
N_A	Avogadro constant	$6.0221420 \cdot 10^{23}\,\mathrm{molecules/mol}$
ε_0	vacuum permittivity	$8.854187817 \cdot 10^{-12}\,\mathrm{As/Vm}$